

Modeling nonlinear propagation
of ultrasound through
inhomogeneous biomedical media

Cover: *Karin Kellner*

www.karinkellner.com

Modeling nonlinear propagation of ultrasound through inhomogeneous biomedical media

PROEFSCHRIFT

ter verkrijging van de graad van doctor
aan de Technische Universiteit Delft,
op gezag van de Rector Magnificus prof. ir. K.C.A.M. Luyben,
voorzitter van het College voor Promoties,
in het openbaar te verdedigen
op 5 maart 2013 om 12:30 uur
door

Libertario DEMI

dottore magistrale in ingegneria delle telecomunicazioni
geboren te Cecina, Italië.

Dit proefschrift is goedgekeurd door de promotor:

Prof. dr. ir. A. Gisolf

Copromotoren:

Dr. K.W.A. van Dongen

Dr. ir M.D. Verweij

Samenstelling promotiecommissie:

Rector Magnificus,	voorzitter
Prof. dr. ir. A. Gisolf	Technische Universiteit Delft, promotor
Dr. K.W.A. van Dongen	Technische Universiteit Delft, copromotor
Dr. ir. M.D. Verweij	Technische Universiteit Delft, copromotor
Prof. dr. ir. A.W. Heemink	Technische Universiteit Delft
Prof. dr. ir. A.W.F. van der Steen	Erasmus Medical Center Rotterdam
Prof. dr. ing. G. Schmitz	Ruhr-Universität Bochum, Germany
Prof. O. Basset	INSA-Lyon, France
Prof. dr. ir. P.M. van den Berg	Technische Universiteit Delft, reservelid

ISBN 978-94-6191-626-6

Copyright ©2013, by L. Demi, Laboratory of Acoustical Wavefield Imaging, Faculty of Applied Sciences, Delft University of Technology, Delft, The Netherlands.

All rights reserved. No part of this publication may be reproduced, stored in a retrieval system or transmitted in any form or by any means, electronic, mechanical, photocopying, recording or otherwise, without the prior written permission of the author.

Typesetting system: L^AT_EX.

Printed in The Netherlands by Ipskamp Drukkers, Enschede.

*All that is straight (linear) lies, all truth is crooked (nonlinear)*¹

¹ Inspired by “Alles Gerade lügt, ... alle Wahrheit ist krumm”. [Friedrich Nietzsche, Also sprach Zarathustra]

Contents

1	Introduction	1
1.1	Ultrasound in medicine	1
1.2	Nonlinear acoustics	3
1.3	This thesis	5
2	Theory	9
2.1	Nonlinear wave equation with spatially varying κ and β	9
2.2	Inclusion of spatially varying attenuation	14
2.3	Compliance relaxation function	16
2.3.1	General properties	17
2.3.2	Compliance relaxation function for frequency power law losses	18
2.4	Contrast source approach	20
3	Neumann scheme	23
3.1	Solution method	23
3.1.1	Neumann scheme	23
3.1.2	Convergence	24
3.2	Results	25
3.2.1	Configuration 1	26
3.2.2	Configuration 2	29
3.3	Conclusions	39
4	Bi-CGSTAB scheme	41
4.1	Linearization	41
4.2	Solution method	43

4.2.1	Bi-CGSTAB scheme	43
4.2.2	Convergence	45
4.3	Results	45
4.3.1	Configuration 3	45
4.3.2	Configuration 4	50
4.4	Conclusions	61
5	Steepest Descent scheme	65
5.1	Solution method	66
5.1.1	Steepest Descent scheme	67
5.1.2	Convergence	68
5.2	Results	68
5.2.1	Configuration 3	69
5.2.2	Configuration 5	71
5.3	Conclusions	80
6	Application of the method developed	83
6.1	Parallel transmit beamforming using OFDM for harmonic imaging	83
6.1.1	Introduction	83
6.2	Theory	84
6.2.1	Operating principles	85
6.2.2	Maximum exploitable bandwidth condition	86
6.2.3	Mixing frequencies	88
6.3	Results	88
6.3.1	Numerical study	89
6.3.2	Measurements	98
6.4	Conclusions	101
7	Conclusions and Discussion	103
7.1	Conclusions	103
7.2	Discussion	105
A	Appendix: Lossy Green's function combined with contrast source approach	107
A.1	Results	108
A.1.1	Convergence	108
A.1.2	In silico experiments	109
A.2	Conclusions	110

B Appendix: List of configurations	113
Bibliography	115
Summary	123
Samenvatting	127
About the author	131
Publications	133

Introduction

This thesis is concerned with the development of a numerical method for modeling the nonlinear propagation of pressure wave fields through inhomogeneous biomedical media. This method may be used to design and optimize ultrasound transducers or to investigate novel ultrasound modalities or devices. Nonlinear propagation, attenuation and spatial inhomogeneities in the relevant acoustical parameters, i.e. coefficient of nonlinearity, attenuation and speed of sound, are included in the model, leading to the formulation of an integral equation. The method developed provides a solution to this equation by means of advanced iterative schemes and is an extension of the already existing iterative nonlinear contrast source (INCS) method [1, 2]. In this thesis, several iterative schemes have been derived, implemented and compared. In addition, the obtained numerical method has been used to assist in the design of a probe for echographic imaging (within a joint project with Erasmus Medical Center and Oldest Ultrasound) and to evaluate the performances of novel imaging modalities [3, 4].

In this Chapter the application of ultrasound in medicine and the basics of nonlinear acoustics are discussed in Section 1.1 and 1.2 respectively. Next, an overview of the work presented in this thesis is given in Section 1.3.

1.1 Ultrasound in medicine

The application of ultrasound in the field of medicine was first suggested for therapy, as early as 1932 [5], following the studies on the biological effect of ul-

trasound. These studies began thanks to Langévin's 1917 observation [6], whom during sonar experiments noted destruction of school of fishes in the sea, and thanks to the work done from Wood and Loomis [5]. Although the possibility to use sound for imaging was known since the World War I due to sonar applications, diagnostic application of ultrasound appeared only from the end of the 30's. Firestone's 1942 patent [5] is considered, even if originally thought for flaw detection in metal, the first modern pulse-echo ultrasound technique and the basis for pulse-echo in imaging. Successively, in the late 40's and early 50's, Howry and Wild [5] showed respectively the possibility to detect tissue interfaces and differentiate tissue structures (cancer from benign) by means of ultrasound. Around 20 years later, a big step toward the pulse-echo imaging systems utilized nowadays was made, thanks to Somer and Bom, whom introduced the phased-array and linear-array transducers respectively in 1968 [7] and 1971 [8]. To mention another interesting example, it was in the 80's when Howry and his group demonstrated that ultrasound could be used to produce a tomographic image of soft human tissues. To do so they transformed parts of a World War II B-29 bomber gun turret into a water tank in which the patient was immersed. Next, an ultrasound transducer was revolved around the patient using the turret ring gear, and images of a cross section of the neck were obtained [6]. The rapid growth of ultrasound based examinations and treatments has boosted the research on medical ultrasound during the last 30 years. Nowadays ultrasound is standard practice for the diagnosis as well as for the treatment of a wide range of diseases. To give an idea, in the year 2000, it has been estimated that each week five million ultrasound examinations were performed world-wide [6].

Echocardiography is one application from many where ultrasound is used for diagnosis. With echocardiography, images of the heart are obtained from a transthoracic echocardiogram (TTE) or trans-esophageal echocardiogram (TEE). During a TTE an ultrasound transducer is positioned at different locations on the chest or abdominal wall. Next, the transducer transmits pressure waves at ultrasonic frequencies into the chest and records echoes reflecting off the different parts of the insonified volume. After processing the acquired signals, high quality images of the heart are obtained. An echocardiogram may be used to evaluate the condition of the four chambers of the heart, the heart valves, the lining of the heart (the pericardium), and the aorta. In addition, it can be useful for detecting a heart attack, enlargement or hypertrophy of the heart, cardiac tumors, and a variety of other findings. A disadvantage of TTE is that the accuracy

and image quality may be reduced because of obesity, chronic obstructive pulmonary disease, chest-wall deformities, otherwise technically difficult patients, and in general by the presence of obstacles such as ribs and lungs. In circumstances in which satisfying images cannot be obtained via TTE, TEE may be utilized. With TEE the probe is positioned inside the esophagus, just behind the heart. Therefore, the transducer is closer to the heart as compared to TTE and basically no obstacles are present in the field of view. Drawbacks of TEE are the necessity of a fasting and sedated patient, increase in examination time and the risk for possible injuries, e.g. esophageal perforation [9].

It's the author's believe that a better understanding of the physical phenomena behind pressure wave propagation will improve the equipment by which patients will be examined and treated in the future. This is the driving motive behind the research presented in this thesis.

1.2 Nonlinear acoustics

The propagation of a pressure wave field is a nonlinear phenomenon. The nonlinearity may be represented by pressure dependent acoustic medium parameters, i.e. volume density of mass and compressibility. However, for small amplitude pressure wave fields that propagate over a short distance, this nonlinear phenomenon is not significant, and a linear approximation provides sufficiently good results. Nevertheless, for biomedical applications, when transient pressure fields with amplitudes in the order of 100 kPa or higher are used, the cumulative nonlinear distortion starts to play a significant role and manifests itself by the appearance of harmonic components, i.e. emerging spectral content centered around multiples of the central frequency of the emitted wave. Figure 1.1 shows and compares the time signal and frequency spectra of a plane wave propagating through a lossless homogeneous medium (water) in case of a peak pressure equal to 1 kPa (solid line) or 2.5 MPa (dashed line). In the first case the normalized time signal and frequency spectra remain identical during propagation, while this is not the case when the source signal with the same shape but a much higher amplitude is transmitted and nonlinear propagation is considered. With nonlinear propagation, the part of the wave at higher pressure levels tends to move faster than the part at lower pressure levels, resulting in a distortion of the wave shape. In the frequency domain, this distortion becomes apparent through the formation of harmonic components. The fundamental component (F0), together with the

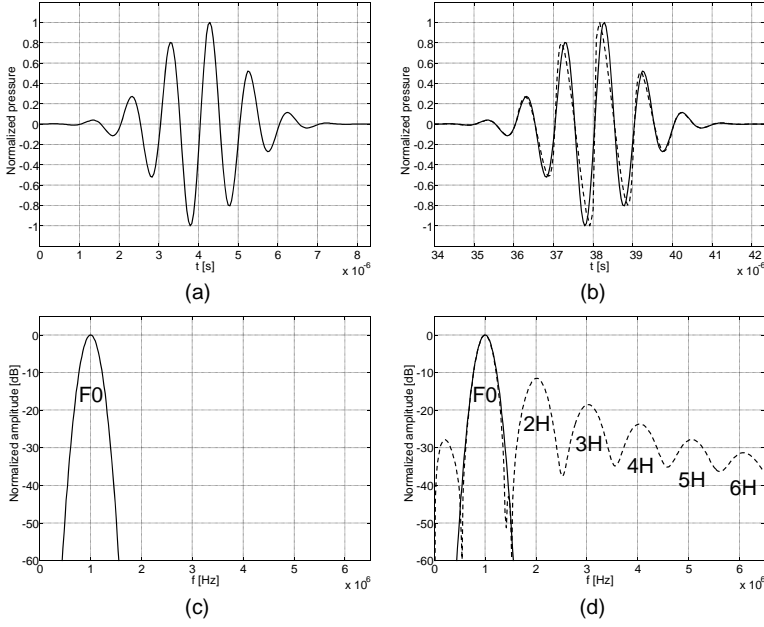


Figure 1.1: Normalized time signal and frequency spectra for a plane wave (a,c) at source position and (b,d) after propagating 50 mm through water, in case of a peak pressure equal to 1 kPa (solid line) and 2.5 MPa (dashed line).

second (2H) up to sixth (6H) harmonic component, is visible in Fig. 1.1(d).

Nowadays, nonlinear acoustics play a key role in the development of new medical diagnostic and therapeutic applications of ultrasound. For example, nonlinear ultrasound is known to improve significantly the quality of echographic images [10] and to influence the heat deposition during acoustic ablation therapy [11]. These effects are due to the higher harmonic wave fields generated during propagation. These harmonic fields contain higher frequencies than the pressure wave field at the surface of the transducer, and yield, therefore, an improved axial resolution and increased absorption because of the frequency dependency of the absorption mechanism. Furthermore, among the peculiarities of the beam formed by the higher harmonic wave fields, are a reduction of the elevation and lateral size of the focal spot and the reduction of clutter, and side and grating lobes [10], as compared to the fundamental wave field. An

example of a well known ultrasound imaging modality is Tissue Harmonic Imaging (THI) [12, 13, 14, 15]. This technique, which takes advantage of the benefits mentioned by imaging only the reflected second harmonic component, is currently the standard in commercial diagnostic ultrasound scanning systems. To exploit further the benefits of higher harmonics, researchers currently investigate ultrasound imaging based on the reflection of the third to the fifth harmonic component. In literature this is referred to as Super-Harmonic Imaging (SHI) [3, 16, 17]. The ability to simulate accurately and understand the corresponding nonlinear phenomena is therefore necessary for the development, design and optimization of new ultrasound modalities or devices.

1.3 This thesis

The research presented in this thesis concerns the development of a numerical method for modeling nonlinear pressure wave field propagation through inhomogeneous biomedical media. Existing methods for the numerical simulation of nonlinear acoustic wave fields may be divided into two categories: forward wave methods and full wave methods [18, 19].

Forward wave methods start with a pressure distribution in the plane of the transducer, and march the field forward in a preferred direction, which usually corresponds to the direction of the main beam [20, 21, 22, 23, 24, 25, 26]. Many methods that belong to this category, such as the Khokhlov-Zabolotskaya-Kuznetsov (KZK) method [21, 26], subject the acoustic wave equation to a parabolic approximation. Consequently, forward wave methods are inaccurate for fields that propagate in directions which deviate from the preferred direction of propagation, and cannot deal with back-scattered wave fields.

Full wave methods do not involve a preferred direction of propagation. Some methods that belong to this category solve the relevant basic acoustic equations using Finite Difference [27, 28, 29] or Finite Element [30] methods. Since these methods need to sample at considerably more than two points per smallest wavelength and per shortest period, the number of grid points needed to handle a realistic computational domain soon becomes too large. The INCS [1, 2] method is a full wave method which avoids this problem. By taking advantage of the Filtered Convolution method [31] it only requires two points per wavelength or period and therefore it can handle nonlinear ultrasound fields over computational

domains measuring hundreds of wavelengths and periods. Originally, the INCS method was only applied to homogeneous nonlinear media with frequency power law attenuation [1, 32].

In this thesis the basic steps behind INCS, i.e. the contrast source approach and the Filtered Convolution method [31], are preserved and the method is extended to deal with spatially varying attenuation, coefficient of nonlinearity and speed of sound.

In Chapter 2, the theory is presented and discussed. Here, the integral equation which defines our contrast source problem is derived starting from the equation of motion and the deformation equation.

Chapter 3 contains results obtained with the application of a Neumann scheme. In case of strong contrasts typically observed in biomedical applications, Neumann may result in slow convergence or may even diverge. In order to overcome this problem other schemes have been investigated.

Chapter 4 contains the formulation of an alternative approach, where the nonlinear problem is linearized and solved using a biconjugate gradient stabilized (Bi-CGSTAB) scheme. This scheme is faster and more robust when compared to Neumann. As a drawback, the linearization of the contrast source leads to a significant systematic error for the harmonics of the fourth order or higher. If an accurate simulation of the higher harmonics is needed, a different approach is necessary.

In Chapter 5 a Steepest Descent based method is formulated and results for nonlinear pressure wave field propagating through lossy inhomogeneous media are presented and discussed. This method allows for modeling of the full nonlinear problem, including inhomogeneities in the speed of sound, attenuation and coefficient of nonlinearity. As a drawback it results in a higher computational load and a reduction of the convergence speed.

Chapter 6 contains an example of a possible application of the method developed. A feasibility study that aims to compare the performances of standard parallel beamforming with a new parallel beamforming technique, i.e. parallel transmit beamforming using orthogonal frequency division multiplexing (OFDM), is

discussed.

A discussion of the overall content of the thesis as well as suggestions for further development together with final conclusions are contained in Chapter 7.

Chapter 2

Theory

In this Chapter, the nonlinear wave equation for a lossless medium with a spatially varying compressibility and coefficient of nonlinearity is derived. Next, the equation is extended to deal with spatially varying attenuation. The resulting equation is cast into an integral equation, which forms the starting point of our solution method.

2.1 Nonlinear wave equation with spatially varying κ and β

The acoustic wave motion is a dynamical state of matter that is superimposed on an existing static equilibrium state [34]. To describe the total state, we make use of the equation of motion

$$\nabla \underline{p}(\mathbf{x}, t) + \underline{\rho}(\mathbf{x}, t) D_t \underline{\mathbf{v}}(\mathbf{x}, t) = \underline{\mathbf{f}}(\mathbf{x}, t), \quad (2.1)$$

and the deformation equation

$$\nabla \cdot \underline{\mathbf{v}}(\mathbf{x}, t) + \underline{\kappa}(\mathbf{x}, t) D_t \underline{p}(\mathbf{x}, t) = \underline{q}(\mathbf{x}, t). \quad (2.2)$$

Here, the vector \mathbf{x} contains the coordinates of a position in a three-dimensional Cartesian domain \mathcal{D} , and t is the time coordinate. The symbol ∇ indicates the nabla operator, and $D_t = \partial_t + \mathbf{v} \cdot \nabla$ indicates the material time derivative. The properties of an acoustic medium are described via the volume density of mass $\underline{\rho}(\mathbf{x}, t)$ and the compressibility $\underline{\kappa}(\mathbf{x}, t)$. The underlinings are used to represent

total quantities and to distinguish them from their static or excess values. Equations (2.1) and (2.2) describe the relation between the pressure wave field $\underline{p}(\mathbf{x}, t)$, the particle velocity wave field $\underline{\mathbf{v}}(\mathbf{x}, t)$, the volume source density of volume force $\underline{\mathbf{f}}(\mathbf{x}, t)$, and the volume source density of injection rate $\underline{q}(\mathbf{x}, t)$. Equation (2.1) follows from combining the conservation laws of linear momentum (Newton's second law) and mass, and (2.2) is obtained by combining the conservation laws of volume and mass [1]. Throughout this thesis, we employ the Eulerian description of continuum mechanics.

To extract the dynamical state, we write

$$p(\mathbf{x}, t) = \underline{p}(\mathbf{x}, t) - p_0, \quad (2.3)$$

$$\mathbf{v}(\mathbf{x}, t) = \underline{\mathbf{v}}(\mathbf{x}, t) - \mathbf{v}_0, \quad (2.4)$$

$$\mathbf{f}(\mathbf{x}, t) = \underline{\mathbf{f}}(\mathbf{x}, t) - \mathbf{f}_0, \quad (2.5)$$

$$q(\mathbf{x}, t) = \underline{q}(\mathbf{x}, t) - q_0. \quad (2.6)$$

Here, the quantities on the left hand side denote the dynamic perturbations of the static equilibrium state, which is represented by the quantities with subscript '0'. The quantity $p(\mathbf{x}, t)$ is called the excess or acoustic pressure. Furthermore, p_0 is the static pressure, $\mathbf{v}_0 = 0$ m/s, \mathbf{f}_0 is the force of gravity, and $q_0 = 0$ s⁻¹.

Comparison with work that includes the state equation of the medium, reveals that the counterparts of Eqs (2.1) and (2.2) for the perturbations are [35, 36]

$$\nabla p(\mathbf{x}, t) + \underline{\rho}(\mathbf{x}, t) D_t \mathbf{v}(\mathbf{x}, t) = \underline{\mathbf{f}}(\mathbf{x}, t), \quad (2.7)$$

$$\nabla \cdot \mathbf{v}(\mathbf{x}, t) + \underline{\kappa}(\mathbf{x}, t) D_t p(\mathbf{x}, t) = \underline{q}(\mathbf{x}, t). \quad (2.8)$$

with

$$\underline{\rho}(\mathbf{x}, t) = \rho(\mathbf{x}) [1 + \kappa(\mathbf{x}) p(\mathbf{x}, t)], \quad (2.9)$$

$$\underline{\kappa}(\mathbf{x}, t) = \kappa(\mathbf{x}) \{1 + \kappa(\mathbf{x}) [1 - 2\beta(\mathbf{x})] p(\mathbf{x}, t)\}. \quad (2.10)$$

Here, $\kappa(\mathbf{x})$ and $\rho(\mathbf{x})$ represent the static compressibility and volume density of mass respectively, and $\beta(\mathbf{x})$ is called the coefficient of nonlinearity. The coefficient of nonlinearity β characterizes the nonlinear distortion that occurs during propagation [37]. Each point on the waveform propagates in fact at a different speed, which is determined by its value of excess pressure and by the medium properties, and in particular by the coefficient of nonlinearity β . For an arbitrary fluid, the coefficient of nonlinearity may be written as a summation of two terms,

i.e., $\beta = 1 + B/2A$. Here, the term B/A is the ratio of the second and first order coefficient in a Taylor series expansion of the isentropic equation of state, and is due to the nonlinearity of the pressure-density relation. The first term instead, does not depend on the nonlinearity of the pressure-density relation, and is due to convection [37]. Combined with Eqs. (2.9) and (2.10), Eqs. (2.7) and (2.8) are accurate up till second order in the perturbation quantities. These equations can be utilized to model the nonlinear propagation of a pressure wave field through media presenting spatially varying speed of sound and coefficient of nonlinearity. Here, we opted to model inhomogeneities in the speed of sound via inhomogeneities in the static compressibility. Therefore, the volume density of mass is assumed to be invariant with respect to spatial coordinates and equal to the volume density of mass of the background medium, i.e. $\rho(\mathbf{x}) = \rho_{bg}$.

Equations (2.7) and (2.8) can be combined with Eqs. (2.9) and (2.10). After discarding wave field terms of third order and higher, we obtain

$$\begin{aligned} \nabla p(\mathbf{x}, t) + \rho_{bg} \partial_t \mathbf{v}(\mathbf{x}, t) = & \mathbf{f}(\mathbf{x}, t) - \frac{1}{2} \rho_{bg} \nabla [\mathbf{v}(\mathbf{x}, t) \cdot \mathbf{v}(\mathbf{x}, t)] \\ & - \rho_{bg} \kappa(\mathbf{x}) p(\mathbf{x}, t) \partial_t \mathbf{v}(\mathbf{x}, t), \end{aligned} \quad (2.11)$$

$$\begin{aligned} \nabla \cdot \mathbf{v}(\mathbf{x}, t) + \kappa(\mathbf{x}) \partial_t p(\mathbf{x}, t) = & q(\mathbf{x}, t) - \kappa(\mathbf{x}) \mathbf{v}(\mathbf{x}, t) \cdot \nabla p(\mathbf{x}, t) \\ & - \kappa^2(\mathbf{x}) [1 - 2\beta(\mathbf{x})] p(\mathbf{x}, t) \partial_t p(\mathbf{x}, t). \end{aligned} \quad (2.12)$$

Next, the combination of Eq. (2.11) with Eq. (2.12) provides the nonlinear wave equation with inhomogeneities in the compressibility and in the coefficient of nonlinearity,

$$\begin{aligned} \nabla^2 p(\mathbf{x}, t) - \frac{1}{c^2(\mathbf{x})} \partial_t^2 p(\mathbf{x}, t) = & -\rho_{bg} \partial_t q(\mathbf{x}, t) + \nabla \cdot \mathbf{f}(\mathbf{x}, t) \\ & - \nabla \cdot \left\{ \frac{1}{2} \rho_{bg} \nabla [\mathbf{v}(\mathbf{x}, t) \cdot \mathbf{v}(\mathbf{x}, t)] \right\} \\ & + \rho_{bg} \partial_t \left\{ \kappa^2(\mathbf{x}) [1 - 2\beta(\mathbf{x})] p(\mathbf{x}, t) \partial_t p(\mathbf{x}, t) \right\} \\ & - \nabla \cdot [\rho_{bg} \kappa(\mathbf{x}) p(\mathbf{x}, t) \partial_t \mathbf{v}(\mathbf{x}, t)] \\ & + \rho_{bg} \partial_t [\kappa(\mathbf{x}) \mathbf{v}(\mathbf{x}, t) \cdot \nabla p(\mathbf{x}, t)], \end{aligned} \quad (2.13)$$

where the small-signal speed of sound equals

$$c(\mathbf{x}) = \frac{1}{\sqrt{\rho_{bg} \kappa(\mathbf{x})}}. \quad (2.14)$$

Outside any source domain we can use Eq. (2.7) to reformulate Eq. (2.13) into

$$\begin{aligned} \nabla^2 p(\mathbf{x}, t) - \frac{1}{c^2(\mathbf{x})} \partial_t^2 p(\mathbf{x}, t) = & -\rho_{bg} \partial_t q(\mathbf{x}, t) + \nabla \cdot \mathbf{f}(\mathbf{x}, t) \\ & - \rho_{bg} \kappa^2(\mathbf{x}) \beta(\mathbf{x}) \partial_t^2 p^2(\mathbf{x}, t) \\ & + \frac{1}{2} [\nabla \kappa(\mathbf{x})] \cdot \nabla p^2(\mathbf{x}, t) \\ & + \left\{ \frac{1}{2} \kappa(\mathbf{x}) \nabla^2 p^2(\mathbf{x}, t) - \frac{1}{2} \rho_{bg} \nabla^2 [\mathbf{v}(\mathbf{x}, t) \cdot \mathbf{v}(\mathbf{x}, t)] \right. \\ & \left. - \frac{1}{2} \rho_{bg}^2 \kappa(\mathbf{x}) \partial_t^2 [\mathbf{v}(\mathbf{x}, t) \cdot \mathbf{v}(\mathbf{x}, t)] + \frac{1}{2} \rho_{bg} \kappa^2(\mathbf{x}) \partial_t^2 p^2(\mathbf{x}, t) \right\}, \quad (2.15) \end{aligned}$$

where we neglected the terms of third order in the wave field quantities.

Now we consider the term in between the curly brackets of Eq. (2.15). From Eq. (2.7), it can be proved that for a homogeneous volume density of mass, outside any source domain and up to first order in the wave field quantities, the acoustic velocity $\mathbf{v}(\mathbf{x}, t)$ is irrotational, i.e. $\nabla \times \mathbf{v}(\mathbf{x}, t) = 0$. The acoustic velocity can therefore be expressed by means of a velocity potential $\phi(\mathbf{x}, t)$, viz.

$$\mathbf{v}(\mathbf{x}, t) = \nabla \phi(\mathbf{x}, t), \quad (2.16)$$

and consequently the pressure field $p(\mathbf{x}, t)$ can be expressed as

$$p(\mathbf{x}, t) = -\rho_{bg} \partial_t \phi(\mathbf{x}, t). \quad (2.17)$$

Substitution of Eqs. (2.16) and (2.17) into the term in between curly brackets in Eq. (2.15) allows the latter to be rewritten as

$$\begin{aligned} -\frac{1}{2} \rho_{bg} [\nabla^2 + \rho_{bg} \kappa(\mathbf{x}) \partial_t^2] \left\{ \frac{1}{2} [\nabla^2 \phi^2(\mathbf{x}, t) - \rho_{bg} \kappa(\mathbf{x}) \partial_t^2 \phi^2(\mathbf{x}, t)] \right. \\ \left. - \phi(\mathbf{x}, t) [\nabla^2 \phi(\mathbf{x}, t) - \rho_{bg} \kappa(\mathbf{x}) \partial_t^2 \phi(\mathbf{x}, t)] \right\} \\ - \nabla [\rho_{bg}^2 \kappa(\mathbf{x})] \cdot \nabla [\partial_t \phi(\mathbf{x}, t)]^2 \\ - \frac{1}{2} \nabla^2 [\rho_{bg}^2 \kappa(\mathbf{x})] [\partial_t \phi(\mathbf{x}, t)]^2. \quad (2.18) \end{aligned}$$

Next, assuming the quantities in the second order terms in the wave equation to obey to a plane wave relation, the *kinetic energy* density equals the *potential energy* density (which assumes the Lagrangian density to be zero):

$$\kappa(\mathbf{x}) p^2(\mathbf{x}, t) = \rho_{bg} \mathbf{v}(\mathbf{x}, t) \cdot \mathbf{v}(\mathbf{x}, t). \quad (2.19)$$

It can be demonstrated, in combination with Eq (2.16) and (2.17), that

$$\nabla^2 \phi^2(\mathbf{x}, t) - \rho_{bg} \kappa(\mathbf{x}) \partial_t^2 \phi^2(\mathbf{x}, t) = 0. \quad (2.20)$$

Equation (2.20) can also be obtained from the arguments put forward by Aanonsen et al. [38] and Naze and Tjøtta [39, 40], as the term on the left hand side of equation (2.20) is negligible under the assumption that the cumulative nonlinear effect dominates the local nonlinear effect. Combining Eqs. (2.16), (2.17) and Eq. (2.8), we obtain a wave equation in $\phi(\mathbf{x}, t)$, which is valid up to first order:

$$\nabla^2 \phi(\mathbf{x}, t) - \rho_{bg} \kappa(\mathbf{x}) \partial_t^2 \phi(\mathbf{x}, t) = 0. \quad (2.21)$$

The combination of Eqs. (2.16), (2.17), (2.20) and Eq. (2.21), allows us to rewrite the term in Eq. (2.18) as follows

$$\begin{aligned} -\nabla [\rho_{bg}^2 \kappa(\mathbf{x})] \cdot \nabla [\partial_t \phi(\mathbf{x}, t)]^2 - \frac{1}{2} \nabla^2 [\rho_{bg}^2 \kappa(\mathbf{x})] [\partial_t \phi(\mathbf{x}, t)]^2 \\ = -\nabla \kappa(\mathbf{x}) \cdot \nabla p^2(\mathbf{x}, t) - \frac{1}{2} \nabla^2 [\kappa(\mathbf{x})] p^2(\mathbf{x}, t). \end{aligned} \quad (2.22)$$

From Eq. (2.22), we can reformulate Eq. (2.15) in the form

$$\begin{aligned} \nabla^2 p(\mathbf{x}, t) - \frac{1}{c^2(\mathbf{x})} \partial_t^2 p(\mathbf{x}, t) = -\rho_{bg} \partial_t q(\mathbf{x}, t) + \nabla \cdot \mathbf{f}(\mathbf{x}, t) \\ - \rho_{bg} \kappa^2(\mathbf{x}) \beta(\mathbf{x}) \partial_t^2 p^2(\mathbf{x}, t) \\ - \frac{1}{2} [\nabla \kappa(\mathbf{x})] \cdot \nabla p^2(\mathbf{x}, t) \\ - \frac{1}{2} [\nabla^2 \kappa(\mathbf{x})] p^2(\mathbf{x}, t). \end{aligned} \quad (2.23)$$

In conclusion, Eq. (2.23) can be rewritten as follows

$$\begin{aligned} \nabla^2 p(\mathbf{x}, t) - \frac{1}{c_{bg}^2} \partial_t^2 p(\mathbf{x}, t) = -S_{pr}(\mathbf{x}, t) \\ - S_{nl} [p(\mathbf{x}, t)] - S_{nl\kappa} [p(\mathbf{x}, t)] - S_c [p(\mathbf{x}, t)], \end{aligned} \quad (2.24)$$

with

$$c_{bg}^2 = \frac{1}{\rho_{bg} \kappa_{bg}}, \quad (2.25)$$

$$S_{pr}(\mathbf{x}, t) = \rho_{bg} \partial_t q(\mathbf{x}, t) - \nabla \cdot \mathbf{f}(\mathbf{x}, t), \quad (2.26)$$

$$S_{nl} [p(\mathbf{x}, t)] = \rho_{bg} \kappa^2(\mathbf{x}) \beta(\mathbf{x}) \partial_t^2 p^2(\mathbf{x}, t), \quad (2.27)$$

$$S_{nl\kappa} [p(\mathbf{x}, t)] = \frac{1}{2} \nabla \cdot \{ [\nabla \kappa(\mathbf{x})] p^2(\mathbf{x}, t) \}, \quad (2.28)$$

$$S_c [p(\mathbf{x}, t)] = \left[\frac{1}{c_{bg}^2} - \frac{1}{c^2(\mathbf{x})} \right] \partial_t^2 p(\mathbf{x}, t). \quad (2.29)$$

Here, c_{bg} and κ_{bg} are spatially independent quantities representing the small-signal speed of sound and the static compressibility of the background medium. $S_{pr}(\mathbf{x}, t)$ represents the primary source, which is the source that generates the pressure field, $S_{nl}[p(\mathbf{x}, t)]$ is the nonlinear contrast source, which models the nonlinear correction to the linear field and $S_c[p(\mathbf{x}, t)]$ and $S_{nl\kappa}[p(\mathbf{x}, t)]$ represent the speed of sound and second order compressibility contrast source respectively. For homogeneous media, $S_{nl\kappa}[p(\mathbf{x}, t)]$ and $S_c[p(\mathbf{x}, t)]$ are zero and Eq. (2.24) becomes the lossless Westervelt equation [1, 39].

2.2 Inclusion of spatially varying attenuation

In most medical applications of ultrasound, the medium cannot be considered to be lossless and spatially varying attenuation must be accounted for.

Here, to incorporate losses, a causal relaxation function is employed, as it provides a compact way of modeling the frequency power law attenuation typically observed in biomedical tissue. In addition, it automatically yields the associated dispersion and it allows for a straightforward extension to spatially varying losses. In this section we first derive the linear lossy wave equation, followed by a modification of the lossless nonlinear wave equation in Eq. (2.23) to cope with spatially varying losses.

Using the relaxation function approach, the lossless deformation equation, in its low velocity approximation:

$$\nabla \cdot \mathbf{v}(\mathbf{x}, t) + \kappa_{bg} \partial_t p(\mathbf{x}, t) = q(\mathbf{x}, t), \quad (2.30)$$

may be turned into its lossy counterpart [35, 41, 42]

$$\nabla \cdot \mathbf{v}(\mathbf{x}, t) + \kappa_{bg} \partial_t [m(\mathbf{x}, t) * p(\mathbf{x}, t)] = q(\mathbf{x}, t). \quad (2.31)$$

Here, $m(\mathbf{x}, t)$ is the normalized compliance (or memory) relaxation function. This function depends on \mathbf{x} to model spatially dependent attenuation and may be separated into

$$m(\mathbf{x}, t) = \delta(t) + A(\mathbf{x}, t), \quad (2.32)$$

where the Dirac delta function $\delta(t)$ represents the instantaneous medium behavior, and the function $A(\mathbf{x}, t)$ represents the delayed reaction of the medium on events that occurred in the past. This behavior is associated with the occurrence

of losses. Because of its physical role, the relaxation function $m(\mathbf{x}, t)$ is real valued and causal.

In the same way, the equation of motion (in its low velocity approximation),

$$\nabla p(\mathbf{x}, t) + \rho_{bg} \partial_t \mathbf{v}(\mathbf{x}, t) = \mathbf{f}(\mathbf{x}, t), \quad (2.33)$$

may be turned into its lossy version by convolving $\mathbf{v}(\mathbf{x}, t)$ with a normalized inertia relaxation function $\mu(\mathbf{x}, t)$ [41, 42]. However, it is usually assumed that in biological tissue attenuation is mainly due to relaxation in the compliance, while the inertia shows negligible relaxation effects [1, 35].

Combination of Eqs. (2.31) and (2.33) yields the following wave equation for linear acoustic media with spatially varying losses

$$\nabla^2 p(\mathbf{x}, t) - \frac{1}{c_{bg}^2} \partial_t^2 [m(\mathbf{x}, t) *_t p(\mathbf{x}, t)] = -S_{pr}(\mathbf{x}, t). \quad (2.34)$$

Substitution of Eq. (2.32) into Eq. (2.34) allows the latter to be rewritten as

$$\nabla^2 p(\mathbf{x}, t) - \frac{1}{c_{bg}^2} \partial_t^2 p(\mathbf{x}, t) = -S_{pr}(\mathbf{x}, t) + \frac{1}{c_{bg}^2} \partial_t^2 [A(\mathbf{x}, t) *_t p(\mathbf{x}, t)]. \quad (2.35)$$

Similar to the contrast sources in Eq. (2.24), an attenuation contrast source now appears at the right-hand side of Eq. (2.35), which equals

$$S_{at}[p(\mathbf{x}, t)] = -\frac{1}{c_{bg}^2} \partial_t^2 [A(\mathbf{x}, t) *_t p(\mathbf{x}, t)]. \quad (2.36)$$

So far, we consider the background medium to be lossless. In order to reduce the correction that the attenuative contrast source has to account for, (see Appendix A) we can write the compliance memory function as a summation of two terms:

$$m(\mathbf{x}, t) = m_{bg}(t) + \Delta m(\mathbf{x}, t), \quad (2.37)$$

where $m_{bg}(t)$ models the losses of the background medium and $\Delta m(\mathbf{x}, t) = m(\mathbf{x}, t) - m_{bg}(t)$ models the variations in the attenuation properties with respect to the homogeneous background medium. Combining Eq. (2.37) with Eq. (2.34) results in

$$\begin{aligned} \nabla^2 p(\mathbf{x}, t) - \frac{1}{c_{bg}^2} \partial_t^2 [m_{bg}(t) *_t p(\mathbf{x}, t)] &= -S_{pr}(\mathbf{x}, t) \\ &+ \frac{1}{c_{bg}^2} \partial_t^2 [\Delta m(\mathbf{x}, t) *_t p(\mathbf{x}, t)], \end{aligned} \quad (2.38)$$

with on the left hand side the linear lossy wave equation and on the right hand side the primary source $S_{\text{pr}}(\mathbf{x}, t)$ and the pressure dependent attenuation contrast source $S_{\text{at}}[p(\mathbf{x}, t)]$:

$$S_{\text{at}}[p(\mathbf{x}, t)] = -\frac{1}{c_{bg}^2} \partial_t^2 [\Delta m(\mathbf{x}, t) * p(\mathbf{x}, t)]. \quad (2.39)$$

The described approach can be utilized to include spatially varying losses in the lossless nonlinear wave equation in Eq. (2.23). Inclusion of the compliance memory function in the left hand side of Eq. (2.23) provides the wave equation for nonlinear media with spatially varying losses, coefficient of nonlinearity and speed of sound:

$$\begin{aligned} \nabla^2 p(\mathbf{x}, t) - \frac{1}{c_{bg}^2} \partial_t^2 [m_{bg}(t) * p(\mathbf{x}, t)] = & -S_{\text{pr}}(\mathbf{x}, t) \\ & - S_{\text{nl}}[p(\mathbf{x}, t)] - S_{\text{nl}\kappa}[p(\mathbf{x}, t)] - S_c[p(\mathbf{x}, t)] - S_{\text{at}}[p(\mathbf{x}, t)], \end{aligned} \quad (2.40)$$

with

$$S_c[p(\mathbf{x}, t)] = \left[\frac{1}{c_{bg}^2} - \frac{1}{c^2(\mathbf{x})} \right] \partial_t^2 [m_{bg}(t) * p(\mathbf{x}, t)], \quad (2.41)$$

$$S_{\text{at}}[p(\mathbf{x}, t)] = -\frac{1}{c(\mathbf{x})^2} \partial_t^2 [\Delta m(\mathbf{x}, t) * p(\mathbf{x}, t)]. \quad (2.42)$$

Here, the effect of the delayed reaction of the medium on second order terms in the wave quantities has been neglected [35]. In conclusion, Eqs. (2.40) – (2.42) may be written as

$$\nabla^2 p(\mathbf{x}, t) - \frac{1}{c_{bg}^2} \partial_t^2 [m_{bg}(t) * p(\mathbf{x}, t)] = -S_{\text{pr}}(\mathbf{x}, t) - S_{\text{cs}}[p(\mathbf{x}, t)], \quad (2.43)$$

where the total contrast source equals

$$S_{\text{cs}}[p(\mathbf{x}, t)] = S_{\text{nl}}[p(\mathbf{x}, t)] + S_{\text{nl}\kappa}[p(\mathbf{x}, t)] + S_c[p(\mathbf{x}, t)] + S_{\text{at}}[p(\mathbf{x}, t)]. \quad (2.44)$$

Equations (2.43) and (2.44) form an extended version of the Westervelt equation that allows to model nonlinear pressure wave field propagation through media with spatially varying attenuation, coefficient of nonlinearity and speed of sound.

2.3 Compliance relaxation function

In this Section, the general properties of a compliance relaxation function are derived. Moreover, a suitable relaxation function is proposed that yields a frequency power law attenuation as observed in most biological tissue, and that satisfies causality [1, 32, 33].

2.3.1 General properties

For convenience it is first assumed that the attenuation is spatially independent, i.e. the considered compliance memory function is $m(\mathbf{x}, t) = m(t)$. If in that case Eqs. (2.31) and (2.33) are subjected to a temporal Laplace transformation and the proper substitutions are performed, the following wave equation is obtained

$$\nabla^2 \hat{p}(\mathbf{x}, s) - \frac{s^2}{c_{bg}^2} \hat{m}(s) \hat{p}(\mathbf{x}, s) = -\hat{S}_{pr}(\mathbf{x}, s), \quad (2.45)$$

where the hat $\hat{\cdot}$ indicates that a quantity has been transformed by means of the Laplace transformation with transform parameter s . At this stage, the Laplace transformation is preferred over the Fourier transformation. This is because Lerch's theorem [43, 44, 45] for the Laplace transformation provides a stronger and simpler way of keeping track of causality than the Paley-Wiener [46] theorem does for the Fourier transformation. From Lerch's theorem it may be deduced that a sufficient condition for a transform domain function $\hat{f}(s)$ to correspond to a unique, causal time domain function $f(t)$ is that $\hat{f}(s)$ should remain bounded for all real $s \geq s_0 \geq 0$, where s_0 may be chosen arbitrary large (but not infinite). Like any of the transformed quantities, $\hat{m}(s)$ is the Laplace transform of a real function $m(t)$, so $\hat{m}(s)$ must be real for real values of s . Moreover, $\hat{m}(s)$ is the Laplace transform of a unique, causal function $m(t)$. As explained in the previous paragraph, this is certainly satisfied if $\hat{m}(s)$ remains bounded on the real axis for $s \geq s_0 \geq 0$. Upon solving Eq. (2.45), the obtained wave field will have a propagation coefficient

$$\hat{\gamma}(s) = \frac{s}{c_{bg}} \hat{m}^{\frac{1}{2}}(s), \quad (2.46)$$

in which c_{bg} is the wave speed in the lossless medium. In the lossless case there is no dispersion and every part of the wave has the same speed c_{bg} . This speed also applies to the wave front. The speed of the wave front always follows from the high-frequency behavior of $\hat{\gamma}$ as $c_{bg} = \lim_{|s| \rightarrow \infty} s / \hat{\gamma}(s)$ for $\text{Re}(s) > 0$. In case of losses, $\hat{A}(s)$ will be at most of order s^n with $n < 0$, because $A(t)$ is less singular at $t = 0$ than a delta function. Consequently, $\lim_{|s| \rightarrow \infty} \hat{m}(s) = 1$ and the wave front will travel with the same speed c_{bg} as in the lossless case. When replacing s by $j\omega$, the propagation coefficient may be written as

$$\hat{\gamma}(j\omega) = \hat{\alpha}(\omega) + j\hat{\beta}(\omega), \quad (2.47)$$

in which $\hat{\alpha}(\omega)$ is the attenuation coefficient and $\hat{\beta}(\omega)$ is the phase coefficient. In view of the causality of $m(t)$, the real and imaginary parts of $\hat{m}(j\omega)$ must now

satisfy the Kramers-Kronig relations [47]. As a consequence of causality, $\hat{\alpha}(\omega)$ cannot be chosen independently from $\hat{\beta}(\omega)$, and attenuation and dispersion will be interlinked phenomena.

The above theory is easily extended to the case of spatially varying losses by taking a spatially dependent compliance relaxation function $m(\mathbf{x}, t)$. From the above, it is possible to derive the general properties of any causal function $\hat{m}(\mathbf{x}, s)$ [1, 32, 33]:

1. $\hat{m}(\mathbf{x}, s)$ is real for real values of s ,
2. $\hat{m}(\mathbf{x}, s)$ remains bounded for all $s \geq s_0 \geq 0$,
3. $\lim_{|s| \rightarrow \infty} \hat{m}(\mathbf{x}, s) = 1$ for $\text{Re}(s) > 0$.

2.3.2 Compliance relaxation function for frequency power law losses

A function $\hat{m}(s)$ that for $s = j\omega$ provides the power law attenuation coefficient $\hat{\alpha}(\omega) = \alpha_1 |\omega|^b$ as observed in many measurements [48, 49, 50], is

$$\hat{m}(s) = \left[1 + \frac{c_{bg}\alpha_1 s^{b-1}}{\cos(\pi b/2)} \right]^2, \quad (2.48)$$

with positive real parameters α_1 and b (b may not be an odd integer). Some typical values are given in Table 2.1, and more extensive data may be found in the literature [6, 49, 50, 51]. The given function yields the same attenuation and phase coefficient as obtained by Szabo [52]. In the current context, two changes will be made to Eq. (2.48). First of all, in order to satisfy the last two requirements at the end of Subsection 2.3.1, a denominator is introduced that prevents the function to become infinite for $|s| \rightarrow \infty$ [1, 32, 33]. Secondly, the relevant loss coefficients are made spatially dependent. The resulting function $\hat{m}(\mathbf{x}, s)$ is

$$\hat{m}(\mathbf{x}, s) = \left\{ 1 + \frac{c_{bg}\alpha_1(\mathbf{x})s^{b(\mathbf{x})-1}}{\cos[\pi b(\mathbf{x})/2] [1 + (s/s_1)^d]} \right\}^2. \quad (2.49)$$

The parameters $\alpha_1(\mathbf{x})$ and $b(\mathbf{x})$ represent the spatially dependent attenuative properties of the specific medium. In addition, s_1 is a positive parameter that is larger than the largest angular frequency of interest, and d is a positive integer parameter that satisfies $d > \max_{\mathbf{x} \in \mathcal{D}} \{b(\mathbf{x})\} - 1$. The introduction of the factor $1 + (s/s_1)^d$ in the denominator ensures that the compliance relaxation function remains causal and that the wavefront remains traveling with the finite

wave speed c_{bg} instead of the infinite wave speed that is implied by Eq. (2.48). Since s_1 is larger than the largest frequency of interest, the influence of the term will be practically negligible while theoretically avoiding the occurrence of a noncausal compliance relaxation function and associated problems. After substitution of Eq. (2.49) into Eq. (2.46) and setting $s = j\omega$, it is easily shown that for $|\omega| < s_1$, the function $\hat{\gamma}(\mathbf{x}, j\omega)$ consists of spatially dependent attenuation coefficient $\hat{\alpha}(\mathbf{x}, j\omega)$ and a phase coefficient $\hat{\beta}(\mathbf{x}, j\omega)$ that can be approximated by

$$\hat{\alpha}(\mathbf{x}, \omega) \approx \alpha_1(\mathbf{x}) |\omega|^{b(\mathbf{x})}, \quad (2.50)$$

$$\hat{\beta}(\mathbf{x}, \omega) \approx \frac{\omega}{c_{bg}} + \alpha_1(\mathbf{x}) \tan[\pi b(\mathbf{x})/2] \omega |\omega|^{b(\mathbf{x})-1}. \quad (2.51)$$

In the spatially homogeneous case, these coefficients correspond to those described by Szabo [52], and the propagation of a one way plane wave with angular frequency ω is just governed by these coefficients. Equation (2.51) may be related to the phase speed $\hat{c}(\mathbf{x}, \omega)$ at angular frequency ω by using the relation $\hat{\beta}(\mathbf{x}, \omega) = \omega/\hat{c}(\mathbf{x}, \omega)$. This yields for $|\omega| < s_1$ the following dispersion equation

$$\hat{c}(\mathbf{x}, \omega) \approx \frac{1}{c_{bg}^{-1} + \alpha_1(\mathbf{x}) \tan[\pi b(\mathbf{x})/2] |\omega|^{b(\mathbf{x})-1}}. \quad (2.52)$$

Spatially varying attenuation is thus accompanied by a spatially varying phase speed. Both types of inhomogeneities will influence the propagation and give rise to scattering of an acoustic wave. By modeling the attenuation via a compliance relaxation function, all relevant physical effects are automatically included via the applied attenuation contrast source. From Eqs. (2.32) and (2.49) it follows that the function $\hat{A}(\mathbf{x}, s)$ in the attenuation contrast source in Eq. (2.36) is given by

$$\begin{aligned} \hat{A}(\mathbf{x}, s) = & \frac{2c_{bg}\alpha_1(\mathbf{x})s^{b(\mathbf{x})-1}}{\cos(\pi b(\mathbf{x})/2) [1 + (s/s_1)^d]} \\ & + \left\{ \frac{c_{bg}\alpha_1(\mathbf{x})s^{b(\mathbf{x})-1}}{\cos[\pi b(\mathbf{x})/2] [1 + (s/s_1)^d]} \right\}^2. \end{aligned} \quad (2.53)$$

Note that, in case spatially dependent speed of sound has to be modeled, c_{bg} has to be replaced with $c(\mathbf{x})$. Frequency domain results for $\hat{A}(\mathbf{x}, s)$ are obtained by taking $s = j2\pi f$, with f being the temporal frequency. As an example, $|\hat{A}(f)|$ is plotted in Fig. 2.1 for liver, brain, blood, and water.

Table 2.1: Acoustic medium parameters for water and several human tissues [6]. The relation between a and α_1 is $\alpha_1 = 100 \times a(2\pi)^{-b}$.

Medium	a [Np cm ⁻¹ MHz ^{-b}]	b [-]	c_{bg} [m s ⁻¹]	β [-]
liver	$5.2 \cdot 10^{-2}$	1.05	1578	4.38
brain	$6.7 \cdot 10^{-2}$	1.3	1562	4.28
blood	$1.6 \cdot 10^{-2}$	1.21	1584	4.00
water	$2.5 \cdot 10^{-4}$	2.0	1482.3	3.42

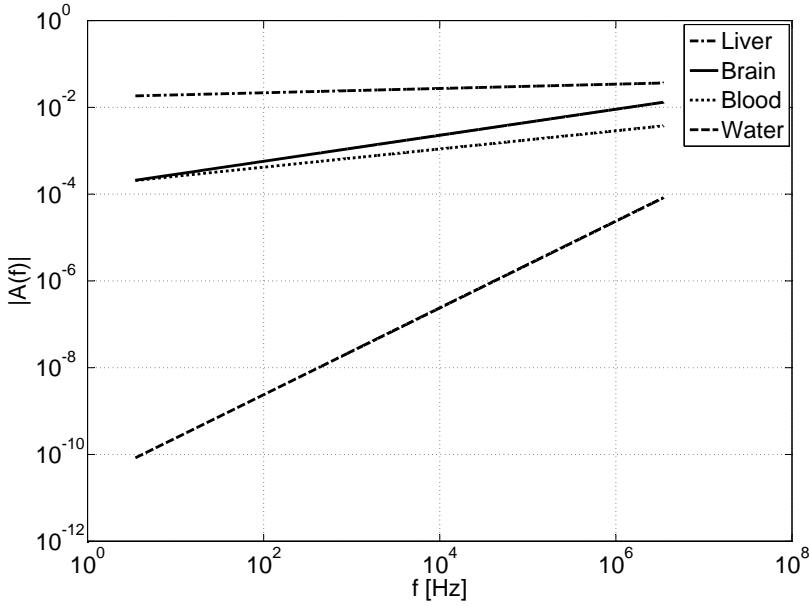


Figure 2.1: The modulus of $\hat{A}(f)$ versus frequency, for liver, brain, blood and water.

2.4 Contrast source approach

In the previous Sections we derived and discussed the characteristics of Eq. (2.43). Here, we formulate how Eq. (2.43) may be solved by means of a contrast source approach.

The wave equation for homogeneous lossless linear media, in presence of an arbitrary primary source $S_{\text{pr}}(\mathbf{x}, t)$, equals

$$\nabla^2 p(\mathbf{x}, t) - \frac{1}{c_{bg}^2} \partial_t^2 p(\mathbf{x}, t) = -S_{\text{pr}}(\mathbf{x}, t). \quad (2.54)$$

Solution in $p(\mathbf{x}, t)$ of Eq. (2.54) may be obtained via spatio-temporal convolution of the primary source $S_{\text{pr}}(\mathbf{x}, t)$ with the Green's function $G(\mathbf{x}, t)$, i.e. the pressure wave field $p(\mathbf{x}, t)$ equals

$$p(\mathbf{x}, t) = \int_{\mathcal{T}} \int_{\mathcal{D}} G(\mathbf{x} - \mathbf{x}', t - t') S_{\text{pr}}(\mathbf{x}', t') d\mathbf{x}' dt', \quad (2.55)$$

with \mathcal{T} and \mathcal{D} being the temporal and spatial domain of integration respectively. The Green's function represents the impulsive response of the system and is obtained as a solution of the wave equation in presence of a delta source $\delta(\mathbf{x})\delta(t)$:

$$\nabla^2 G(\mathbf{x}, t) - \frac{1}{c_{bg}^2} \partial_t^2 G(\mathbf{x}, t) = -\delta(\mathbf{x})\delta(t). \quad (2.56)$$

For homogeneous lossless linear media the Green's function $G(\mathbf{x}, t)$ equals

$$G(\mathbf{x}, t) = \frac{\delta(t - \frac{\|\mathbf{x}\|}{c_{bg}})}{4\pi\|\mathbf{x}\|}, \quad (2.57)$$

with $\|\mathbf{x}\|$ the length of \mathbf{x} . The Green's function is also known for homogeneous lossy linear media. In this case this function may most conveniently be derived in the space-frequency domain [1, 32].

Following this approach, the contrast source in Eq. (2.43) may be considered a distributed source [1, 2, 31]. Hence, for nonlinear inhomogeneous media, the resulting pressure wave field $p(\mathbf{x}, t)$ is given by an integral equation, which equals

$$\begin{aligned} p(\mathbf{x}, t) &= \int_{\mathcal{T}} \int_{\mathcal{D}} G(\mathbf{x} - \mathbf{x}', t - t') \{S_{\text{pr}}(\mathbf{x}', t') + S_{\text{cs}}[p(\mathbf{x}', t')]\} d\mathbf{x}' dt' \\ &= p^{(0)}(\mathbf{x}, t) + \int_{\mathcal{T}} \int_{\mathcal{D}} G(\mathbf{x} - \mathbf{x}', t - t') S_{\text{cs}}[p(\mathbf{x}', t')] d\mathbf{x}' dt', \end{aligned} \quad (2.58)$$

with $p^{(0)}(\mathbf{x}, t)$ being the known linear homogeneous attenuated pressure wave field obtained by the spatio-temporal convolution of the known primary source $S_{\text{pr}}(\mathbf{x}, t)$ with the known Green's function of the homogeneous lossy linear background medium, $G(\mathbf{x}, t)$. This equation represents the starting point of our model and may be solved by means of iterative schemes. In this thesis different schemes will be applied to solve Eq. (2.58), i.e. Neumann, Bi-CGSTAB and Steepest Descent.

Chapter 3

Neumann scheme

In this Chapter, the contrast source problem formulated in Chapter 2 is solved by employing the Neumann iterative solution method. First, the solution method is introduced. Second, results obtained via application of this method are presented and discussed.

3.1 Solution method

In Chapter 2, an integral equation is derived, see Eq. (2.58), which equals

$$\begin{aligned} p(\mathbf{x}, t) &= \int_{\mathcal{T}} \int_{\mathcal{D}} G(\mathbf{x} - \mathbf{x}', t - t') \{S_{\text{pr}}(\mathbf{x}', t') + S_{\text{cs}}[p(\mathbf{x}', t')]\} d\mathbf{x}' dt' \\ &= p^{(0)}(\mathbf{x}, t) + \int_{\mathcal{T}} \int_{\mathcal{D}} G(\mathbf{x} - \mathbf{x}', t - t') S_{\text{cs}}[p(\mathbf{x}', t')] d\mathbf{x}' dt'. \end{aligned} \quad (3.1)$$

This integral equation describes a contrast source problem with known acoustic medium parameters and primary source, and unknown acoustic pressure wave field. This problem is referred to as a forward wave problem in the literature. In this Section, it is shown that for weak contrasts this problem may be solved by employing the Neumann iterative solution method.

3.1.1 Neumann scheme

Equation (3.1) may be rewritten as

$$p(\mathbf{x}, t) = G(\mathbf{x}, t) *_{\mathbf{x}, t} \{S_{\text{pr}}(\mathbf{x}, t) + S_{\text{cs}}[p(\mathbf{x}, t)]\}. \quad (3.2)$$

Here, $*_{\mathbf{x},t}$ denotes a convolution over space and time. As the contrast source $S_{cs}[p(\mathbf{x}, t)]$ is a function of the unknown pressure field $p(\mathbf{x}, t)$, Eq. (3.2) forms an integral equation. For weak contrasts Eq. (3.2) may be solved via the Neumann iterative solution

$$p^{(0)}(\mathbf{x}, t) = G(\mathbf{x}, t) *_{\mathbf{x},t} S_{pr}(\mathbf{x}, t), \quad (3.3)$$

$$\begin{aligned} p^{(n)}(\mathbf{x}, t) &= G(\mathbf{x}, t) *_{\mathbf{x},t} \left\{ S_{pr}(\mathbf{x}, t) + S_{cs} \left[p^{(n-1)}(\mathbf{x}, t) \right] \right\} \\ &= p^{(0)}(\mathbf{x}, t) + G(\mathbf{x}, t) *_{\mathbf{x},t} S_{cs} \left[p^{(n-1)}(\mathbf{x}, t) \right], (n > 0). \end{aligned} \quad (3.4)$$

This scheme defines the Neumann expansion [34] of the acoustic pressure field. After discretization with respect to space and time, the following discrete Neumann scheme is obtained

$$\mathbf{p}^{(0)} = \mathbf{G} S_{pr}, \quad (3.5)$$

$$\begin{aligned} \mathbf{p}^{(n)} &= \mathbf{G} \left[S_{pr} + S_{cs} \left[\mathbf{p}^{(n-1)} \right] \right] \\ &= \mathbf{p}^{(0)} + \mathbf{G} \left[S_{cs} \left[\mathbf{p}^{(n-1)} \right] \right], (n > 0), \end{aligned} \quad (3.6)$$

in which the vector $\mathbf{p}^{(n)}$ contains the n th order approximation of the acoustic pressure field at discrete grid points that spans the spatio-temporal computational domain. \mathbf{G} is the discrete Green's function that is convolved with the discrete source terms S_{pr} and $S_{cs}[\mathbf{p}^{(n)}]$.

3.1.2 Convergence

Any iterative scheme applied to solve a given problem, requires a criterion that will be used to decide when to stop the iterative process. With respect to the Neumann solution method, convergence is known to depend on the magnitude and the spatial extent of the contrast source. For a theoretical analysis of the convergence of the scheme, the reader is referred to the literature [53]. To verify the numerical convergence of the Neumann scheme towards the solution of the formulated contrast source problem, a normalized error $\text{Err}_1^{(n)}$ is introduced, which equals

$$\text{Err}_1^{(n)} = \frac{\|\mathbf{p}^{(0)} + \mathbf{G} [S_{cs} [\mathbf{p}^{(n-1)}]] - \mathbf{p}^{(n-1)}\|}{\|\mathbf{p}^{(0)}\|}, \quad (3.7)$$

$$= \frac{\|\mathbf{p}^{(n)} - \mathbf{p}^{(n-1)}\|}{\|\mathbf{p}^{(0)}\|}, \quad (3.8)$$

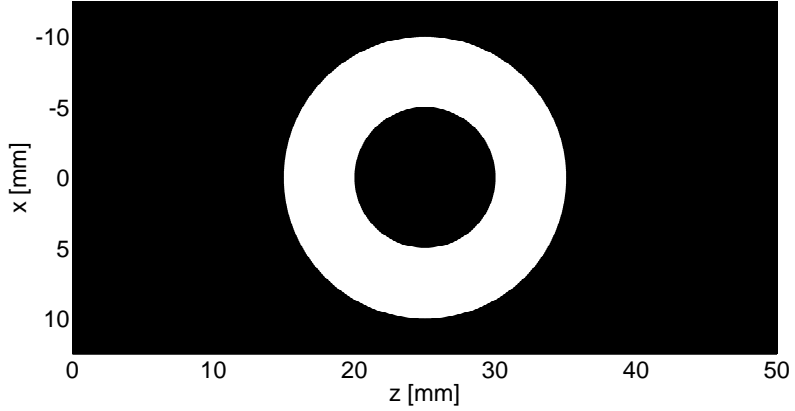


Figure 3.1: Cross-section of the spatial domain \mathcal{D} for configuration 1 along the xz -plane. Black indicates the linear lossless background medium, white indicates the nonlinear object.

with $\|\cdot\|$ the Euclidian length. When $\text{Err}_1^{(n)}$ is decreasing towards zero for increasing n , the obtained solution is converging towards the solution of the formulated contrast source problem [54]. The stop criterion can, therefore, be defined as follows: the iterative process is stopped at the iteration n that gives a normalized error value below a given threshold.

3.2 Results

In this section, two configurations are used to demonstrate the numerical performance of the method presented. First, results as obtained for a plane wave propagating through lossless media with inhomogeneities in the coefficient of nonlinearity are presented and discussed. This is referred to as configuration 1. Second, results as obtained for the pressure wave field generated by a linear array have been computed for different lossy and lossless media exhibiting inhomogeneity in the attenuation. This is referred to as configuration 2. See Appendix B for

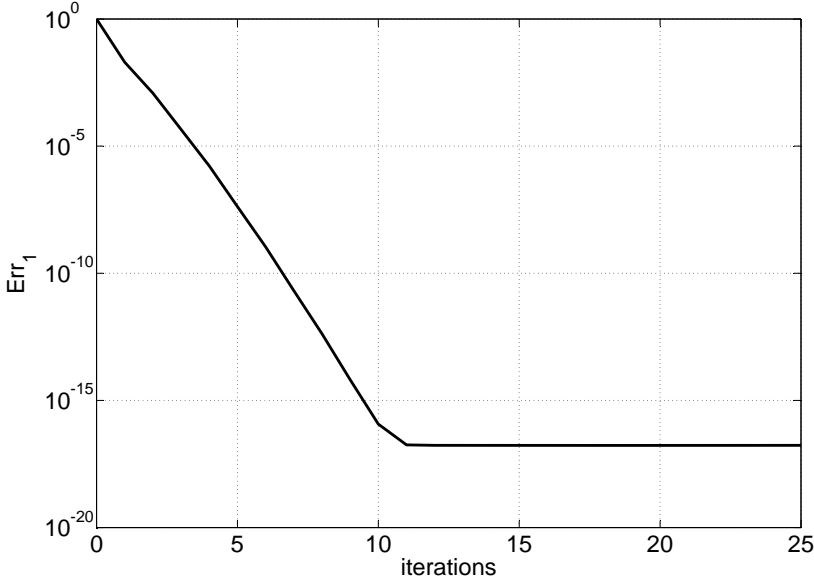


Figure 3.2: Normalized error $\text{Err}_1^{(n)}$ for configuration 1.

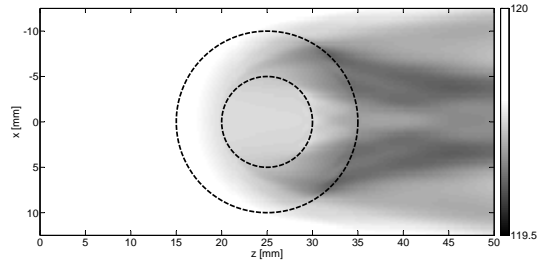
a schematic diagram summarizing the utilized configurations. All results have been obtained up to the third harmonic component. The k th harmonic pressure wave field has been obtained by filtering the total pressure wave field with an 8th order Butterworth filter having a center frequency equal to kf_0 and cut-off frequencies equal to $(\pm 0.4 + k)f_0$, with f_0 the fundamental center frequency. For the fundamental pressure wave field $k = 1$. Convergence has been investigated for the two configurations described.

3.2.1 Configuration 1

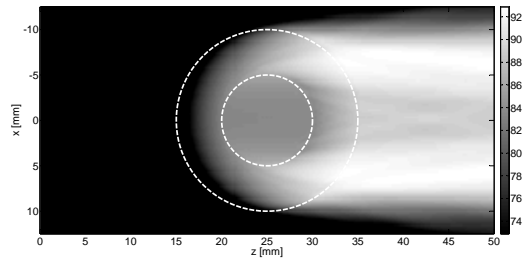
Here, a plane wave is considered. This plane wave is modulated by a Gaussian pulse resulting in a pressure field, which in the plane $z = 0$ mm equals:

$$p(t) = P_0 e^{-(2t/t_w)^2} \sin(2\pi f_0 t), \quad (3.9)$$

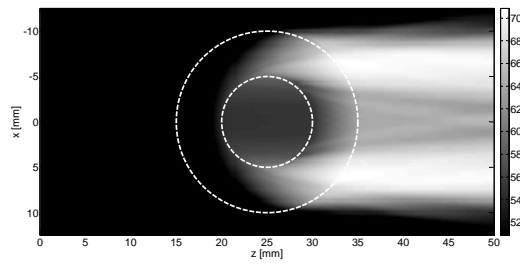
where the time width $t_w = 3/f_0$ and the center frequency $f_0 = 1$ MHz. The envelope of this signal contains about six cycles of the harmonic signal [2]. The peak pressure considered is $P_0 = 1$ MPa. Configuration 1 contains a contrast in the coefficient of nonlinearity, modeled as lossless nonlinear liver, embedded in



(a)



(b)



(c)

Figure 3.3: Two-dimensional spectral profiles of the pressure wave field in configuration 1 with lossless linear liver and nonlinear inhomogeneities; (a) fundamental, (b) second and (c) third harmonic component. The plane of observation is $y = 0$ mm. The pressure values are expressed in dB relative to 1 Pa.

Table 3.1: Acoustic medium parameters for water and several human tissues [6]. The relation between a and α_1 is $\alpha_1 = 100 \times a(2\pi)^{-b}$.

Medium	a [Np cm ⁻¹ MHz ^{-b}]	b [-]	c_{bg} [m s ⁻¹]	β [-]
liver	$5.2 \cdot 10^{-2}$	1.05	1578	4.38
‘linearized’ liver	$5.2 \cdot 10^{-2}$	1.05	1578	0
brain	$6.7 \cdot 10^{-2}$	1.3	1562	4.28
‘linearized’ brain	$6.7 \cdot 10^{-2}$	1.3	1562	0
blood	$1.6 \cdot 10^{-2}$	1.21	1584	4.00
‘linearized’ blood	$1.6 \cdot 10^{-2}$	1.21	1584	0
water	$2.5 \cdot 10^{-4}$	2.0	1482.3	3.42
‘linearized’ water	$2.5 \cdot 10^{-4}$	2.0	1482.3	0

lossless ($a = 0$) ‘linearized’ ($\beta = 0$) liver (See Table 3.1). This configuration is used to demonstrate the capability of the method presented to model spatially varying coefficient of nonlinearity. The dimensions of the spatial computational domain \mathcal{D} are $(x \times y \times z) = (25 \text{ mm} \times 20 \text{ mm} \times 50 \text{ mm})$. A cross-section of the spatial domain \mathcal{D} along the xz -plane is shown in Fig. 3.1. Black indicates the linear lossless background medium, white indicates the nonlinear object.

Convergence

The convergence of the Neumann scheme is tested using the normalized error $\text{Err}_1^{(n)}$. Results are presented in Fig. 3.2. The graph shows that convergence has been obtained after 11 iterations. At this point, the normalized error level has reached a value of $\text{Err}_1^{(11)} \approx 10^{-16}$ and remains flat afterwards.

In silico experiments

Figure 3.3 shows two-dimensional spectral profiles of the pressure wave field as obtained for configuration 1 with lossless linear liver and nonlinear inhomogeneities; (a) fundamental, (b) second and (c) third harmonic component. The plane of observation is $y = 0 \text{ mm}$. The pressure values are expressed in dB relative to 1 Pa. The contours of the nonlinear object are represented by the dotted lines. As can be seen, the amplitude of the incident plane wave decays as soon as it enters the nonlinear contrast. On the other hand, harmonics emerge only in this

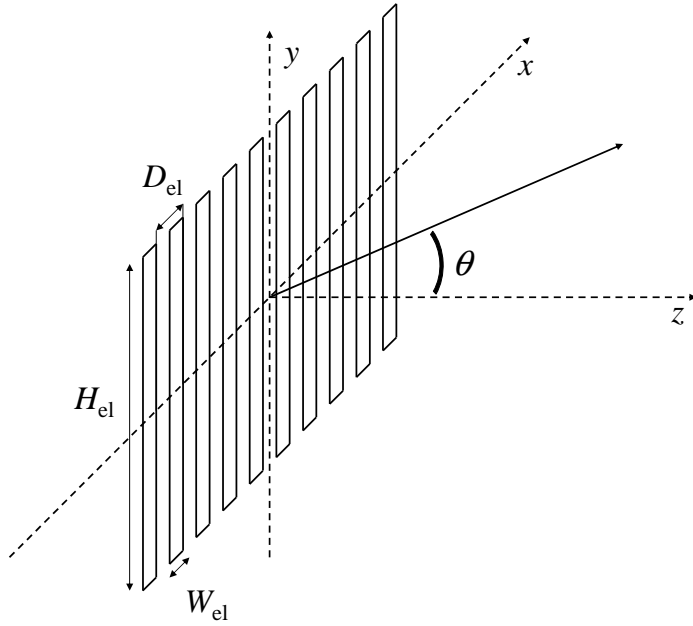


Figure 3.4: The geometry of the phased array source. The number of elements is $N_{el} = 10$. The dimensions of each element are $W_{el} = 0.25$ mm by $H_{el} = 10$ mm, and the pitch is $D_{el} = 1$ mm.

part of the simulated domain and they keep propagating afterwards. Note that the colorbar for the fundamental spectral profile is kept in between 119.5 and 120 dB relative to 1 Pa to show its decay in space. The colorbars for the harmonic components go from the maximum relative value to -20 dB below this value. The cumulative nature of nonlinear propagation can be observed in these figures; the growth of the harmonic components begins sooner for the lower harmonics and keeps increasing along the path where the pressure field propagates nonlinearly.

3.2.2 Configuration 2

In this configuration a realistic source is considered, i.e. a linear phased array. The origin of the coordinate system is located at the center of the transducer. A graphical representation of the source is given in Fig. 3.4. The array consists of $N_{el} = 10$ elements. The dimensions of the elements are $W_{el} = 0.25$ mm by

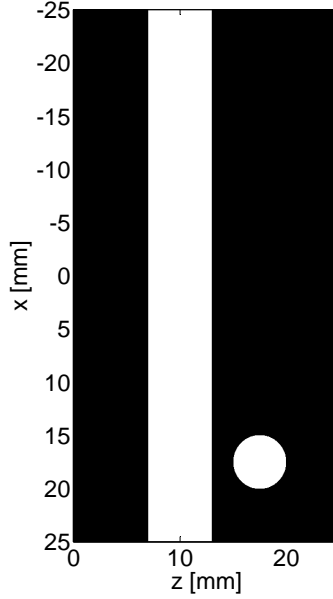


Figure 3.5: Cross-section of the spatial domain \mathcal{D} for scenario 2b along the xz -plane. Black indicates the lossless background medium (lossless nonlinear liver), white indicates the lossy objects (lossy nonlinear liver).

$H_{el} = 10$ mm, and the pitch is $D_{el} = 1$ mm. The elements are excited with a pulse consisting of an harmonic signal with a frequency $f_0 = 1$ MHz that is amplitude modulated by a Gaussian pulse with a width $t_w = 3/f_0$. This envelope contains about six cycles of the harmonic signal [2]. The peak pressure at the surface of each transducer element is $P_0 = 0.5$ MPa. No focusing is applied.

Configuration 2 is used for two different scenarios and we will refer to them as scenario 2a and 2b. Scenario 2a only considers homogeneous lossy (either linear or nonlinear) media (liver, brain, blood, water) and is used to investigate which effect attenuation has on the convergence of the scheme. Hence, even though we are considering homogeneous media, attenuation has been modeled using the contrast source approach. No beam steering is applied, and the dimensions of the spatial computational domain \mathcal{D} are $(x \times y \times z) = (25 \text{ mm} \times 20 \text{ mm} \times 50 \text{ mm})$. Scenario 2b contains lossy objects (lossy nonlinear liver) embedded in a corresponding lossless background medium (lossless nonlinear liver), see Fig. 3.5. This

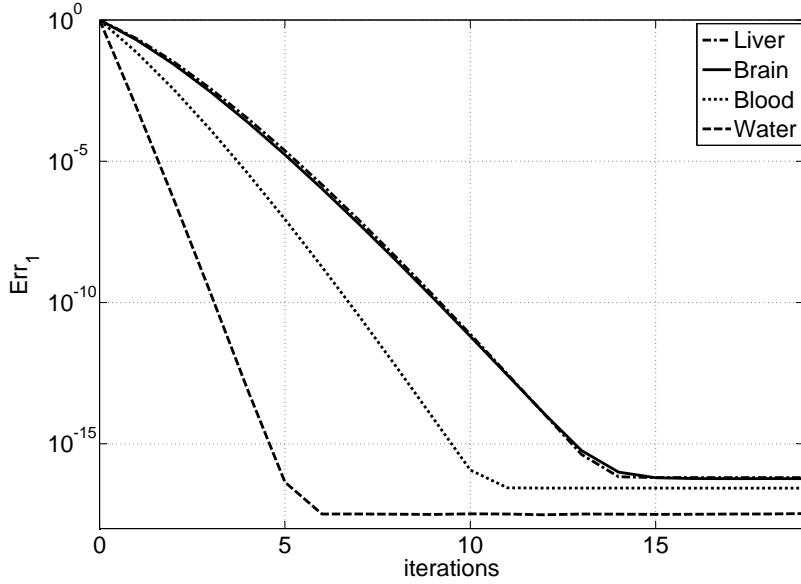


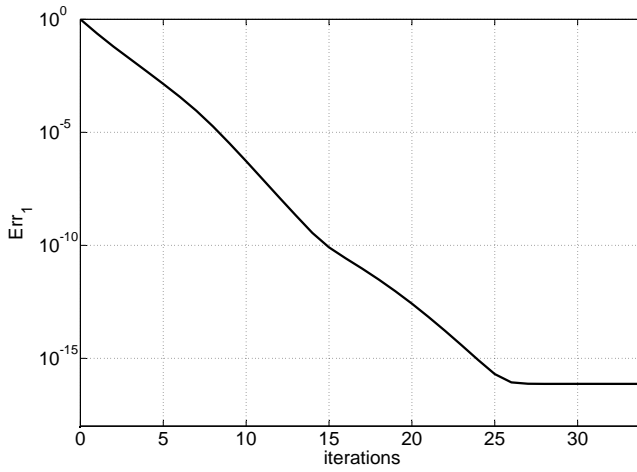
Figure 3.6: Normalized error $\text{Err}_1^{(n)}$ for scenario 2a containing "linearized" ($\beta = 0$) liver, brain, blood, and water.

configuration is used to demonstrate the capability of the method presented to model spatially varying attenuation. The transducer beam is steered over an angle $\theta = 45^\circ$, and the spatial computational domain \mathcal{D} measures $(x \times y \times z) = (50 \text{ mm} \times 20 \text{ mm} \times 25 \text{ mm})$. The steering angle θ is defined in the plane $y = 0 \text{ mm}$, is measured with respect to the normal of the transducer surface and is positive for positive x .

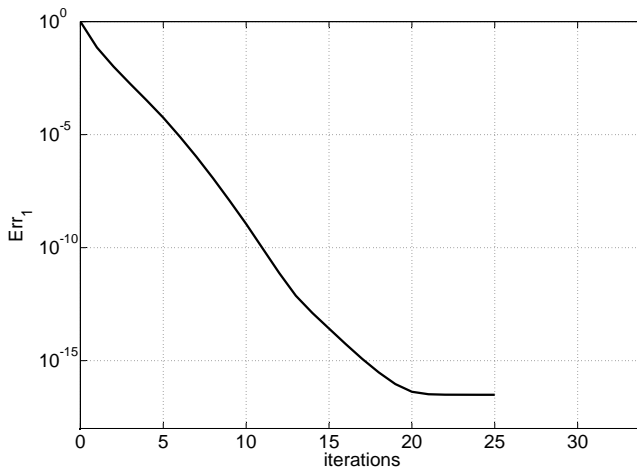
Convergence

The convergence of the Neumann scheme is tested for different types of media using the normalized error $\text{Err}_1^{(n)}$, see Table 3.1 for acoustic medium parameters.

First, scenario 2a is investigated. In order to focus on the effect of attenuation, the media are considered to be lossy and linear ($\beta = 0$). Results are presented in Fig. 3.6. The graphs show that media with less attenuation require significantly fewer iterations to reach an error $\text{Err}_1^{(n)} \approx 10^{-16}$, than media with strong attenuation; i.e. five iterations for weakly attenuative water, and 14 iterations for

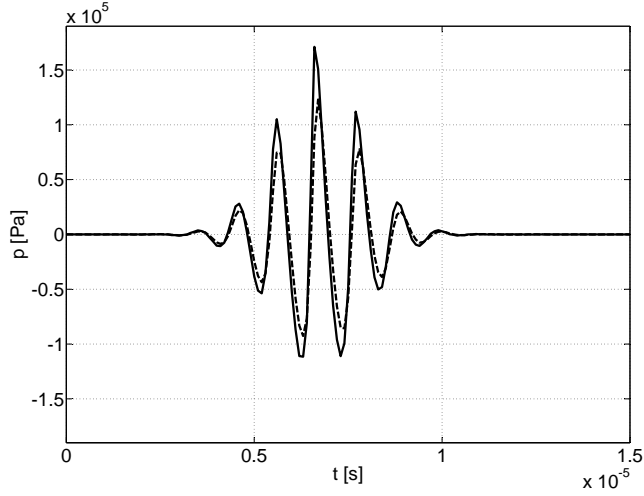


(a)

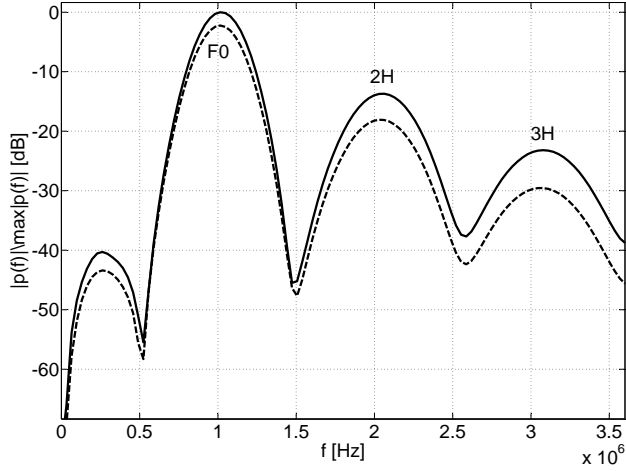


(b)

Figure 3.7: Normalized error $\text{Err}_1^{(n)}$; (a) for scenario 2a (homogeneous lossy nonlinear liver), (b) for scenario 2b (lossy nonlinear liver objects in a lossless nonlinear liver background).

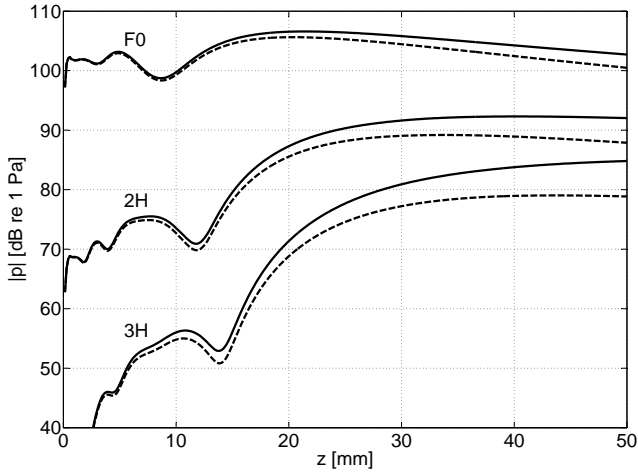


(a)

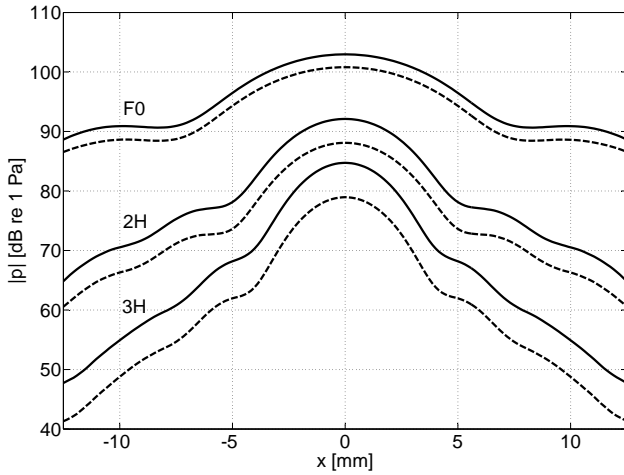


(b)

Figure 3.8: The nonlinear pressure wave in scenario 2a with lossless (solid line) and lossy (dashed line) nonlinear liver; (a) time domain pulses, (b) normalized frequency domain spectra. The point of observation is $(x, y, z) = (0 \text{ mm}, 0 \text{ mm}, 50 \text{ mm})$. The graphs show the fundamental (F0), second harmonic (2H), and third harmonic (3H) component.



(a)



(b)

Figure 3.9: The nonlinear pressure field in scenario 2a with lossless (solid line) and lossy (dashed line) nonlinear liver; (a) axial profile evaluated along the z -axis, (b) lateral profile evaluated along the line $(y, z) = (0 \text{ mm}, 50 \text{ mm})$. The graphs show the fundamental (F0), second harmonic (2H), and third harmonic (3H) component.

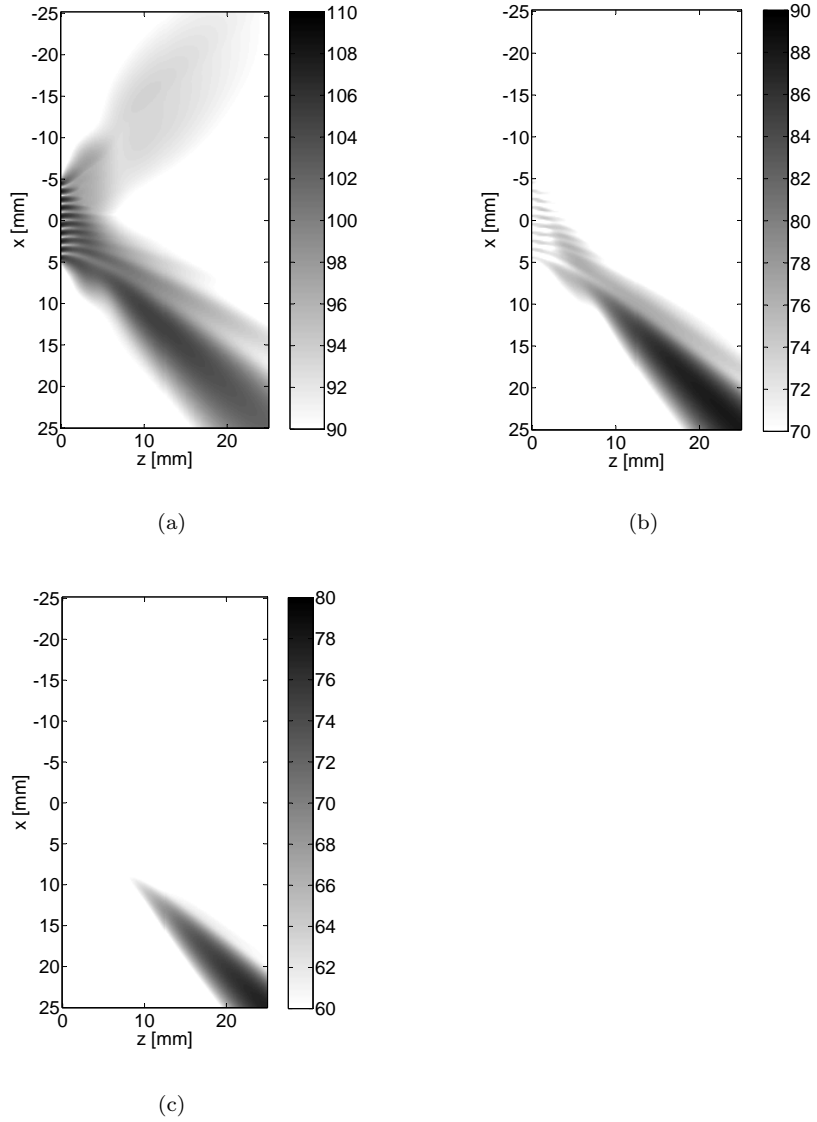
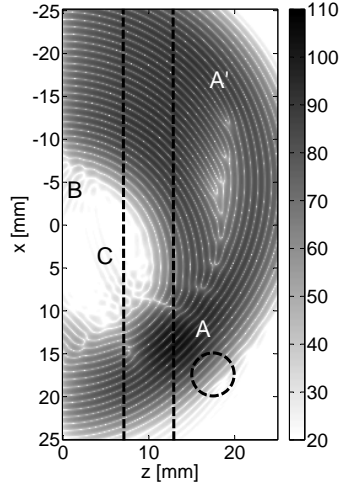
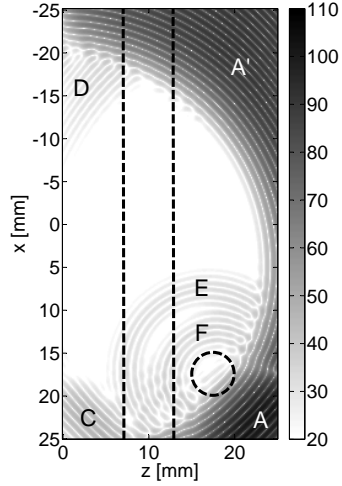


Figure 3.10: Two-dimensional spectral profiles of the pressure wave field in scenario 2b with lossless nonlinear liver and lossy inhomogeneities; (a) fundamental, (b) second harmonic, (c) third harmonic. The plane of observation is $y = 0$ mm. The pressure values are expressed in dB relative to 1 Pa.



(a)



(b)

Figure 3.11: Snapshots of the propagating pressure pulse in scenario 2b with lossless nonlinear liver (background) and lossy inhomogeneities (dashed objects); (a) early time, (b) late time. The plane of observation is $y = 0$ mm. The labels refer to the phenomena described in the text, and in Table 3.2. The pressure values are expressed in dB relative to 1 Pa.

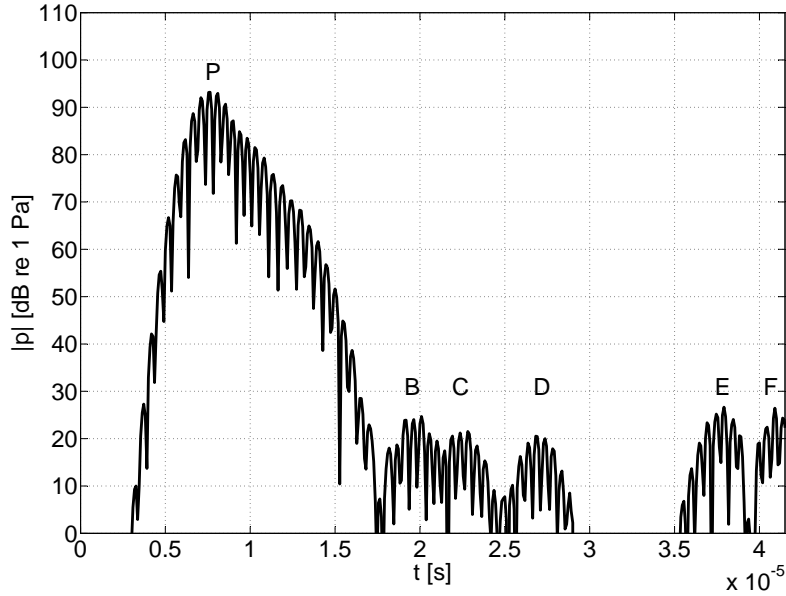


Figure 3.12: Pressure versus time at the origin of the coordinate system in scenario 2b with lossless nonlinear liver and lossy inhomogeneities. The point of observation is $(x, y, z) = (0 \text{ mm}, 0 \text{ mm}, 0 \text{ mm})$. The labels refer to the phenomena described in the text, and in Table 3.2.

highly lossy brain tissue. In addition, it is shown that the normalized error flattens after it reaches this value. Next, the convergence of the Neumann scheme for nonlinear lossy media is investigated by considering scenario 2a containing lossy nonlinear liver, and scenario 2b containing lossy nonlinear liver objects in a lossless nonlinear liver background. Note that a lossless Green's function has been used in both scenarios. The results are presented in Fig. 3.7. For scenario 2a, the flattening of $\text{Err}_1^{(n)}$ is reached within 26 iterations, whereas scenario 2b requires only 19 iterations. The difference may well be caused by the fact that, unlike scenario 2a, scenario 2b has an attenuation contrast source that is zero outside the objects, resulting in a smaller volume of the total contrast source.

In silico experiments

Fig. 3.8 shows time signal and normalized frequency spectrum as obtained in scenario 2a with both lossless ($a = 0$), and lossy nonlinear liver. Figure 3.8(a) shows

the time domain pressure pulses in the point $(x, y, z) = (0 \text{ mm}, 0 \text{ mm}, 50 \text{ mm})$. The normalized frequency spectra of these pulses are shown in Fig. 3.8(b), where the fundamental (F0), the second harmonic (2H), and the third harmonic (3H) component of the pressure wave field are clearly visible. Normalization is performed with respect to the maximum absolute value of the lossless spectrum. Both figures clearly show a reduction of the amplitude of the pressure wave when attenuation is taken into account. The frequency dependent nature of the attenuation is visible in Fig. 3.8(b), in which an increase in attenuation is observed for increasing frequency. This is in agreement with the behavior of $\hat{A}(f)$ for liver, as shown in Fig. 2.1.

Figure 3.9 shows the axial and lateral spectral profiles of the pressure field that is generated in scenario 2a with lossless and lossy nonlinear liver. The axial profiles in Fig. 3.9(a) are evaluated along the z -axis, and the lateral profiles in Fig. 3.9(b) are evaluated along the line $(y, z) = (0 \text{ mm}, 50 \text{ mm})$. In both panels, the increase of attenuation for the higher harmonics is clearly visible. The cumulative nature of the nonlinear effect may be observed in Fig. 3.9(a), which shows the growth of the amplitudes of the harmonics with depth. In Fig. 3.9(b), two effects are recognizable that are connected to nonlinear propagation and that are utilized in medical applications to improve the quality of ultrasound images. First, if the ratio between the amplitude of the main and side lobes is considered, a reduction of this ratio is observed for increasing harmonics. Second, for increasing harmonics, the width of the main beam decreases. In particular, the -3 dB beamwidth is 6.9 mm for the fundamental, 4.3 mm for the second harmonic, and 3.4 mm for the third harmonic.

Figure 3.10 shows the two-dimensional spectral profiles of the nonlinear pressure field in the plane $y = 0 \text{ mm}$ for scenario 2b with lossy (objects) and lossless nonlinear liver (background). The results clearly show that, for increasing harmonics, the size of the focal area is reduced, the amplitude of the grating lobes is strongly diminished, and that possible undesired reflections from objects close to the transducer disappear. Note that grating lobes and related effects can only be modeled accurately when it is possible to compute pressure wave fields over a wide angle. The INCS method allows to do this accurately since no *a priori* assumption on the directivity of the wave field is used [1, 2].

Two snapshots of the pressure wave propagating in scenario 2b are shown

Table 3.2: Acoustical phenomena present in Figs. 3.11 and 3.12.

Character	Acoustical phenomenon
A	Main beam
A'	Grating lobe
B	Reflection from the front of the slab
C-D	Reflection from the back of the slab
E	Reflection from the front of the cylinder
F	Reflection from the back of the cylinder
P	Direct field of the transducer

in Fig. 3.11. The fields are presented for the plane $y = 0$ mm. In Fig. 3.12, pressure versus time at the origin of the coordinate system is shown. In both Figs. 3.11 and 3.12, the characters A to P are used to mark specific phenomena (see Table 3.2). The generated pressure wave field P (Fig. 3.12 only) originates from the transducer and travels through the lossless background. Part of the pressure wave field contributes to the formation of the main beam A and another part to the formation of the grating lobe A' (Fig. 3.11 only). Furthermore, when the pressure wave field encounters an interface between the background and the inhomogeneities, part of the field propagates through and part is backscattered. Specifically, B marks the backscattered pressure wave field caused by the front of the lossy slab, C and D mark the backscattered field caused by the back of the lossy slab and E and F mark the backscattered field caused by the front and the back of the cylinder respectively.

3.3 Conclusions

In this Chapter, a method for modeling nonlinear wave field propagation through biomedical media with spatially varying attenuation and coefficient of nonlinearity has been presented. This method utilizes a Neumann iterative scheme, which is used to solve an integral equation where contrast sources are used to model inhomogeneities in the coefficient of nonlinearity and attenuation. As it is an extension of the INCS method, it is able to solve accurately the full wave equation for the weakly to moderately nonlinear, wide-angle, pulsed, acoustic wave field, in a large three-dimensional domain.

First, the convergence of the method has been investigated. Numerical results show convergence towards the solution of the formulated contrast source problem and how the contrast determines the convergence rate of the scheme. The stronger the contrast, e.g. when modeling stronger attenuating media, the more iterations are required to reach convergence.

Second, numerical results have been generated to demonstrate the capability of the method to model nonlinear pressure wave fields propagating through media presenting spatially varying coefficient of nonlinearity and frequency dependent attenuation, as the case in most biomedical tissue. Moreover, *in silico* experiments show the capability of the method to deal with scattering.

In conclusion, the Neumann scheme represents an intuitive and easily implementable iterative scheme that allows to deal with moderate losses and nonlinearity. Nevertheless, for stronger contrast, convergence may no longer be assured. Therefore, to extend the method to deal with strong losses or realistic inhomogeneities in the speed of sound, alternative schemes have to be investigated. In the next Chapters two alternative approaches are proposed and discussed.

Bi-CGSTAB scheme

When strong contrast sources are considered, e.g. in case of strongly attenuating inhomogeneous media, the Neumann iterative solution method presented in Chapter 3 can be slowly convergent or may even diverge. Consequently, to deal with a broader variety of configurations, a different iterative scheme is required. The ideal iterative scheme should, when compared to Neumann, provide a faster convergence, be capable to cope with stronger contrast and have a reduced complexity and computational cost per iteration. Bi-CGSTAB [55] meets the first two requirements. Unfortunately, it is only applicable to linear problems. Therefore, the nonlinear integral equation derived in Chapter 2:

$$p(\mathbf{x}, t) = p^{(0)}(\mathbf{x}, t) + \int_{\mathcal{T}} \int_{\mathcal{D}} G(\mathbf{x} - \mathbf{x}', t - t') S_{cs}[p(\mathbf{x}', t')] d\mathbf{x}' dt', \quad (4.1)$$

has to be linearized [56, 57].

In this Chapter, a linearized version of Eq. (4.1) is derived, discussed and solved by means of a Bi-CGSTAB iterative solution method. First, the rationale behind the linearization is described. Second the solution method is introduced. Third, results obtained via application of this approach are presented, discussed and compared with results obtained via Neumann scheme.

4.1 Linearization

As described in Chapter 2, the nonlinear propagation of acoustic wave fields through lossy inhomogeneous media may be described using a nonlinear wave

equation:

$$\begin{aligned} \nabla^2 p(\mathbf{x}, t) - \frac{1}{c_{bg}^2} \partial_t^2 [m_{bg}(t) *_t p(\mathbf{x}, t)] = -S_{pr}(\mathbf{x}, t) \\ - S_{nl} [p(\mathbf{x}, t)] - S_{nl\kappa} [p(\mathbf{x}, t)] - S_c [p(\mathbf{x}, t)] - S_{at} [p(\mathbf{x}, t)], \end{aligned} \quad (4.2)$$

with

$$S_{pr}(\mathbf{x}, t) = \rho_{bg} \partial_t q(\mathbf{x}, t) - \nabla \cdot \mathbf{f}(\mathbf{x}, t), \quad (4.3)$$

$$S_{nl} [p(\mathbf{x}, t)] = \rho_{bg} \kappa^2(\mathbf{x}) \beta(\mathbf{x}) \partial_t^2 p^2(\mathbf{x}, t), \quad (4.4)$$

$$S_{nl\kappa} [p(\mathbf{x}, t)] = \frac{1}{2} \nabla \cdot \{ [\nabla \kappa(\mathbf{x})] p^2(\mathbf{x}, t) \}, \quad (4.5)$$

$$S_c [p(\mathbf{x}, t)] = \left[\frac{1}{c_{bg}^2} - \frac{1}{c^2(\mathbf{x})} \right] \partial_t^2 [m_{bg}(t) *_t p(\mathbf{x}, t)], \quad (4.6)$$

$$S_{at} [p(\mathbf{x}, t)] = -\frac{1}{c^2(\mathbf{x})} \partial_t^2 [\Delta m(\mathbf{x}, t) *_t p(\mathbf{x}, t)]. \quad (4.7)$$

The sources defined in Eqs. (4.3) to (4.7) can be divided into three categories. The first category contains sources that are independent on the unknown $p(\mathbf{x}, t)$, i.e. $S_{pr}(\mathbf{x}, t)$, the second category contains contrast sources that linearly depend on the unknown quantity $p(\mathbf{x}, t)$, i.e. $S_c(\mathbf{x}, t)$ and $S_{at}(\mathbf{x}, t)$, and the third category contains contrast sources that depend nonlinearly on $p(\mathbf{x}, t)$, i.e. $S_{nl} [p(\mathbf{x}, t)]$ and $S_{nl\kappa} [p(\mathbf{x}, t)]$. To linearize Eq. (4.2), the *nonlinear* contrast sources have to be reformulated such that they fall in the first or second category.

The linearization presented in this section is based on the assumption that the total acoustic wave field $p(\mathbf{x}, t)$ may be considered the combination of a primary contribution $p^{(0)}(\mathbf{x}, t)$ and a secondary contribution $\tilde{p}(\mathbf{x}, t)$, which represents the perturbation to the linear incident field $p^{(0)}(\mathbf{x}, t)$. In view of the smallness of $\tilde{p}(\mathbf{x}, t)$ with respect to $p^{(0)}(\mathbf{x}, t)$, it is assumed that $p^2(\mathbf{x}, t)$ may be approximated by [56, 57]

$$\begin{aligned} p^2(\mathbf{x}, t) &= [p^{(0)}(\mathbf{x}, t) + \tilde{p}(\mathbf{x}, t)]^2 \approx [p^{(0)}(\mathbf{x}, t)]^2 + 2p^{(0)}(\mathbf{x}, t)\tilde{p}(\mathbf{x}, t) \\ &= -[p^{(0)}(\mathbf{x}, t)]^2 + 2p^{(0)}(\mathbf{x}, t)p(\mathbf{x}, t). \end{aligned} \quad (4.8)$$

Substitution of Eq. (4.8) into Eqs. (4.4) and (4.5) allows to reformulate the two

contrast sources as

$$S_{\text{nl}}^{\text{new}} [p(\mathbf{x}, t)] = \rho_{bg} \kappa^2(\mathbf{x}) \beta(\mathbf{x}) \partial_t^2 \left\{ - \left[p^{(0)}(\mathbf{x}, t) \right]^2 + 2p^{(0)}(\mathbf{x}, t)p(\mathbf{x}, t) \right\}, \quad (4.9)$$

$$S_{\text{nl}\kappa}^{\text{new}} [p(\mathbf{x}, t)] = \frac{1}{2} \nabla \cdot \left\{ [\nabla \kappa(\mathbf{x})] \left\{ - \left[p^{(0)}(\mathbf{x}, t) \right]^2 + 2p^{(0)}(\mathbf{x}, t)p(\mathbf{x}, t) \right\} \right\}. \quad (4.10)$$

The linearized form of the nonlinear wave equation presented in Eq. (4.2) is therefore formulated as

$$\nabla^2 p(\mathbf{x}, t) - \frac{1}{c_{bg}^2} \partial_t^2 [m_{bg}(t) *_t p(\mathbf{x}, t)] = -S_{\text{pr}}(\mathbf{x}, t) - S_{\text{cs}}^{\text{new}} [p(\mathbf{x}, t)], \quad (4.11)$$

with

$$S_{\text{cs}}^{\text{new}} [p(\mathbf{x}, t)] = S_{\text{nl}}^{\text{new}} [p(\mathbf{x}, t)] + S_{\text{nl}\kappa}^{\text{new}} [p(\mathbf{x}, t)] + S_{\text{c}} [p(\mathbf{x}, t)] + S_{\text{at}} [p(\mathbf{x}, t)]. \quad (4.12)$$

Eqs. (4.11) in combination with (4.12) is referred to as the linearized wave equation.

4.2 Solution method

Equations (4.11) and (4.12) describe a linearized wave equation with known acoustic medium parameters and primary source, and unknown acoustic pressure wave field. In this Section, a solution method based on the Bi-CGSTAB iterative solution scheme is presented.

4.2.1 Bi-CGSTAB scheme

The linearized nonlinear wave equation, Eq. (4.11), may be recast into an integral equation which reads

$$p(\mathbf{x}, t) = G(\mathbf{x}, t) *_t \{ S_{\text{pr}}(\mathbf{x}, t) + S_{\text{cs}}^{\text{new}} [p(\mathbf{x}, t)] \}. \quad (4.13)$$

Here, $G(\mathbf{x}, t)$ is the known Green's function of the homogeneous lossy linear background medium and $*_{\mathbf{x}, t}$ represents a convolution over space and time. After discretization, Eq. (4.13) can be written as

$$\mathbf{p} = \mathbf{G} [S_{\text{pr}} + S_{\text{cs}}^{\text{new}} [\mathbf{p}]]. \quad (4.14)$$

Here, \mathbf{G} is the operator that convolves the discrete Green's function of the homogeneous lossy linear background medium with the discrete sources. As Eq. (4.14)

Algorithm 1 The Bi-CGSTAB solution method

```

 $\mathbf{p}^{(n)} = 0 (n < 0)$ 
 $\mathbf{p}^{(0)} = \mathbf{G} [\mathbf{S}_{\text{pr}}]$ 
 $\hat{\mathbf{r}}^{(0)} = \mathbf{r}^{(0)} = \mathbf{G} [\mathbf{S}_{\text{cs}}^{\text{new}} [\mathbf{p}^{(0)}]]$ 
 $\rho_{sc}^{(0)} = \alpha_{sc}^{(0)} = \omega_{sc}^{(0)} = 1$ 
 $\mathbf{v}_{sc}^{(0)} = \mathbf{x}_{sc}^{(0)} = 0$ 

for  $n > 0$  do
   $\rho_{sc}^{(n)} = \langle \hat{\mathbf{r}}^{(0)}, \mathbf{r}^{(n-1)} \rangle$ 
   $\beta_{sc}^{(n)} = \frac{\alpha_{sc}^{(n-1)} \rho_{sc}^{(n)}}{\omega_{sc}^{(n-1)} \rho_{sc}^{(n-1)}}$ 
   $\mathbf{x}_{sc}^{(n)} = \mathbf{r}^{(n-1)} + \beta_{sc}^{(n)} (\mathbf{x}_{sc}^{(n-1)} - \omega_{sc}^{(n-1)} \mathbf{v}_{sc}^{(n-1)})$ 
   $\mathbf{v}_{sc}^{(n)} = \mathbf{G} [\mathbf{S}_{\text{cs}}^{\text{new}} [\mathbf{x}_{sc}^{(n)}]] - \mathbf{x}_{sc}^{(n)}$ 
   $\alpha_{sc}^{(n)} = \frac{\rho_{sc}^{(n)}}{\langle \hat{\mathbf{r}}^{(0)}, \mathbf{v}_{sc}^{(n)} \rangle}$ 
   $\mathbf{s}_{sc}^{(n)} = \mathbf{r}^{(n-1)} - \alpha_{sc}^{(n)} \mathbf{v}_{sc}^{(n)}$ 
   $\mathbf{t}_{sc}^{(n)} = \mathbf{G} [\mathbf{S}_{\text{cs}}^{\text{new}} [\mathbf{s}_{sc}^{(n)}]] - \mathbf{s}_{sc}^{(n)}$ 
   $\omega_{sc}^{(n)} = \frac{\langle \mathbf{t}_{sc}^{(n)}, \mathbf{s}_{sc}^{(n)} \rangle}{\langle \mathbf{t}_{sc}^{(n)}, \mathbf{t}_{sc}^{(n)} \rangle}$ 
   $\mathbf{p}^{(n)} = \mathbf{p}^{(n-1)} + \alpha_{sc}^{(n)} \mathbf{x}_{sc}^{(n)} + \omega_{sc}^{(n)} \mathbf{s}_{sc}^{(n)}$ 
   $\mathbf{r}^{(n)} = \mathbf{s}_{sc}^{(n)} - \omega_{sc}^{(n)} \mathbf{t}_{sc}^{(n)}$ 
end for

```

is linear in the unknown pressure field \mathbf{p} , it may be solved via the Bi-CGSTAB iterative solution presented in Algorithm 1. Here, the inner product is defined as follows,

$$\langle \mathbf{x}, \mathbf{y} \rangle = \sum_{m=1}^M x_m y_m^*, \quad (4.15)$$

where \mathbf{x} and \mathbf{y} represent two arbitrary vectors of length M and y_m^* is the complex conjugate of y_m . Given an arbitrary vector \mathbf{x} , the inner product $\langle \mathbf{x}, \mathbf{x} \rangle$ equals the square of the Euclidian norm $\|\mathbf{x}\|^2$. During each iteration step, the vector $\mathbf{p}^{(n)}$ is updated through a search correction that depends on the residual $\mathbf{r}^{(n-1)}$, which is the function that is minimized during each iteration.

4.2.2 Convergence

The numerical convergence of the Bi-CGSTAB scheme introduced in this Section can be verified by means of the residual $r^{(n)}$. When $r^{(n)}$ is decreasing towards zero for increasing n , the obtained solution is converging towards the solution of the linearized problem. To compare $r^{(n)}$ with the normalized error $\text{Err}_1^{(n)}$ defined for Neumann we make use of the normalized error $\text{Err}_2^{(n)}$:

$$\text{Err}_2^{(0)} = 1, \quad (4.16)$$

$$\text{Err}_2^{(n+1)} = \frac{\|r^{(n)}\|}{\|p^{(0)}\|}, \quad (n \geq 0). \quad (4.17)$$

When $\text{Err}_2^{(n)}$ is decreasing towards zero for increasing n , the obtained solution is converging towards the solution of the linearized problem.

4.3 Results

In Chapter 3, two different configurations are utilized to analyze the performance of the Neumann iterative solution method. In this Section, two new configurations are used to demonstrate the numerical performance of the linearized method that has been presented. First, results obtained for a plane wave propagating through nonlinear lossless homogeneous water, are presented and discussed. This is referred to as configuration 3. Second, results have been obtained for the pressure wave field generated by a linear array. In this case, different types of media have been considered. This is referred to as configuration 4. See Appendix B for a schematic diagram which summarizes the utilized configurations. The k th harmonic pressure wave field has been obtained by filtering the total pressure wave field with an 8th order Butterworth filter having a center frequency equal to kf_0 and cut-off frequencies equal to $(\pm 0.4 + k)f_0$, with f_0 the fundamental frequency. For the fundamental pressure wave field $k = 1$. Convergence has also been investigated for configurations 3 and 4.

4.3.1 Configuration 3

Here, a plane wave is considered. This plane wave is modulated by a Gaussian pulse resulting in a pressure field that, in the plain $z = 0$ mm is given by:

$$p(t) = P_0 e^{-(2t/t_w)^2} \sin(2\pi f_0 t), \quad (4.18)$$

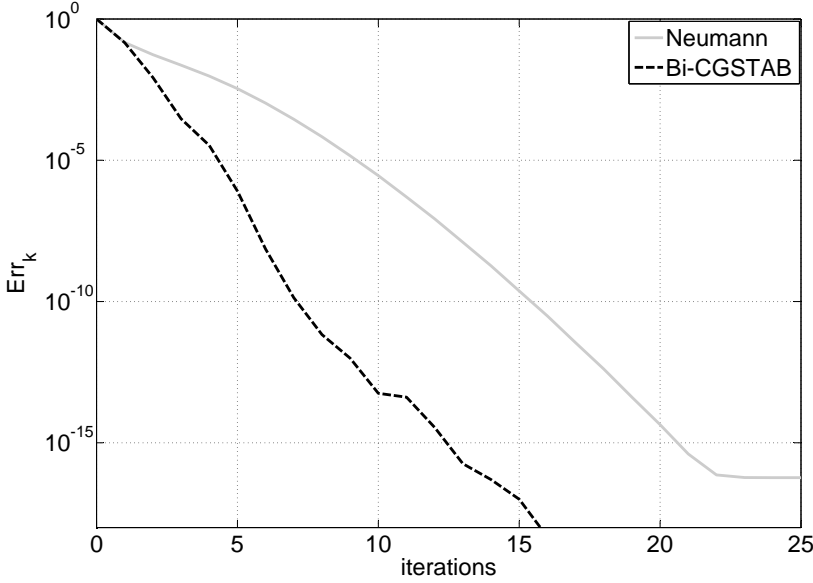


Figure 4.1: Normalized error $Err_k^{(n)}$ for configuration 3 for Neumann (gray-solid line) applied to the full nonlinear problem and Bi-CGSTAB (black-dashed line) applied to the linearized problem.

with a time width $t_w = 3/f_0$ and a center frequency $f_0 = 1$ MHz. The envelope of this signal contains about six cycles of the harmonic signal [2]. The peak pressure considered is $P_0 = 2$ MPa. The dimensions of the spatial computational domain \mathcal{D} are $(x \times y \times z) = (10 \text{ mm} \times 10 \text{ mm} \times 50 \text{ mm})$ and simulations have been performed up to the fifth harmonic component.

Convergence

Convergence of the presented Bi-CGSTAB scheme is tested for configuration 3 using the normalized error $Err_2^{(n)}$. Furthermore, $Err_2^{(n)}$ is compared with the normalized error $Err_1^{(n)}$, as obtained when the Neumann scheme described in Chapter 3 is applied to configuration 3.

Results are presented in Fig. 4.1. The graphs show that if the Neumann iterative solution method is applied, the normalized error $Err_1^{(n)} \approx 10^{-16}$ after 21 iterations, and remains flat afterwards. Therefore, if the threshold is set

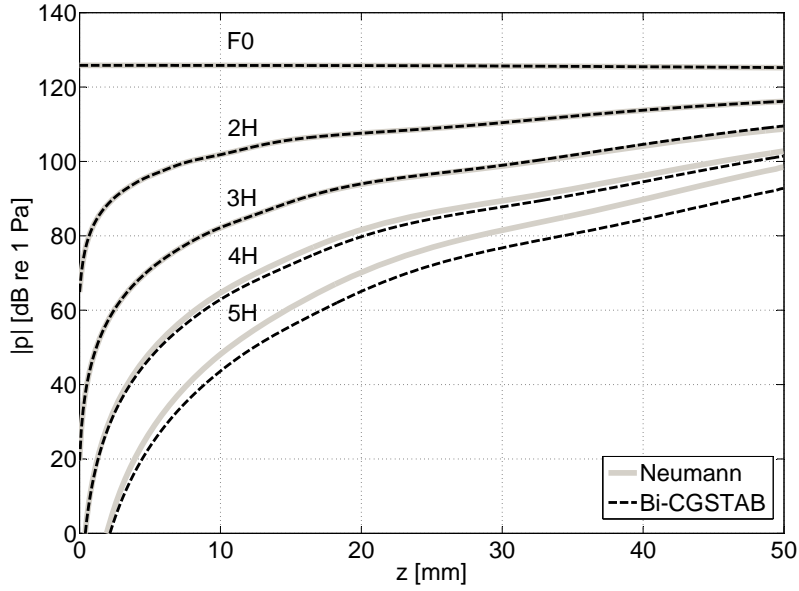


Figure 4.2: Axial profiles for the fundamental (F0), second (2H), third (3H), fourth (4H) and fifth (5H) harmonic as obtained in configuration 3 for Neumann (gray-solid line) applied to the full nonlinear problem and Bi-CGSTAB (black-dashed line) applied to the linearized problem. The pressure values are expressed in dB relative to 1 Pa.

to 10^{-16} , the Neumann iterative solution method may be stopped at iteration 22. On the other hand, in case Bi-CGSTAB is applied to solve the linearized integral equation, the normalized error $\text{Err}_2^{(n)} \approx 10^{-16}$ after 13 iterations, and hence the iterative scheme can be stopped at iteration 14. Therefore, it can be concluded that application of a Bi-CGSTAB scheme leads to a significantly faster convergence when compared to the Neumann iterative solution method described in Chapter 3. In fact, a reduction of the required number of iterations equal to 38% can be observed for the described configuration. Nevertheless, although $\text{Err}_2^{(n)}$ provides the information needed to define a stop criterion, it says nothing about the correctness of the obtained solution. In fact, while $\text{Err}_1^{(n)}$ provides information on the error with respect to the solution of the full nonlinear problem, $\text{Err}_2^{(n)}$ provides information on the error with respect to the solution of the linearized problem, and no information on the distance from the solution of the linearized and the full nonlinear problem is given.

In silico experiments

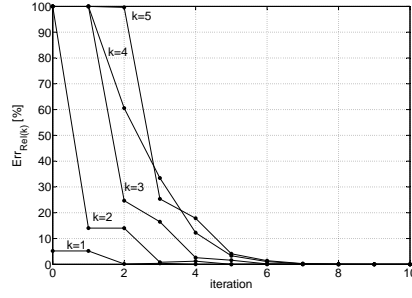
Figure 4.2 shows the axial profiles along the z -axis for the fundamental (F0), second (2H), third (3H), fourth (4H) and fifth (5H) harmonic as obtained in configuration 3 for Neumann (gray-solid line) applied to the full nonlinear problem and Bi-CGSTAB (black-dashed line) applied to the linearized problem. The pressure values are expressed in dB relative to 1 Pa. As can be seen, the solution of the linearized problem does not fully coincide with the solution of the full nonlinear problem.

To quantify the influence of the linearization and to verify whether it does, or does not depend on the iterative scheme used, the relative error

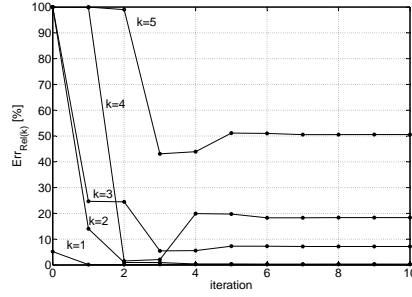
$$\text{Err}_{\text{rel}(k)}^{(n)} = 100 \times \frac{|\hat{p}^{(n)}(\mathbf{x}, kf_0) - \hat{p}^{\text{B}}(\mathbf{x}, kf_0)|}{|\hat{p}^{\text{B}}(\mathbf{x}, kf_0)|} \quad (4.19)$$

has been computed for configuration 3, when Neumann is applied either to the full nonlinear problem or to the linearized problem, and when Bi-CGSTAB is applied to the linearized problem. Here, $\hat{p}^{(n)}(\mathbf{x}, kf_0)$ and $\hat{p}^{\text{B}}(\mathbf{x}, kf_0)$ represent the pressure values in a point \mathbf{x} for the frequency kf_0 , with k an integer number and f_0 the fundamental frequency of the propagating wave field, as obtained for a given method after n iterations and a benchmark solution respectively. Here, the result obtained with the Neumann iterative solution method applied to the full nonlinear problem, as obtained at iteration 22, is used as benchmark solution. Figure 4.3 shows the relative error $\text{Err}_{\text{rel}(k)}^{(n)}$ calculated at $(x, y, z) = (0 \text{ mm}, 0 \text{ mm}, 50 \text{ mm})$, as obtained with (a) Neumann applied to the full nonlinear problem and (b) Neumann and (c) Bi-CGSTAB applied to the linearized problem. The top panel, Fig. 4.3(a), shows the behavior of the original INCS method, i.e. using the Neumann iterative solution without linearization of the contrast source. The relative error for this scheme converges to a stable value in seven iterations. Results in the center panel, Fig. 4.3(b), apply to the case where the Neumann iterative solution method is applied to the linearized problem. Also in this case, the relative error converges to a stable value in seven iterations. However, this result does not coincide with the benchmark solution. The bottom panel, Fig. 4.3(c), shows results obtained with Bi-CGSTAB applied to the linearized problem. This method converges more quickly, i.e. a stable relative error is obtained in three iterations. However, the obtained result again does not coincide with the benchmark.

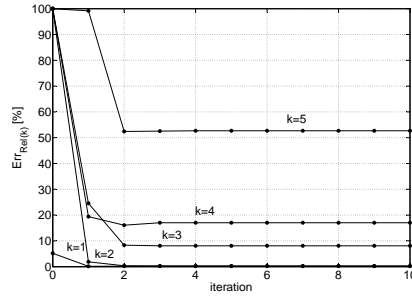
Upon comparing the different methods, four observations may be made. First, the application of the Neumann iterative solution method to the linearized prob-



(a)



(b)



(c)

Figure 4.3: Relative error $\text{Err}_{\text{rel}(k)}^{(n)}$ calculated at $(x, y, z) = (0 \text{ mm}, 0 \text{ mm}, 50 \text{ mm})$, as obtained with (a) Neumann applied to the full nonlinear problem, and (b) Neumann and (c) Bi-CGSTAB applied to the linearized problem. The solution of the full nonlinear problem obtained with Neumann at iteration 22 is used as benchmark solution.

lem seems to have only an adverse effect. In fact, when compared to the application of the Neumann iterative solution method to the full nonlinear problem, a higher relative error is obtained and the same amount of iterations is required in order to reach a stable relative error value. By contrast, when Bi-CGSTAB is applied to the linearized problem, a faster method, as compared to the application of the Neumann iterative solution methods, is obtained. Second, both schemes, when applied to the linearized problem, converge to almost the same error. Thus, linearization causes a systematic error that appears to be independent of the applied solution method. Third, linearization seems to have a noticeable effect only on the fourth and higher harmonics. Since the amplitudes of these harmonics are small with respect to the amplitude of the fundamental component, the error in these harmonics will only have a small effect on the total nonlinear wave field. Fourth, when comparing Figs. 4.1 and 4.3, it is interesting to notice that given the iterations at which each method reaches a stable relative error, the normalized errors $\text{Err}_1^{(n)}$ and $\text{Err}_2^{(n)}$ have reached basically the same value. In fact, $\text{Err}_1^{(n=7)} = 2.8 \cdot 10^{-4}$ and $\text{Err}_2^{(n=3)} = 2.9 \cdot 10^{-4}$. This seems to suggest that we can assume a threshold of 10^{-4} to be sufficient for our stop criterion.

4.3.2 Configuration 4

In this configuration a more realistic source is considered, i.e. a linear phased array. The origin of the coordinate system is located at the center of the transducer. The array consists of $N_{el} = 40$ elements. The dimensions of the elements are $W_{el} = 0.45$ mm by $H_{el} = 10$ mm, and the pitch is $D_{el} = 0.5$ mm. The elements are excited with the same pulse as used for configuration 3, except that this time the peak pressure at the surface of each transducer element is reduced to $P_0 = 1$ MPa. In addition, focusing is applied.

Configuration 4 contains lossless nonlinear water as a background medium, may contain lossy nonlinear objects, and is used for two distinct scenarios that we will refer to as scenario 4a and 4b. In scenario 4a the beam is focused at $(x, y, z) = (0 \text{ mm}, 0 \text{ mm}, 35 \text{ mm})$ and the dimensions of the spatial computational domain \mathcal{D} are $(x \times y \times z) = (30 \text{ mm} \times 20 \text{ mm} \times 50 \text{ mm})$. In scenario 4b, the beam is focused at $(x, y, z) = (35 \text{ mm}, 0 \text{ mm}, 35 \text{ mm})$, and the spatial computational domain \mathcal{D} measures $(x \times y \times z) = (24 \text{ mm} \times 12 \text{ mm} \times 40 \text{ mm})$. For this scenario only, a skew domain, having the same angles with respect to the y and z axes as the beam axis, is used [1]. Furthermore, this scenario applies only to homogeneous media.

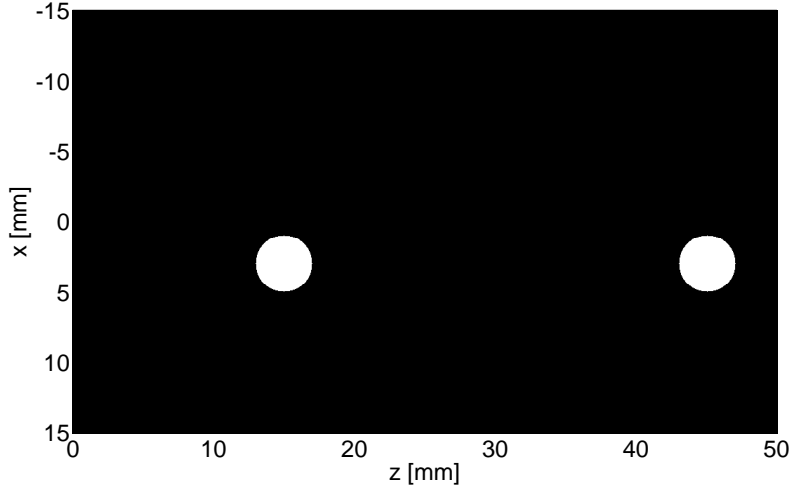


Figure 4.4: Cross-section of the spatial domain \mathcal{D} for scenario 4a containing highly-lossy nonlinear objects embedded in lossless nonlinear water along the plane $y = 0$ mm. Black indicates the lossless nonlinear background medium, white indicates the lossy nonlinear objects.

Convergence

The convergence of the linearized Bi-CGSTAB scheme is tested using the normalized error $\text{Err}_2^{(n)}$. This error has been computed for scenario 4a containing highly lossy nonlinear objects embedded in lossless nonlinear water. Simulations have been performed up to the third harmonic. The lossy nonlinear objects consist of two spherical inclusions of radius $r = 2$ mm showing a coefficient of nonlinearity, a speed of sound and a density of mass equal to water and a frequency power law attenuation with $a = 1.56 \text{ Np cm}^{-1} \text{ MHz}^{-b}$ and $b = 1.05$. These losses are 30 times those encountered in liver, and may therefore be considered extremely high in a biomedical context. A cross-section of the spatial domain \mathcal{D} along the plane $y = 0$ mm is shown in Fig. 4.4. Black indicates the lossless nonlinear background medium, white indicates the lossy nonlinear objects. The same configuration has been also utilized to calculate the normalized error $\text{Err}_1^{(n)}$, in order to compare the performance of the Neumann iterative solution method applied to the full

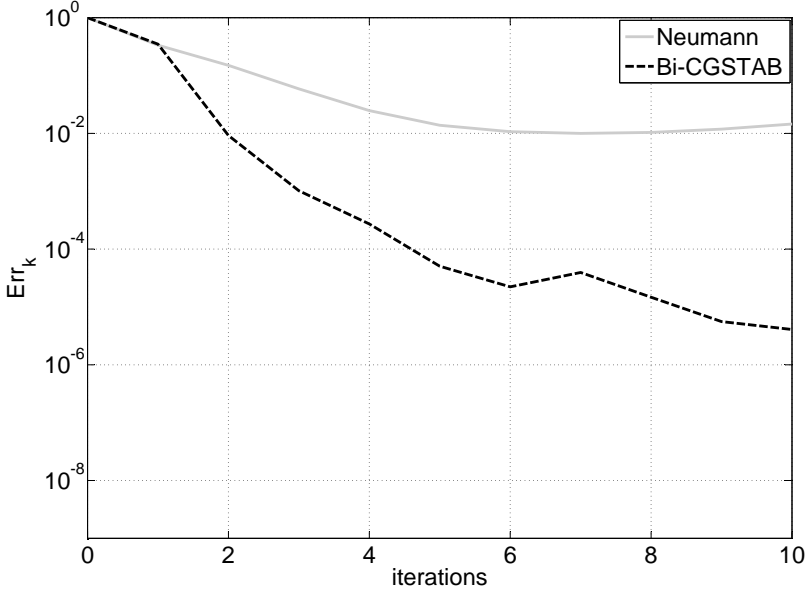
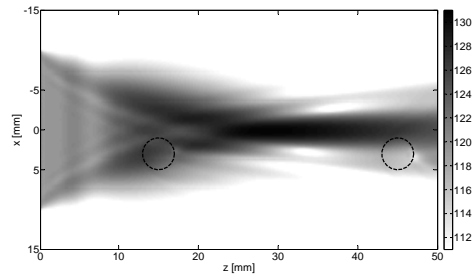


Figure 4.5: Normalized error $Err_k^{(n)}$ as obtained with Neumann (gray-solid line) applied to the full nonlinear problem and Bi-CGSTAB (black-dashed line) applied to the linearized problem for scenario 4a containing highly-lossy nonlinear objects embedded in lossless nonlinear water.

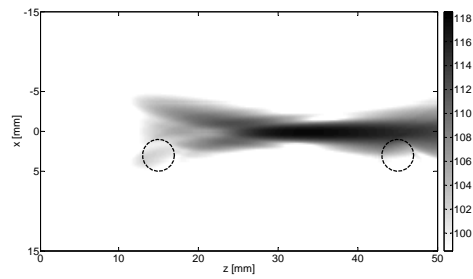
nonlinear problem with the Bi-CGSTAB iterative solution method applied to the linearized problem. Results for the two normalized errors are presented in Fig. 4.5. As can be seen, while the Neumann iterative solution method starts to manifest a divergent behavior, the Bi-CGSTAB iterative solution method allows to reach a normalized error value lower than 10^{-4} in five iterations. This observation demonstrates the usefulness of linearizing the nonlinear wave equation.

In silico experiments

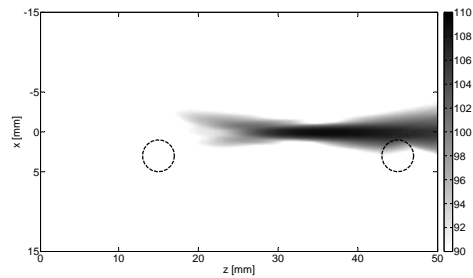
Figure 4.6 shows two-dimensional spectral profiles of the pressure wave field for the (a) fundamental, (b) second and (c) third harmonic component in the plane $y = 0$ mm, as obtained for scenario 4a with highly lossy spheres (dashed objects). The results are obtained with the Bi-CGSTAB iterative solution method applied to the linearized problem. As can be seen, the beam patterns are deformed by the lossy inclusions. Note that the deformation becomes more prominent for the



(a)

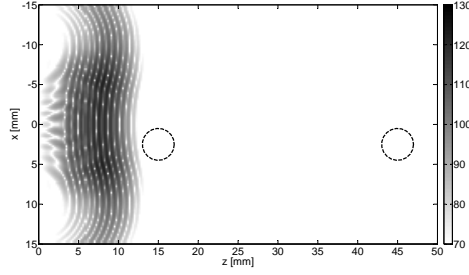


(b)

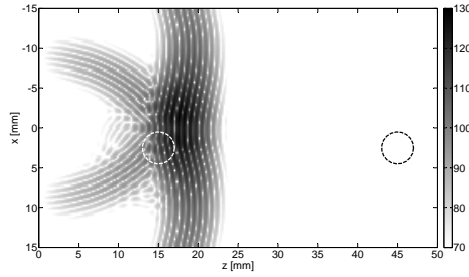


(c)

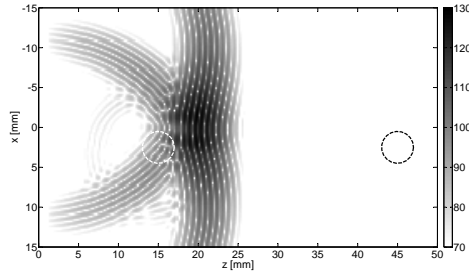
Figure 4.6: Two-dimensional spectral profiles of the pressure wave field in scenario 4a with lossless nonlinear water (background) and lossy inhomogeneities (dashed objects); (a) fundamental, (b) second harmonic, (c) third harmonic. The plane of observation is $y = 0$ mm. The pressure values are expressed in dB relative to 1 Pa.



(a)



(b)



(c)

Figure 4.7: Snapshots of the propagating pressure pulse in scenario 4a with lossless nonlinear water (background) and lossy inhomogeneities (dashed objects); (a) early time to (b-c) late time. The plane of observation is $y = 0$ mm. The pressure values are expressed in dB relative to 1 Pa.

higher harmonics. This effect may be explained by the frequency dependency of the lossy contrast, by the increasing size of the contrast with respect to decreasing wavelength, and by the nonlinearity of the phenomena which generates the higher harmonics, which causes a slight disturbance in the fundamental to become enhanced in the higher harmonics.

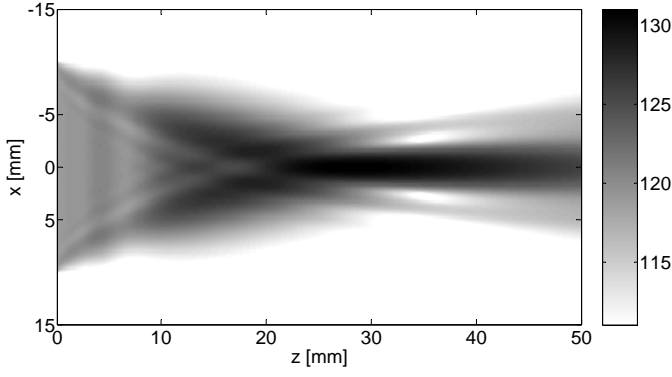
Figure 4.7 shows several snapshots of the total nonlinear wave field in the plane $y = 0$ mm. The snapshot at the top shows the wave field just after its transmission by the transducer. The other two snapshots show the reflection from the left inclusion.

Figures 4.8 to 4.12 show the two-dimensional spectral profiles and the relative errors in the plane $y = 0$ mm, up to the fifth harmonic component, as obtained in scenario 4a when no lossy nonlinear objects are present. For these plots, the relative error is defined as

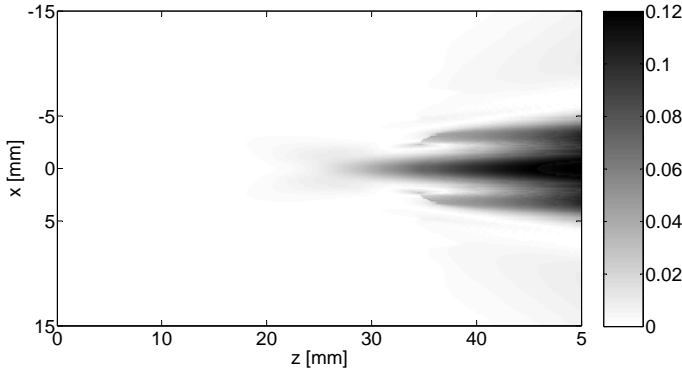
$$\text{Err}_{\text{rel}}(\mathbf{x}) = 100 \times \frac{|\max_t [p_k(\mathbf{x}, t)] - \max_t [p_k^{\text{B}}(\mathbf{x}, t)]|}{|\max_t [p_k^{\text{B}}(\mathbf{x}, t)]|}. \quad (4.20)$$

These results are obtained by the Neumann iterative solution method applied to the linearized problem. The figures clearly show the typical features of the higher harmonic beam patterns that are generated during nonlinear propagation, such as the decrease of the focal width and the shift of the onset of the beams. Here, $p_k(\mathbf{x}, t)$ is the k th harmonic pressure wave field obtained with the described linearized method as obtained at iteration seven ($\text{Err}_1^{(n=7)} = 2.1 \cdot 10^{-4}$). The error is determined with respect to $p_k^{\text{B}}(\mathbf{x}, t)$, which is the k -th harmonic pressure wave field as obtained with the Neumann iterative solution method applied to the full nonlinear problem at iteration seven ($\text{Err}_1^{(n=7)} = 2.3 \cdot 10^{-4}$). Similar to the observation made for configuration 3, it is observed that the errors increase for increasingly higher harmonics and that accurate results are obtained up till the third harmonic.

Figure 4.13 shows the beam profiles, up to the fifth harmonic, along the beam axis and along the line $(y, z) = (0 \text{ mm}, 35 \text{ mm})$, as obtained in scenario 4b. The results, obtained with the Neumann iterative solution method applied to the full nonlinear problem (solid-gray line) and to the linearized problem (dashed-black line), are in full correspondence with the results previously shown. In fact, both methods yield identical results for the fundamental up to the third harmonic component, while results obtained with the Neumann iterative solution method

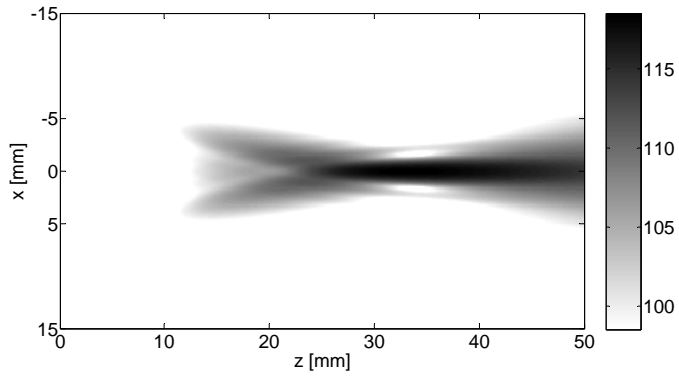


(a)

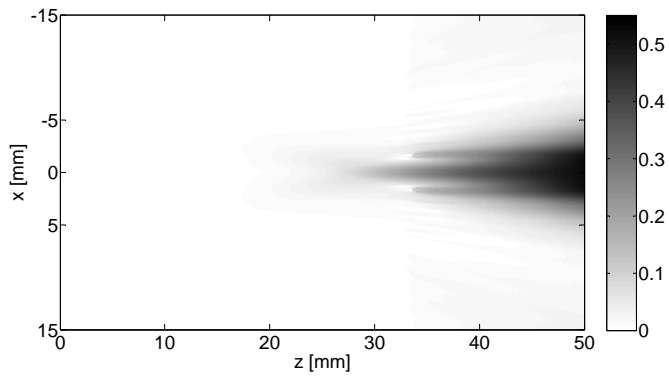


(b)

Figure 4.8: Two-dimensional (a) spectral profiles and (b) relative error for the fundamental pressure wave field in scenario 4a without lossy nonlinear objects. The plane of observation is $y = 0$ mm. The pressure values are expressed in dB relative to 1 Pa.

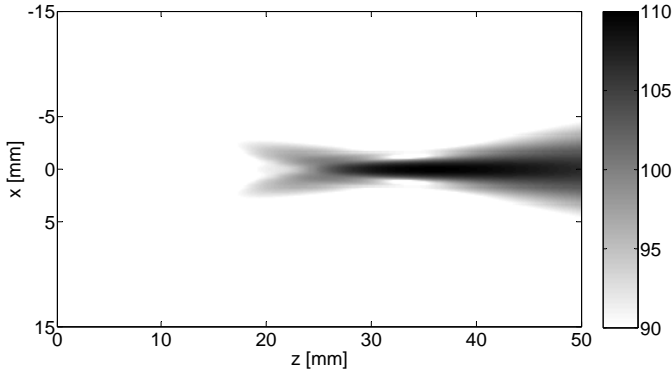


(a)

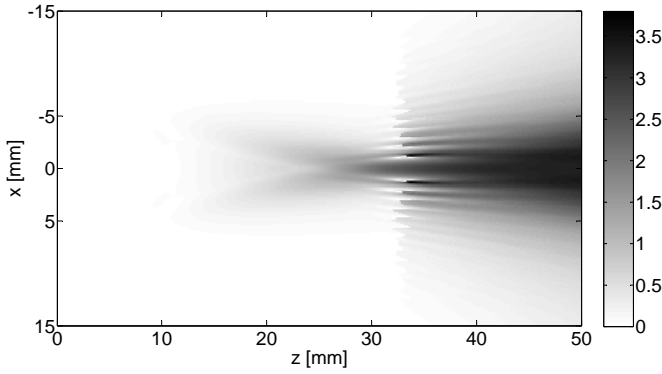


(b)

Figure 4.9: Two-dimensional (a) spectral profiles and (b) relative error for the second harmonic pressure wave field in scenario 4a without lossy nonlinear objects. The plane of observation is $y = 0$ mm. The pressure values are expressed in dB relative to 1 Pa.

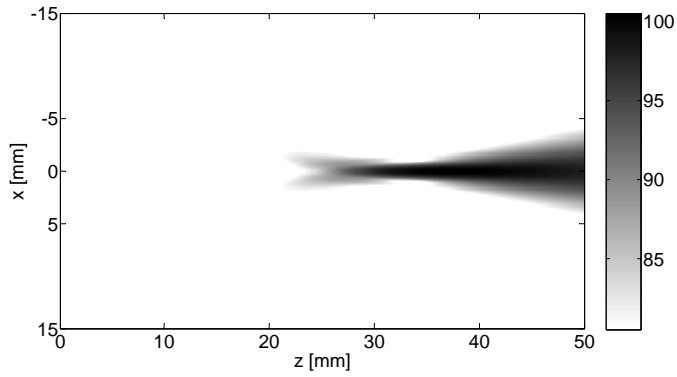


(a)

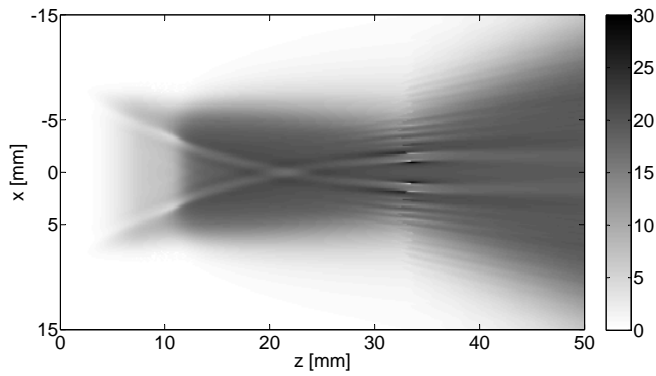


(b)

Figure 4.10: Two-dimensional (a) spectral profiles and (b) relative error for the third harmonic pressure wave field in scenario 4a without lossy nonlinear objects. The plane of observation is $y = 0$ mm. The pressure values are expressed in dB relative to 1 Pa.

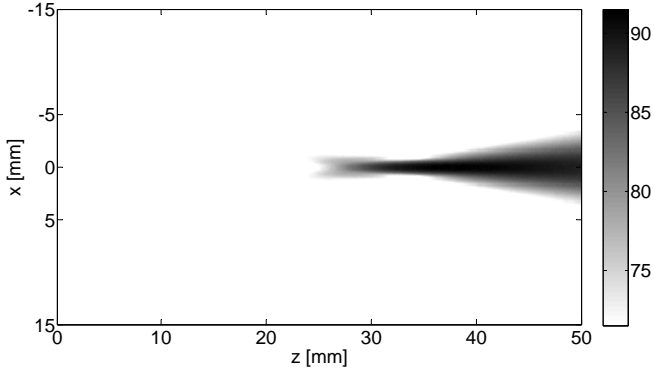


(a)

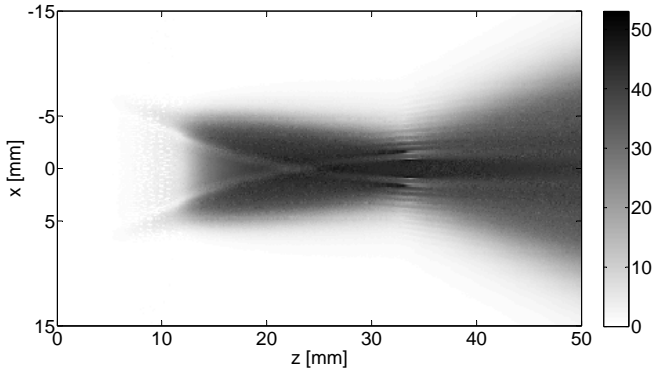


(b)

Figure 4.11: Two-dimensional (a) spectral profiles and (b) relative error for the fourth harmonic pressure wave field in scenario 4a without lossy nonlinear objects. The plane of observation is $y = 0$ mm. The pressure values are expressed in dB relative to 1 Pa.



(a)



(b)

Figure 4.12: Two-dimensional (a) spectral profiles and (b) relative error for the fifth harmonic pressure wave field in scenario 4a without lossy nonlinear objects. The plane of observation is $y = 0$ mm. The pressure values are expressed in dB relative to 1 Pa.

applied to the linearization problem shown an underestimation of the fourth and fifth harmonic component when compared to results obtained with the Neumann iterative solution method applied to the full nonlinear problem. Moreover, they show that linearization works equally well for a steered and an unsteered beam.

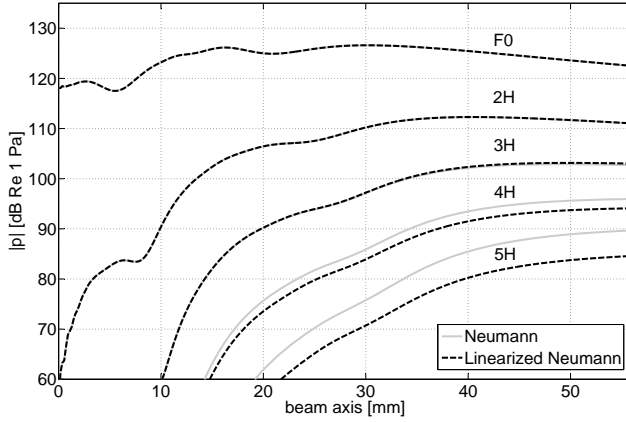
4.4 Conclusions

In this Chapter, a method that makes use of a Bi-CGSTAB scheme to model nonlinear wave fields propagation through inhomogeneous biomedical media has been presented. This solution method has become applicable after linearization of the nonlinear wave equation. Only inhomogeneities in the attenuation have been considered in this Chapter.

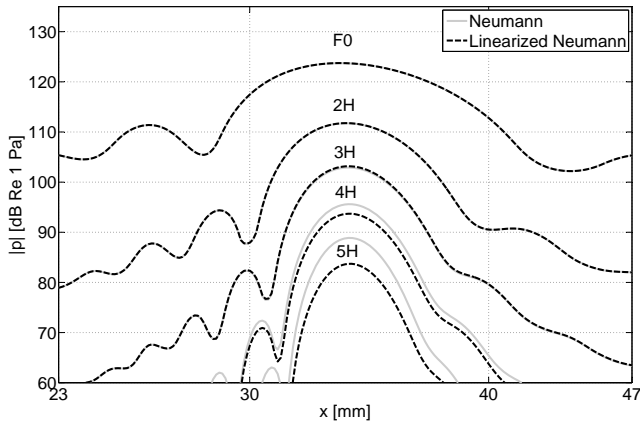
First, the convergence of the solution method has been investigated. Numerical results show convergence towards the solution of the linearized problem. In addition, it is shown how the contrast, and the scheme applied, determine the convergence rate of the method. Moreover, application of a Bi-CGTAB scheme results in a faster convergence when compared to the application of a Neumann scheme. Furthermore, it has been shown that Bi-CGSTAB allows to handle stronger contrasts than Neumann.

Second, the capability of the method to model nonlinear pressure wave fields propagating through media presenting spatially inhomogeneous frequency dependent attenuation has been demonstrated. In silico experiments show the capability of the method to deal with scattering and that the linearization does not influence the full wave character of the method.

In conclusion, Bi-CGSTAB represents a suitable scheme that allows to deal with a broader variety of contrasts than Neumann. Nevertheless, it comes with the cost of an approximation that influences the obtained results. The linearization introduces a systematic error that can be considered independent of the applied scheme and that is relevant for the harmonics of the fourth order or higher. Furthermore, it should be noted that the Bi-CGSTAB scheme, when compared to the Neumann scheme, requires a higher computational cost, i.e. two spatio-temporal convolutions are required per iteration, and results in an increased complexity, i.e. more vectors need to be computed and stored. Moreover, it is known that Bi-CGSTAB may not converge in case of increasingly stronger



(a)



(b)

Figure 4.13: The nonlinear pressure field in scenario 4b as obtained with the Neumann iterative solution method applied to the full nonlinear problem (solid-gray line) and to the linearized problem (dashed-black line); (a) axial profile evaluated along the transducer axis, (b) lateral profile evaluated along the line $(y, z) = (0 \text{ mm}, 35 \text{ mm})$. The graphs show the fundamental (F0), second (2H), third (3H), fourth (4H) and fifth harmonic (5H) component.

contrast. Therefore, to extend the method to deal with a broader variety of contrasts, e.g. realistic inhomogeneities in the speed of sound, and be capable at the same time to model high harmonics (higher than the third order), an alternative scheme has to be investigated. In the next Chapter a Steepest Descent based approach is proposed and discussed.

Steepest Descent scheme

The nonlinear propagation of acoustic wave fields through inhomogeneous media can be modeled using an integral equation formulation. In Chapter 3, it has been shown that this integral equation may be solved with a Neumann solution method in case weak contrasts are present, i.e. when only variations in the coefficient of nonlinearity, or small variations in the attenuation, are considered. In case of stronger contrasts, Neumann can be slowly convergent or even diverge. A way to overcome this limitation is to linearize the nonlinear wave equation that models the propagation of the nonlinear pressure wave field, and make use of a Bi-CGSTAB scheme to solve the resulting linearized problem. However, this approach seems only to be suitable for simulations up to the third harmonic, as the linearization brings along a systematic error which becomes relevant for the harmonics of the fourth order or higher.

In this Chapter, an alternative approach based on a Steepest Descent scheme is presented. Results will show how this scheme allows for modeling the full nonlinear problem in presence of stronger contrasts as compared to both the Neumann and Bi-CGSTAB iterative solution methods described in Chapter 3 and 4 respectively. As a drawback, it results in an increased complexity and computational cost per iteration. First the solution method is introduced. Second, results obtained via application of this method are presented, discussed and compared with results obtained via Neumann and Bi-CGSTAB scheme.

Algorithm 2 The Steepest Descent solution method

for $n \geq 0$ **do**

$$r^{(n)} = p^{(0)} - p^{(n)} + G *_{\mathbf{x},t} S_{\text{cs}} [p^{(n)}]$$

$$d^{(n)} = -\frac{\Delta m^T}{c^2} *_t \left\{ \partial_t^2 [G^T *_{\mathbf{x},t} r^{(n)}] \right\} - \frac{m_{bg}^T}{c^2} *_t \left\{ \frac{c_{bg}^2 - c^2}{c_{bg}^2} \partial_t^2 [G^T *_{\mathbf{x},t} r^{(n)}] \right\} \\ + 2\rho_{bg}\kappa^2 \beta p^{(n)} \partial_t^2 [G^T *_{\mathbf{x},t} r^{(n)}] - r^{(n)}$$

$$\alpha_{sd}^{(n)} = s_1 + s_2 - \frac{\phi_3}{4}$$

$$p^{(n+1)} = p^{(n)} + \alpha_{sd}^{(n)} d^{(n)}$$

end for

with

$$p^{(n)} = 0 \text{ for } (n < 0)$$

$$p^{(0)} = G *_{\mathbf{x},t} S_{\text{pr}}$$

$$s_1 = \sqrt[3]{z - \sqrt{u^3 + z^2}}$$

$$s_2 = \sqrt[3]{z + \sqrt{u^3 + z^2}}$$

$$u = \frac{\phi_2}{6} - \frac{\phi_3^2}{16}$$

$$z = \frac{\phi_2 \phi_3}{16} - \frac{\phi_1}{8} - \frac{\phi_3^3}{64}$$

$$\phi_1 = \frac{2\Re\langle r^{(n)}, \theta_1 \rangle}{\|\theta_2\|^2}$$

$$\phi_2 = \frac{2\Re\langle r^{(n)}, \theta_2 \rangle + \|\theta_1\|^2}{\|\theta_2\|^2}$$

$$\phi_3 = \frac{2\Re\langle \theta_1, \theta_2 \rangle}{\|\theta_2\|^2}$$

$$\theta_1 = -d^{(n)} + G *_{\mathbf{x},t} \left\{ S_{\text{at}} [d^{(n)}] + S_c [d^{(n)}] + 2\rho_{bg}\kappa^2 \beta \partial_t^2 [p^{(n)} d^{(n)}] \right\}$$

$$\theta_2 = G *_{\mathbf{x},t} S_{\text{nl}} [d^{(n)}]$$

5.1 Solution method

In this section, a Steepest Descent based solution method, applied to solve the full nonlinear problem described by the integral equation introduced in Chapter 2, given by

$$p(\mathbf{x}, t) = p^{(0)}(\mathbf{x}, t) + \int_{\mathcal{T}} \int_{\mathcal{D}} G(\mathbf{x} - \mathbf{x}', t - t') S_{\text{cs}}[p(\mathbf{x}', t')] d\mathbf{x}' dt', \quad (5.1)$$

is presented and discussed.

5.1.1 Steepest Descent scheme

The Steepest Descent scheme described in Algorithm 2 is applied to solve Eq. (5.1). The method is based on the ideas presented in [58], where an iterative inversion method with total variation as multiplicative regularization is used for imaging purposes. This regularization factor leads to a fourth order cost functional in the same way as our nonlinear contrast source does. Taking advantage of these similarities, the same scheme is used where the update directions $d^{(n)}$ are obtained by taking Fréchet derivatives

$$\langle d^{(n)}, d^{(n)} \rangle = \lim_{\epsilon \rightarrow 0} \frac{F[p^{(n)} + \epsilon d^{(n)}] - F[p^{(n)}]}{\epsilon}, \quad (5.2)$$

with ϵ real valued, and update amplitudes are obtained by finding the minimum of the fourth order cost polynomial (for given update direction) analytically,

$$\partial_{\alpha_{sd}^{(n)}} F[p^{(n)} + \alpha_{sd}^{(n)} d^{(n)}] = 0, \quad (5.3)$$

with cost functional

$$\begin{aligned} F[p^{(n)}] &= \langle p^{(0)} - p^{(n)} + G *_{\mathbf{x},t} S_{cs}[p^{(n)}], p^{(0)} - p^{(n)} + G *_{\mathbf{x},t} S_{cs}[p^{(n)}] \rangle \\ &= \langle r^{(n)}, r^{(n)} \rangle. \end{aligned} \quad (5.4)$$

In Algorithm 2, $\|\cdot\|$ and $\langle \cdot, \cdot \rangle$ represent the Euclidean norm and the inner product respectively. Here, the inner product is defined as follows,

$$\langle \mathbf{x}, \mathbf{y} \rangle = \sum_{m=1}^M x_m y_m^*, \quad (5.5)$$

where \mathbf{x} and \mathbf{y} represent two arbitrary vectors of length M and y_m^* is the complex conjugate of y_m . Given an arbitrary vector \mathbf{x} , the inner product $\langle \mathbf{x}, \mathbf{x} \rangle$ equals the square of the Euclidian norm $\|\mathbf{x}\|^2$. In Algorithm 2, $r^{(n)}$ represents the residual, and $d^{(n)}$ and $\alpha_{sd}^{(n)}$ are the update direction and amplitudes respectively. For each iteration, $d^{(n)}$ and $\alpha_{sd}^{(n)}$ are utilized to compute the updated solution $p^{(n+1)}$. Δm^T and m_{bg}^T equal $\Delta m(\mathbf{x}, -t)$ and $m_{bg}(-t)$ respectively, G^T equals $G(-\mathbf{x}, -t)$ and $p^{(0)}$ represents the linear incident field, which corresponds to the pressure wave field generated by the primary source $S_{pr}(\mathbf{x}, t)$.

In case the nonlinear contrast sources, i.e. $S_{nl}[p(\mathbf{x}, t)]$ and $S_{nl\kappa}[p(\mathbf{x}, t)]$, equal zero, the scheme presented in Algorithm 2 has to be modified as the order of the

cost polynomial reduces to two. In particular, $\alpha_{sd}^{(n)}$ has to be modified as follows,

$$\alpha_{sd}^{(n)} = -\phi_1, \quad (5.6)$$

with

$$\phi_1 = \frac{\Re < r^{(n)}, \theta_1 >}{||\theta_1||^2}, \quad (5.7)$$

$$\theta_1 = -d^{(n)} + G *_{\mathbf{x},t} \left\{ S_{\text{at}} \left[d^{(n)} \right] + S_c \left[d^{(n)} \right] \right\}. \quad (5.8)$$

Note that for the numerical implementation of the scheme all quantities have been discretized and integrals have been replaced by summations.

5.1.2 Convergence

The numerical convergence of the presented Steepest Descent scheme is verified by means of the residual $r^{(n)}$.

To compare $r^{(n)}$ with the normalized errors $\text{Err}_1^{(n)}$ and $\text{Err}_2^{(n)}$, defined for the Neumann and Bi-CGSTAB solution method respectively, we make use of a third normalized error $\text{Err}_3^{(n)}$, which equals

$$\text{Err}_3^{(0)} = 1, \quad (5.9)$$

$$\text{Err}_3^{(n+1)} = \frac{||r^{(n)}||}{||p^{(0)}||}, (n \geq 0). \quad (5.10)$$

Here, $r^{(n)}$ and $p^{(0)}$ represent the discretized version of $r^{(n)}$ and $p^{(0)}$ respectively. When $\text{Err}_3^{(n)}$ is decreasing towards zero for increasing n , the obtained solution is converging towards the solution of the contrast source problem.

5.2 Results

In this section, two configurations are used to demonstrate the numerical performance of the method presented. First, we make use of the already introduced configuration 3. This configuration is used to compare results obtained with the three different schemes discussed in this thesis, when modeling a plane wave propagating through nonlinear lossless homogeneous water. Second, results as obtained for a plane wave propagating through different types of inhomogeneous

media are obtained. These results will show the capability of the Steepest Descent based method to model inhomogeneities in the speed of sound alone as well as inhomogeneities in all the acoustical medium parameters discussed, i.e. coefficient of nonlinearity, attenuation and speed of sound. This is referred to as configuration 5. See Appendix B for a schematic diagram which summarizes the utilized configurations. The k th harmonic pressure wave field has been obtained by filtering the total pressure wave field with an 8th order Butterworth filter having a center frequency equal to $k f_0$ and cut-off frequencies equal to $(\pm 0.4 + k) f_0$, with f_0 the fundamental frequency. For the fundamental pressure wave field $k = 1$. Convergence of the Steepest Descent method has been investigated for configurations 3 and 5.

5.2.1 Configuration 3

Here, a plane wave is considered. This plane wave is modulated by a Gaussian pulse resulting in a pressure field which, in the plane $z = 0$ mm, equals

$$p(t) = P_0 e^{-(2t/t_w)^2} \sin(2\pi f_0 t), \quad (5.11)$$

with a time width $t_w = 3/f_0$ and a center frequency $f_0 = 1$ MHz. The envelope of this signal contains about six cycles of the harmonic signal [2]. The peak pressure considered is $P_0 = 2$ MPa. The dimensions of the spatial computational domain \mathcal{D} are $(x \times y \times z) = (10 \text{ mm} \times 10 \text{ mm} \times 50 \text{ mm})$ and simulations have been performed up to the fifth harmonic component.

Convergence

The convergence of the presented Steepest Descent based method is tested for configuration 3 using the normalized error $\text{Err}_3^{(n)}$. Furthermore, the normalized error $\text{Err}_3^{(n)}$ has been compared with the normalized errors $\text{Err}_1^{(n)}$ and $\text{Err}_2^{(n)}$, as obtained via application of the previously described Neumann solution method, when applied to the full nonlinear problem, and Bi-CGSTAB solution method applied to the linearized problem.

Fig. 5.1 presents all three normalized errors. The graph shows that the normalized error for the Steepest Descent based method $\text{Err}_3^{(n)} \approx 10^{-16}$ after 21 iterations and remains flat afterwards. Therefore, in case Steepest Descent is applied to solve the full nonlinear problem and the threshold is set to 10^{-16} , the iterative process can be stopped at iteration 22. The same observation is valid for

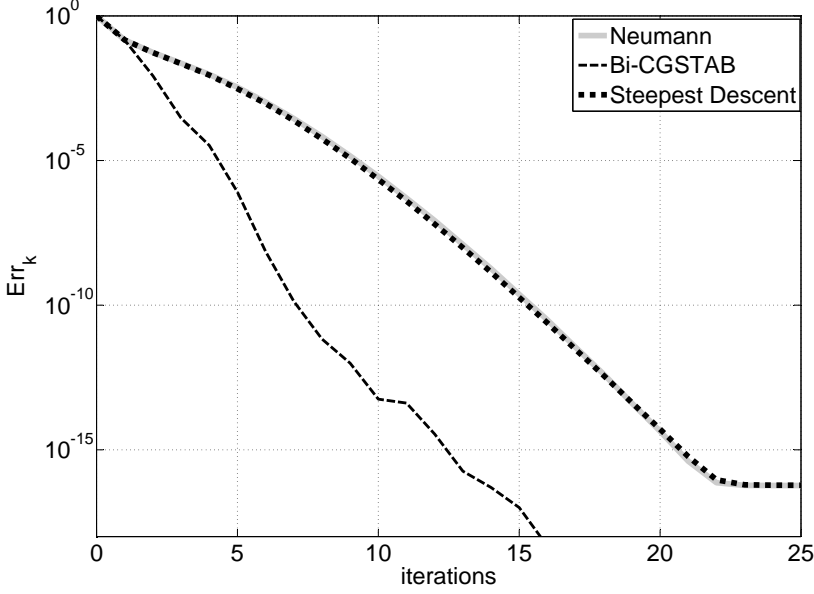


Figure 5.1: Normalized error $\text{Err}_k^{(n)}$ as obtained in configuration 3 with Neumann (gray-solid line) applied to the full nonlinear problem, Bi-CGSTAB (black-dashed line) applied to the linearized problem and Steepest Descent (black-dotted line) applied to the full nonlinear problem.

$\text{Err}_1^{(n)}$, hence in case the Neumann solution method described in Chapter 3 is applied to configuration 3. On the other hand, as already observed in Chapter 4, in case Bi-CGSTAB is applied to solve the linearized problem, $\text{Err}_2^{(n)} \approx 10^{-16}$ after 13 iterations, i.e. the iterative scheme can be stopped at iteration 14. Therefore, it can be concluded that application of a Bi-CGSTAB scheme results in a significantly faster convergence, i.e. a reduction of the required number of iterations equal to 38 % for the described configuration, with respect to both the other described schemes. Nevertheless, it comes with the price of an approximation introduced by the linearization of the integral equation. This is not the case for Steepest Descent, as it can be applied to the full nonlinear problem.

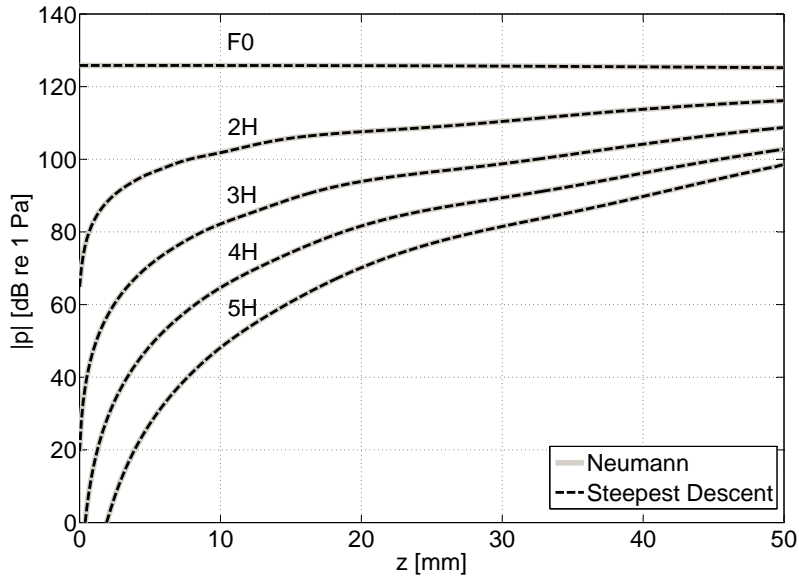


Figure 5.2: Axial profiles for the fundamental (F0), second (2H), third (3H), fourth (4H) and fifth (5H) harmonic as obtained in configuration 3 with Neumann (gray-solid line) and Steepest Descent (black-dashed line) applied to the full nonlinear problem. The pressure values are expressed in dB relative to 1 Pa.

In silico experiments

Figure 5.2 shows the axial profiles along the z axis for the fundamental (F0), second (2H), third (3H), fourth (4H) and fifth (5H) harmonic as obtained in configuration 3 for Neumann (gray-solid line) and Steepest Descent (black-dashed line) applied to the full nonlinear problem. The pressure values are expressed in dB relative to 1 Pa. As can be seen, results obtained via Steepest Descent provide a solution that does coincide with the solution as obtained with Neumann when applied to the full nonlinear problem.

5.2.2 Configuration 5

Here, the same plane wave utilized in configuration 3 is considered. Configuration 5 contains lossless linear water as a background medium and is applied to two distinct scenarios that we will refer to as scenario 5a and 5b. In scenario 5a, a

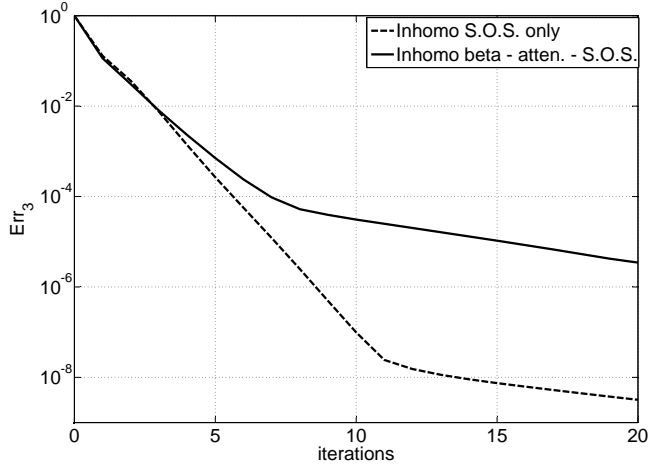
sphere with a radius equal to 4.5 mm centered at $(x, y, z) = (0 \text{ mm}, 0 \text{ mm}, 0 \text{ mm})$ is considered. This scenario is used to model inhomogeneities in the speed of sound only. For this configuration, linear lossless breast tissue is used ($c = 1510 \text{ m/s}$) as contrast [6]. In scenario 5b, a sphere with a radius equal to 4.5 mm centered at $(x, y, z) = (0 \text{ mm}, 0 \text{ mm}, 10 \text{ mm})$ is considered. This scenario is used to model inhomogeneities in the coefficient of nonlinearity, in the attenuation and in the speed of sound. Also for this configuration, breast tissue has been used as contrast ($\beta = 5.815$, $a = 0.066 \text{ Np cm}^{-1} \text{ MHz}^{-b}$, $b = 1.5$, $c = 1510 \text{ m/s}$) [6]. In configuration 5, the spatial computational domain \mathcal{D} measures $(x \times y \times z) = (20 \text{ mm} \times 20 \text{ mm} \times 20 \text{ mm})$ and simulations have been performed up to the fifth harmonic component. In the results presented for this configuration, the second order compressibility contrast $S_{\text{nl}\kappa}[p(\mathbf{x}, t)]$ has been neglected as it did not show any significant effect on the numerical results.

Convergence

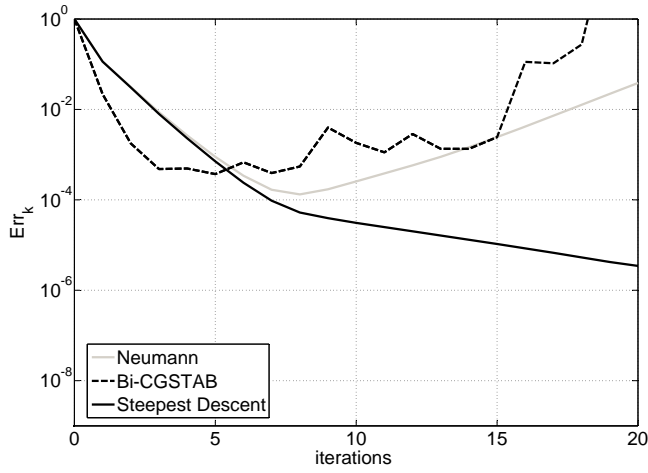
Convergence of the presented Steepest Descent based method is tested for configuration 5 using the normalized error $\text{Err}_3^{(n)}$. Results are presented in Fig. 5.3. Figure 5.3(a) shows the normalized error $\text{Err}_3^{(n)}$ obtained with the Steepest Descent solution method in scenario 5a (black-dashed line) and 5b (black-solid line). The obtained results confirm that a stronger contrast requires more iterations to reach a given normalized error value. In this specific case, when considering the contrast in speed of sound only (black-dashed line) the convergence is faster than in the situation in which we model inhomogeneities in the coefficient of nonlinearity, in the attenuation and in the speed of sound (black-solid line). Figure 5.3(b) compares the normalized errors $\text{Err}_1^{(n)}$, $\text{Err}_2^{(n)}$ and $\text{Err}_3^{(n)}$, as obtained in scenario 5b with Neumann applied to the full nonlinear problem (solid-gray line), Bi-CGSTAB applied to the linearized problem (dotted-black line) and Steepest Descent applied to the full nonlinear problem (solid-black line). This plot shows the capability of the Steepest Descent method to handle stronger contrasts than Neumann and Bi-CGSTAB.

In silico experiments

Figure 5.4 shows snapshots of the propagating pressure wave field in scenario 5a. Results as obtained with the Steepest Descent based solution method presented (left column) are compared with results obtained with the analytical solution (right column) [59]. The plane of observation is $y = 0 \text{ mm}$. The pressure values are expressed in dB relative to 1 Pa. Scattering phenomena are clearly observable



(a)



(b)

Figure 5.3: (a) Normalized error $\text{Err}_3^{(n)}$ as obtained with the Steepest Descent solution method in scenario 5a (black-dashed line) and 5b (black-solid line), and (b) normalized errors $\text{Err}_1^{(n)}$, $\text{Err}_2^{(n)}$ and $\text{Err}_3^{(n)}$ as obtained in scenario 5b with Neumann applied to the full nonlinear problem (solid-gray line), Bi-CGSTAB applied to the linearized problem (dotted-black line) and Steepest Descent applied to the full nonlinear problem (solid-black line).

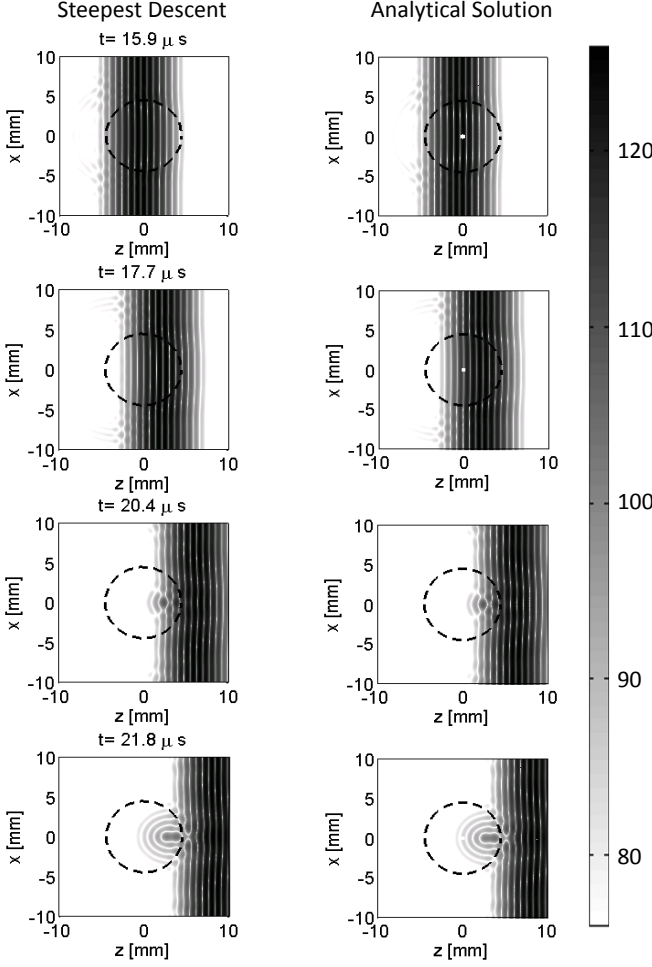


Figure 5.4: Snapshots of the propagating pressure wave field in scenario 5a with lossless linear water as background medium and a spherical object modeling inhomogeneities in the speed of sound only; results as obtained with the Steepest Descent based solution method presented (left column) are compared with results obtained with the analytical solution (right column). The plane of observation is $y = 0$ mm. The pressure values are expressed in dB relative to 1 Pa.

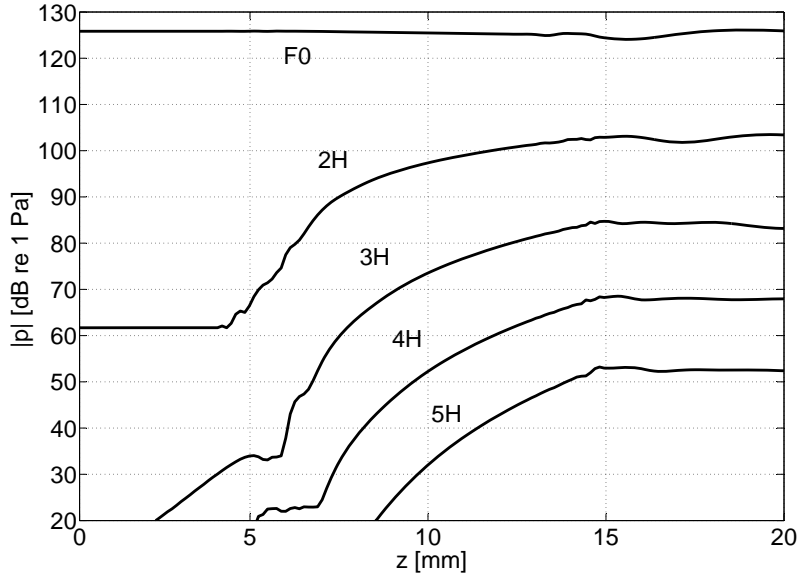
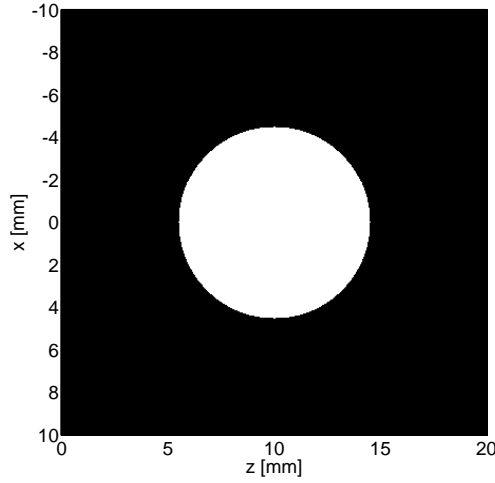


Figure 5.5: Axial profiles for the fundamental (F0), second (2H), third (3H), fourth (4H) and fifth (5H) harmonic as obtained in scenario 5b with the Steepest Descent solution method. The axis of observation is the z -axis. The pressure values are expressed in dB relative to 1 Pa.

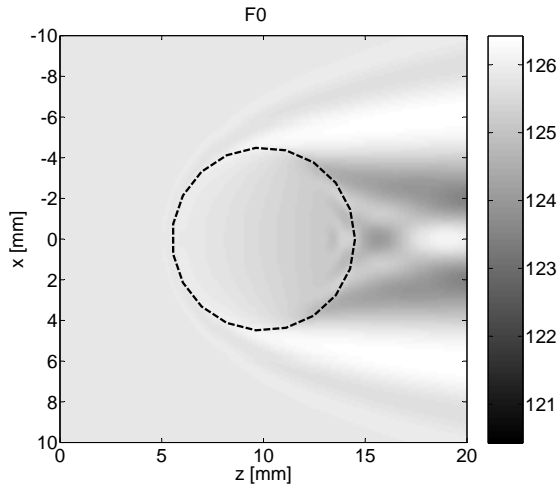
and results obtained from the analytical solution are in agreement with those obtained with the Steepest Descent solution method presented in this Chapter.

Figure 5.5 shows axial profiles for the fundamental (F0), second (2H), third (3H), fourth (4H) and fifth (5H) harmonic as obtained in scenario 5b with the application of the Steepest Descent solution method presented in this Chapter. The axis of observation is the z -axis. The pressure values are expressed in dB relative to 1 Pa.

Figures 5.6 - 5.8 show the two dimensional spectral profiles, for each harmonic component, together with a cross-section of the spatial domain \mathcal{D} along the plane $y = 0$ mm in scenario 5b. Black indicates the lossless linear background medium, white indicates the lossy nonlinear object. Note that the colorbar for the fundamental spectral profile goes from the maximum relative value to -6 dB, in order

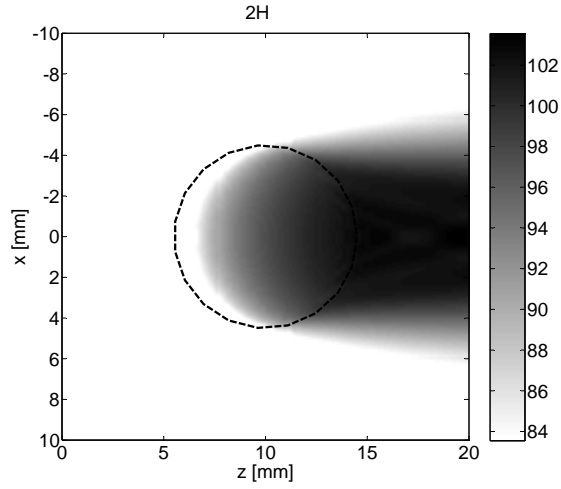


(a)

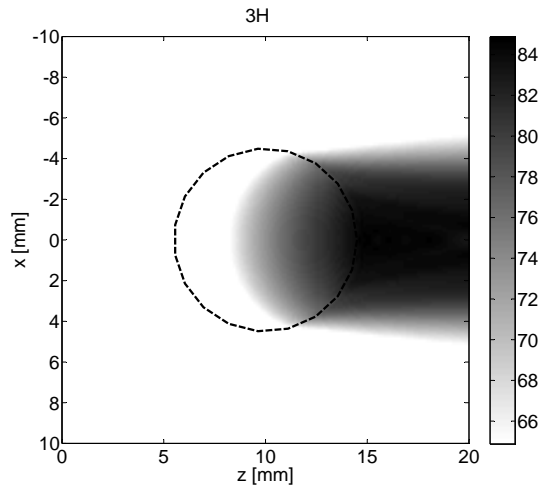


(b)

Figure 5.6: (a) Cross-section of the spatial domain \mathcal{D} for scenario 5b along the plane $y = 0$ mm. Black indicates the lossless linear background medium, white indicates the lossy nonlinear object. (b) Two-dimensional spectral profile of the fundamental component of the pressure wave field in scenario 5b with lossless linear water (background) and lossy nonlinear inhomogeneities (dashed object). The plane of observation is $y = 0$ mm. The pressure values are expressed in dB relative to 1 Pa.

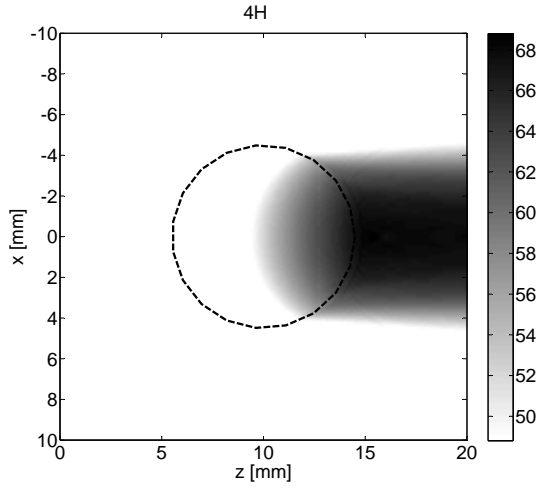


(a)

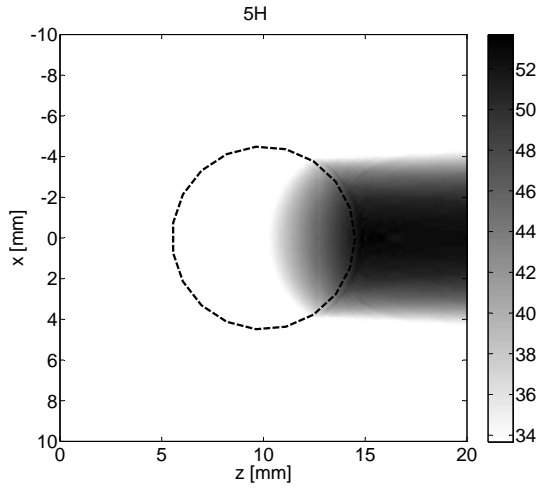


(b)

Figure 5.7: Two-dimensional spectral profiles of the (a) second and (b) third harmonic component of the pressure wave field in scenario 5b with lossless linear water (background) and lossy nonlinear inhomogeneities (dashed object). The plane of observation is $y = 0$ mm. The pressure values are expressed in dB relative to 1 Pa.



(a)



(b)

Figure 5.8: Two-dimensional spectral profiles of the (a) fourth and (b) fifth harmonic component of the pressure wave field in scenario 5b with lossless linear water (background) and lossy nonlinear inhomogeneities (dashed object). The plane of observation is $y = 0$ mm. The pressure values are expressed in dB relative to 1 Pa.

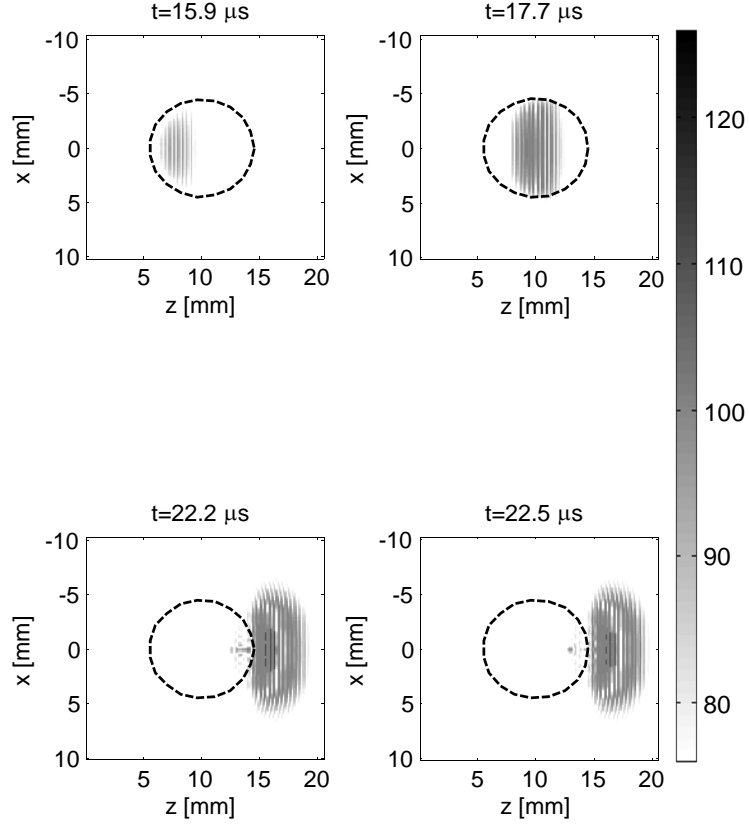


Figure 5.9: Snapshots of the second harmonic component of the propagating pressure wave field in scenario 5b with lossless linear water as background medium and lossy nonlinear object. The plane of observation is $y = 0$ mm. The pressure values are expressed in dB relative to 1 Pa.

to be able to emphasize its decay in space. The colorbars for the harmonic components go from the maximum relative values to -20 dB. As can be seen, the amplitude of the incident plane wave decays as soon as it enters the nonlinear

object. Moreover, harmonics emerge only inside this part of the simulated domain and they keep propagating afterwards. Furthermore, the cumulative nature of nonlinear propagation can be observed in these figures; the growth of the harmonic components begins sooner for the lower harmonics and keeps increasing along the path where the pressure field propagates nonlinearly.

Figure 5.9 shows snapshots of the second harmonic component of the propagating pressure wave field in scenario 5b. The plane of observation is $y = 0$ mm. The pressure values are expressed in dB relative to 1 Pa and the colorbar goes from 76 to 126 dB relative to 1 Pa. Cumulative growth of the second harmonic component inside the sphere and scattering phenomena can be observed.

5.3 Conclusions

In this Chapter, a method which makes use of a Steepest Descent scheme to model nonlinear wave fields propagation through inhomogeneous biomedical media has been presented. Inhomogeneities in the coefficient of nonlinearity, attenuation and speed of sound have been considered in this Chapter.

First, the convergence of the method has been investigated. Numerical results show convergence towards the solution of the full nonlinear problem. Furthermore, it has been shown how the contrast and the applied scheme determine the convergence rate. Moreover, application of the Steepest Descent solution method results in a method which allows to model stronger contrast than the Neumann and Bi-CGSTAB solution methods presented in Chapter 3 and 4 respectively.

Second, numerical results demonstrate the capability of the method to model nonlinear pressure wave fields propagating through media presenting spatially varying coefficient of nonlinearity, frequency dependent attenuation and speed of sound. In silico experiments show the capability of the method to deal with scattering.

In conclusion, Steepest Descent represents a suitable scheme that allows to deal with a broader variety of contrasts than Neumann and Bi-CGSTAB. Nevertheless, when compared to Neumann, it comes with the cost of an increased complexity and computational load, i.e. more vectors need to be computed and stored and four spatio-temporal convolutions are required per iteration. When

compared to Bi-CGSTAB it comes with the cost of an increased computational load and decreased convergence rate.

Application of the method developed

The INCS method has been applied to test the feasibility of a new ultrasound beamforming technique, i.e. parallel transmit beamforming using Orthogonal Frequency Division Multiplexing (OFDM) applied to harmonic imaging. In this Chapter, the theory of the technique proposed, its advantages as well as its drawbacks and restrictions are addressed. Next, numerical results are presented and compared with standard parallel beamforming. Measurements have also been performed. The obtained results confirm the applicability of the technique proposed for a transducer with a realistic bandwidth.

6.1 Parallel transmit beamforming using OFDM for harmonic imaging

6.1.1 Introduction

Real-time 3D ultrasound images are nowadays used in diagnostic medical applications. To achieve the desirable frame rate, a high volumetric data acquisition rate is necessary. This is limited by the number of lines necessary to generate an image of sufficient resolution, and by the speed of sound, as it determines the time of flight for the pulse-echo signals. To overcome this limitation, parallel processing approaches [60, 61, 62, 63, 64, 65, 66] have been developed. One of the most well known is the Explososcan [67, 68, 69]. With this method, a wide

beam in transmission is used to insonify a large volume, and multiple lines are simultaneously acquired by means of narrower receiver beams. This method is referred to as standard parallel beam forming. In principle, this technique is also applicable to harmonic imaging, e.g. second harmonic imaging [12, 13, 14, 15]. However, the demand for high-amplitude pressure wave fields necessary to generate the harmonic components clashes with the idea of using a wide-angled beam in transmission, as this results in a large spatial decay of the acoustic pressure. To enhance the amplitude of the harmonics it is preferable to do the reverse; transmit several narrow parallel beams and use a wide-angled beam for reception.

In this Chapter it is investigated whether this concept can be utilized for second harmonic imaging [70]. To generate parallel beams that are distinguishable in transmission, orthogonal frequency division multiplexing (OFDM) [71, 72] is utilized. With this technique, multiple channels are generated by allocating to each channel a different portion of the available bandwidth. These orthogonal bandwidths are utilized to transmit pulses which are modulated at different center frequencies. In this manner, the capability to generate simultaneously multiple distinguishable channels, is obtained. Each channel can be independently utilized to generate a beam, that can be steered over a desired angle by application of appropriate time delays between elements. In Section 6.2 the theory is discussed. Numerical and experimental results are contained in Section 6.3, in which standard parallel beamforming is compared with the method proposed in this Chapter. All transmit, receive and combined transmit-receive beam profiles have been simulated up to the second harmonic component using the Iterative Nonlinear Contrast Source (INCS) method [2, 32, 54, 73, 74, 33]. Moreover, measurements in water are used to confirm the feasibility of the technique proposed. Conclusions are drawn in Section 6.4.

6.2 Theory

In this Section the theory of the technique proposed, its drawbacks and restrictions are discussed. The symbols F0 and 2H are used to describe fundamental and second harmonic components respectively and the symbol f is used to describe a specific frequency.

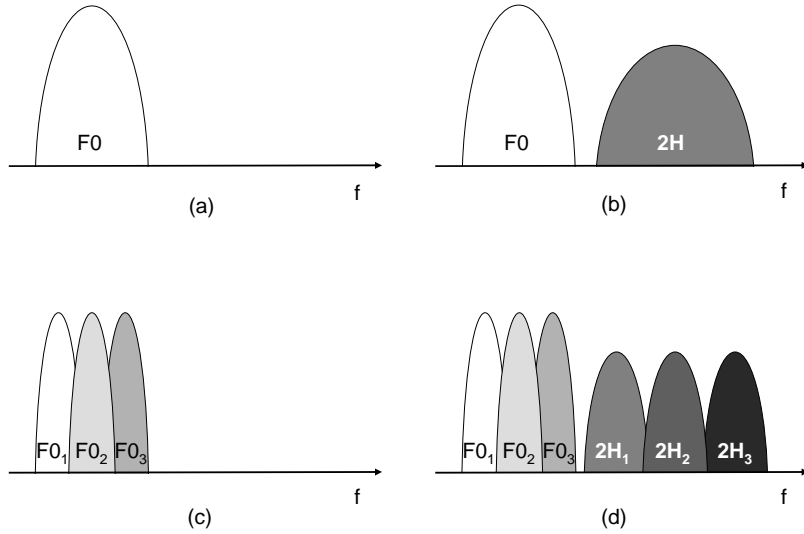


Figure 6.1: Illustration of the basic principles behind parallel transmit beamforming using OFDM: (a) transmitted and (b) received frequency spectra for the standard second harmonic imaging modality, and (c) transmitted and (d) received frequency spectra for the OFDM technique.

6.2.1 Operating principles

Figure 6.1 explains the principles of the OFDM technique proposed. For second harmonic imaging, a given phased array is excited with a pulse with center frequency f^{F0} , resulting in a pressure wave field propagating in a certain direction.

This results in the generation of a fundamental pressure wave field, which is schematically represented in the frequency domain in Fig. 1(a). As this pulse propagates nonlinearly, a second harmonic component, i.e. $2H$, is formed (see Fig. 1(b)). This component is extracted from the scattered wave field to form an image. The very same phased array may also be simultaneously excited with multiple pulses, each having a different center frequency, e.g. three pulses with center frequencies f_1^{F0} , f_2^{F0} and f_3^{F0} (see Fig. 1(c)), resulting in pressure wave fields propagating in different directions. If the properties of the pulses are cho-

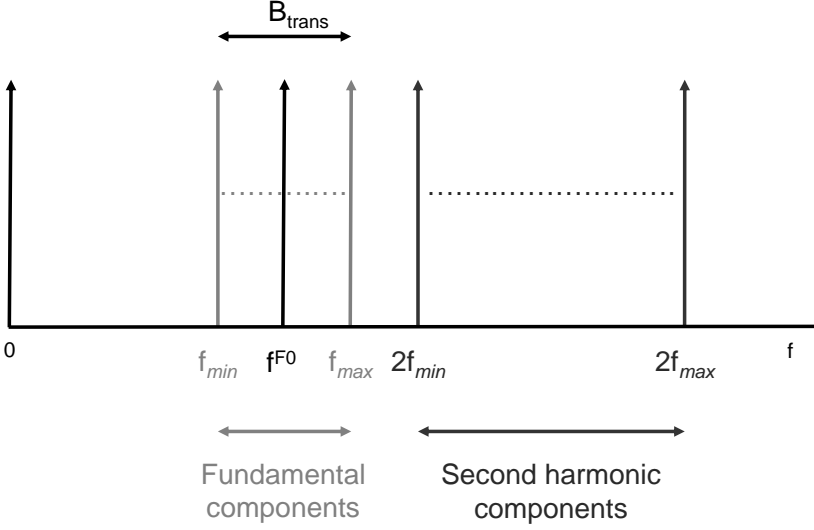


Figure 6.2: Schematic representation of the frequency spectra in case of monochromatic waves.

sen properly, distinguishable second harmonic components are generated during propagation, see Fig. 1(d). The echoes of the second harmonics generated during propagation are recorded in reception and their characteristic frequency content indicates the direction of observation.

6.2.2 Maximum exploitable bandwidth condition

Overlap between the fundamental and the second harmonic components has to be avoided, to guarantee the capability to discriminate between the channels. In case of monochromatic transmission at a frequency f , the rise of the corresponding second harmonic component at a frequency $2f$ is observed (see Fig. 6.2). Therefore, to avoid the overlap, the following restriction applies

$$f_{max} < 2f_{min}, \quad (6.1)$$

with f_{max} and f_{min} being the maximum and minimum frequency respectively utilized in transmission. This condition limits the exploitable bandwidth. Given the bandwidth utilized in transmission $B_{trans} = f_{max} - f_{min}$ and the center frequency $f^{F0} = \frac{1}{2}(f_{max} + f_{min})$, it follows that

$$f_{max} = f^{F0} + \frac{1}{2}B_{trans}, \quad (6.2)$$

$$f_{min} = f^{F0} - \frac{1}{2}B_{trans}, \quad (6.3)$$

and Eq. (6.1) implies the maximum exploitable bandwidth condition

$$B_{trans} < \frac{2}{3}f^{F0}. \quad (6.4)$$

This condition is essential, but not sufficient, to obtain distinguishable channels.

Although monochromatic waves are very useful for an intuitive explanation, they cannot be used for pulse-echo imaging purposes, as they lead to infinitely long time signals. Therefore, the constraint on the exploitable bandwidth has to be formulated for a given pulse shape. Here, Gaussian pulses are analyzed. Under the assumption that the bandwidth of the n th harmonic depends in first approximation on the contribution of the lower harmonics, the following expression holds true for Gaussian modulated pulses

$$B^{[n]} = \sqrt{n}B_{pulse}, \quad (6.5)$$

where $B^{[n]}$ and B_{pulse} represent the bandwidth of the n th harmonic and the fundamental component respectively. In view of this formulation, Eq. (6.1) can be rewritten as follows

$$f_M^{F0} + \frac{1}{2}B_{pulse} < 2f_1^{F0} - \frac{\sqrt{2}}{2}B_{pulse}, \quad (6.6)$$

with f_1^{F0} and f_M^{F0} being respectively the minimum and maximum center frequency utilized in transmission. Given the transmission bandwidth utilized B_{trans} , which in this case is given by

$$B_{trans} = f_M^{F0} - f_1^{F0} + B_{pulse}, \quad (6.7)$$

the maximum exploitable bandwidth condition of Eq. (6.4) becomes

$$B_{trans} < f_1^{F0} + \frac{1 - \sqrt{2}}{2}B_{pulse}. \quad (6.8)$$

This condition guarantees that the fundamental does not mix with the second harmonic components when Gaussian modulated pulses are utilized.

6.2.3 Mixing frequencies

When multiple pulses are transmitted simultaneously, the nonlinear distortion in overlapping areas gives rise to unwanted *mixing frequencies*. These frequencies occur within the frequency band of the second harmonic of different channels, leading to a degradation of the channel discrimination capabilities. A possible strategy to overcome this limitation is to increase the frequency separation between channels. In this way the mixing frequencies occur in frequency bands that can be filtered out in reception, as they do not belong to any of the frequency bands of the second harmonic components of the transmitted signals. However a drawback of this approach is a reduction of the number of available channels, within a given transducer bandwidth. A second strategy to suppress the formation of the unwanted mixing frequencies without reducing the available number of channels, is to notice that these frequencies will not be present in case each pulse is transmitted separately and to decouple the generated beam profiles by introducing a time delay between the pulses. This idea seems to somewhat weaken the parallel character of the described method. However, it should be noted that the applied time delays are much shorter than the typical round-trip travel times.

From now on, straightforward implementation of the OFDM technique will be referred to as approach A, application of OFDM with increased frequency separation between channels will be referred to as approach B and the application of time delays between the pulses will be referred to as approach C. All three approaches are investigated and compared with standard parallel beamforming in the Section 6.3.

6.3 Results

In this Section, the applicability of the OFDM technique described is tested. First, a numerical study is conducted. The aim of this study is to compare the performances of the methods proposed with standard parallel beamforming for the same array configuration. The second harmonic beam profile generated in transmission, the beam profile in reception (obtained as the linear beam profile generated in transmission when the array is excited at the second harmonic frequency) and the combined beam profile (calculated as a product of the transmit and receive beams previously described) are simulated. Scattered waves, due to their relatively low amplitude, are assumed to propagate linearly. Next, experimental results are used to confirm the feasibility of the technique proposed for a

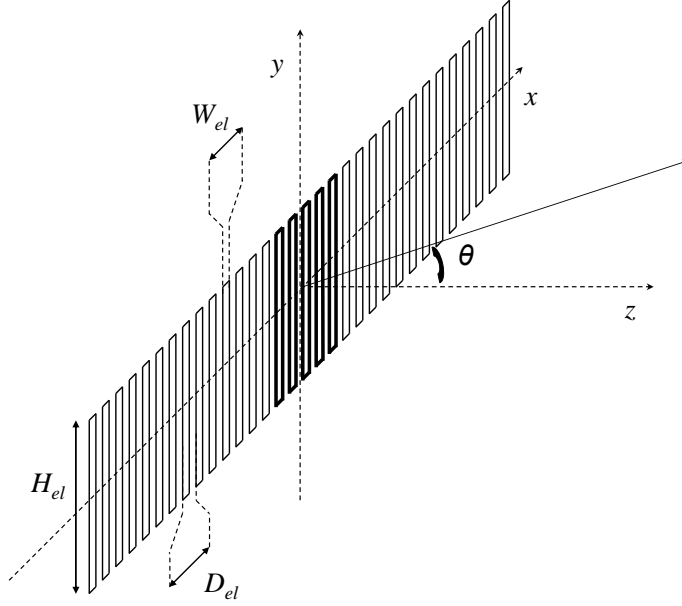


Figure 6.3: The geometry of the linear phased array. The number of elements is $N_{el} = 32$. The dimensions of each element are $W_{el} = 0.27$ mm by $H_{el} = 10$ mm, and the pitch is $D_{el} = 0.31$ mm.

transducer with a realistic bandwidth.

6.3.1 Numerical study

A 32 element linear phased array, submerged in lossy nonlinear blood ($\beta = 4$, $c_0 = 1584$ m/s, $\rho_0 = 1060$ kg/m³, $\alpha = 0.016|f/f_0|^{1.21}$ Np/cm, with $f_0 = 1$ MHz [6]) is used. The origin of the coordinate system is located at the center of the transducer. The steering angle θ is defined in the plane $y = 0$ mm, is measured with respect to the normal of the transducer surface and is positive for positive x . A graphical representation is given in Fig. 6.3. Each element has dimensions $W_{el} = 0.27$ mm by $H_{el} = 10$ mm, and the pitch is $D_{el} = 0.31$ mm. For simplicity, each element is considered to be exploitable both as transmitter and receiver.

First, standard parallel beamforming in reception is considered. The elements

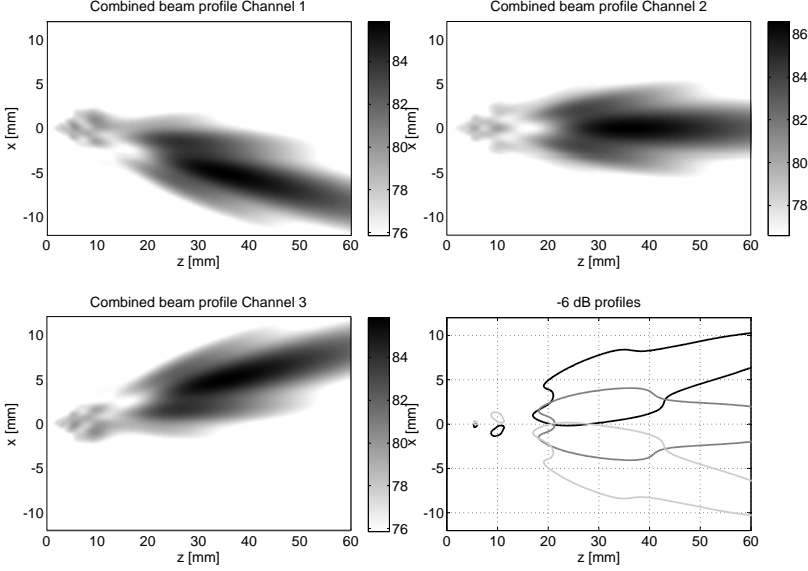


Figure 6.4: Combined transmit-receive beam profiles for three distinct channels, as obtained with standard parallel beamforming. The beams are steered over -8° , 0° and 8° . Values are in dB relative to 1 Pa.

15 to 19, represented in bold in Fig. 6.3, form the transmitter array. These elements are all excited with the same Gaussian modulated pulse, resulting in a source pressure

$$p(t) = P_0 e^{-(2t/t_w)^2} \sin(2\pi f^{F0} t), \quad (6.9)$$

with a fundamental frequency $f^{F0} = 1$ MHz, a time width $t_w = 4.5/f^{F0}$ and a peak pressure $P_0 = 1.5$ MPa. In reception the entire array is used for the beamforming of the second harmonic component. Next, the same array is used to evaluate the performances of OFDM and in particular of approaches A, B and C. In transmission all 32 elements are excited. Three channels are formed by three distinct signals with fundamental frequencies equal to $f_1^{F0} = 0.8$ MHz, $f_2^{F0} = 1$ MHz and $f_3^{F0} = 1.2$ MHz. With OFDM, each signal is amplitude modulated by a Gaussian pulse with a width $t_w = 8/f^{F0}$ and a peak pressure $P_0 = 1.5$ MPa. In reception the elements 15 to 19 are used to measure the distinct second harmonic components (with assumed center frequencies $f_1^{2H} = 1.6$ MHz, $f_2^{2H} = 2$ MHz and $f_3^{2H} = 2.4$ MHz). For approach B, only two channels are used, i.e. channel 1

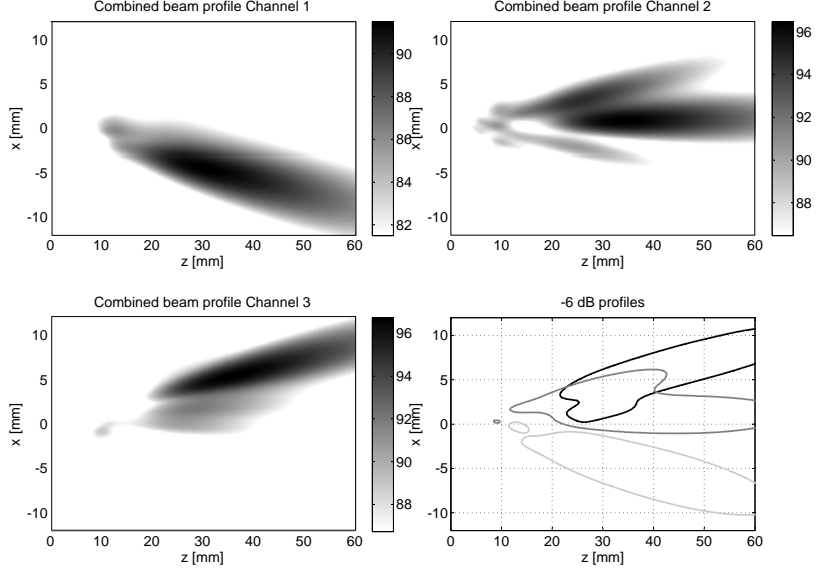


Figure 6.5: Combined transmit-receive beam profiles for three simultaneous channels, as obtained with OFDM approach A. The beams are steered over -8° , 0° and 8° . Values are in dB relative to 1 Pa.

($f_1^{F0} = 0.8$ MHz) and channel 3 ($f_3^{F0} = 1.2$ MHz).

Beam profiles

Results for three distinct channels, respectively steered over -8° (channel 1), 0° (channel 2) and 8° (channel 3), are shown in Fig. 6.4 for standard parallel beamforming, and in Fig. 6.5 for OFDM approach A, when three pulses are simultaneously excited. As visible from Fig. 6.5, an average gain in amplitude in the order of 9 dB is obtained for the main beam when the technique proposed is applied. However, the channel discrimination capabilities of the technique proposed seem to be poor, leading to the presence of spatial overlap between beam profiles, which for channels 2 and 3 is even stronger than for standard parallel beamforming. The cause of this spatial overlap is the presence of the unwanted mixing frequencies. Results for OFDM approach B for two distinct channels, respectively steered over -8° and 8° , are shown in Fig. 6.6. In this case a smoother beam profile and suppression of spatial overlap is observed.

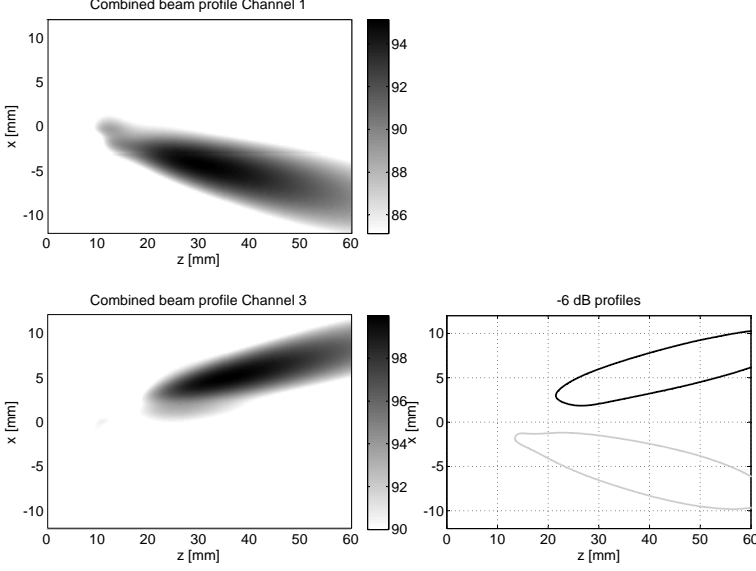


Figure 6.6: Combined transmit-receive beam profiles for two distinct channels, as obtained with OFDM approach B. The beams are steered over -8° and 8° . Values are in dB relative to 1 Pa.

Results for OFDM approach C are shown in Fig. 6.7. Time delays equal to 0, $15/f^{F0}$ and $30/f^{F0}$ are introduced for channel 1, 2 and 3 respectively. As visible, application of time delays leads to a strong reduction of spatial overlap between the beam profiles, while maintaining the capability of transmitting three distinct channels. Both approaches B and C show side-lobes suppression and an average gain in amplitude of 12 dB when compared to standard parallel beamforming in reception.

Signal analysis

Figures 6.8 and 6.9 show the time signals and frequency spectra of the pressure wave field generated at the transducer surface, in the point $(x, y, z) = (0 \text{ mm}, 0 \text{ mm}, 0 \text{ mm})$. From top to bottom, results are shown for standard parallel beamforming (PBF), OFDM parallel transmit beamforming (PTBF) with three simultaneous pulses (approach A), with two simultaneous pulses (approach B), and with three pulses having additional time delays (approach C). As expected,

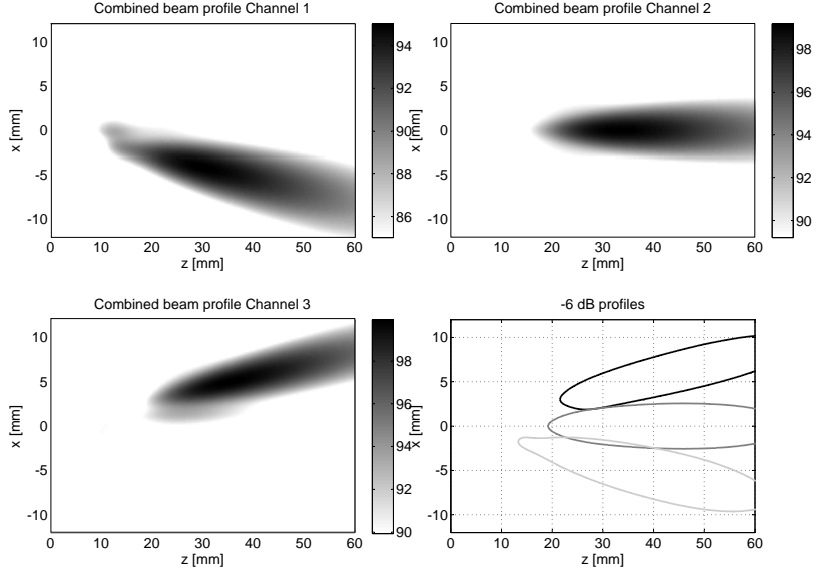


Figure 6.7: Combined transmit-receive beam profiles for three distinct channels when time delays between channels are applied, as obtained with OFDM approach C. The beams are steered over -8° , 0° and 8° . Values are in dB relative to 1 Pa.

the duration of the pulse used for standard parallel beamforming is shorter than for OFDM. With OFDM, distinguishably narrower fundamental components, centered at $f_1^{F0} = 0.8$ MHz, $f_2^{F0} = 1$ MHz and $f_3^{F0} = 1.2$ MHz, are obtained.

Figures 6.10 and 6.11 show the time signals and the frequency spectra of the pressure wave field generated at $z = 40$ mm. From top to bottom, results are shown for standard parallel beamforming (PBF), OFDM parallel transmit beamforming (PTBF) with three simultaneous pulses (approach A), with two simultaneous pulses (approach B), and with three pulses and additional time delays (approach C). In case multiple pulses are simultaneously transmitted, the time axis of the OFDM signals are modified such that up to three signals can be displayed in one plot. Vertical lines have also been added to mark the beginning of the time axis relative to each pulse. From the frequency spectra, two aspects can be observed. First, when OFDM techniques are employed, the second har-

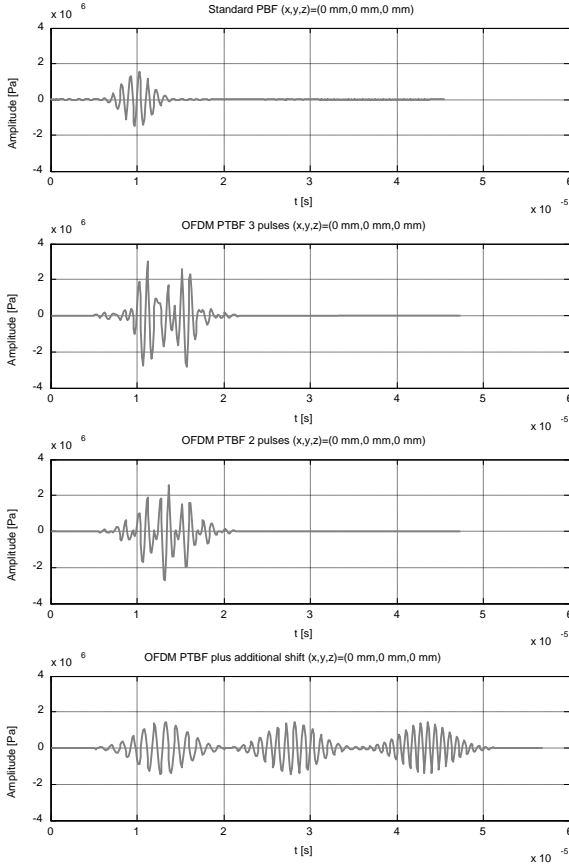


Figure 6.8: Signal analysis at the transducer surface. Time signals are compared for the four approaches described, i.e. from top to bottom, results are shown for standard parallel beamforming (PBF), OFDM parallel transmit beamforming (PTBF) with three simultaneous pulses (approach A), with two simultaneous pulses (approach B), and with three pulses and additional time delays (approach C).

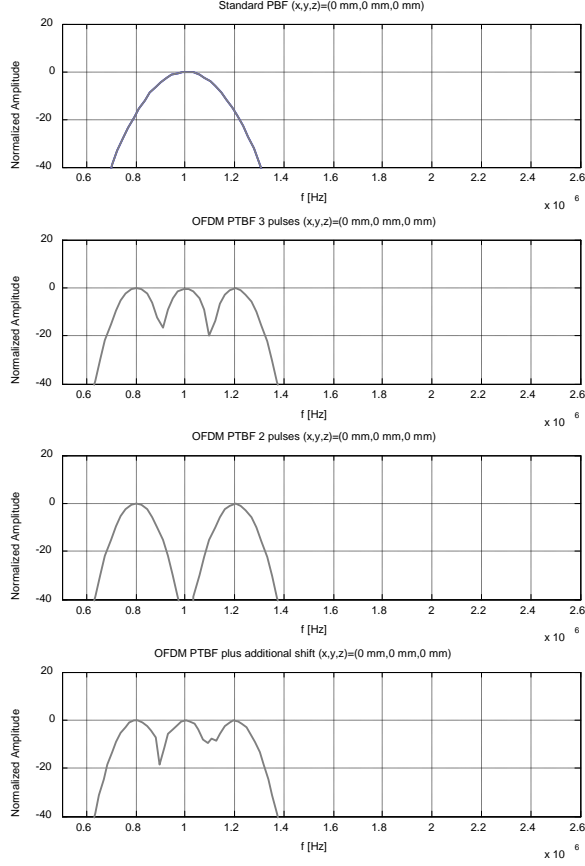


Figure 6.9: Signal analysis at the transducer surface. Normalized frequency spectra are compared for the four approaches described, i.e. from top to bottom, results are shown for standard parallel beamforming (PBF), OFDM parallel transmit beamforming (PTBF) with three simultaneous pulses (approach A), with two simultaneous pulses (approach B), and with three pulses and additional time delays (approach C).

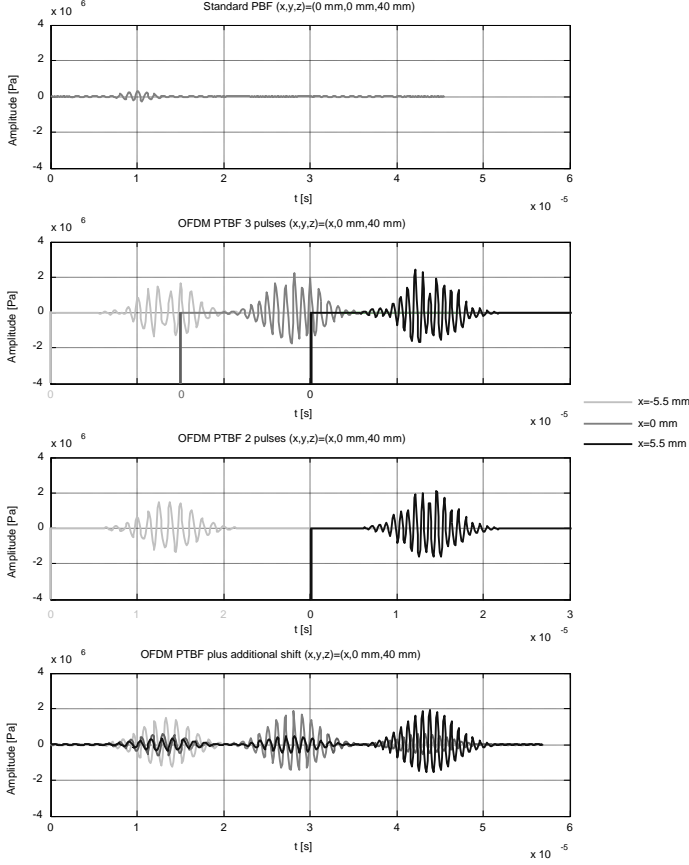


Figure 6.10: Signal analysis at $z = 40$ mm. Time signals are compared for the four approaches described, i.e. from top to bottom, results are shown for standard parallel beamforming (PBF), OFDM parallel transmit beamforming (PTBF) with three simultaneous pulses (approach A), with two simultaneous pulses (approach B), and with three pulses and additional time delays (approach C). In case OFDM is applied, different points in space are used to analyze the signals, i.e. $(x, y, z) = (0$ mm, -5.5 mm, 40 mm) for channel 1, $(x, y, z) = (0$ mm, 0 mm, 40 mm) for channel 2 and $(x, y, z) = (0$ mm, 5.5 mm, 40 mm) for channel 3 (See legend).

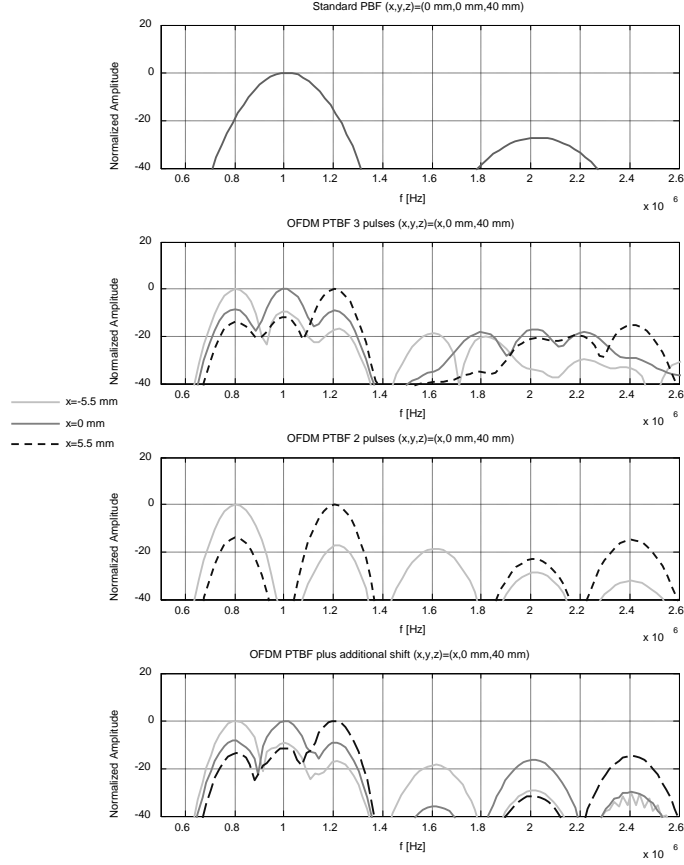


Figure 6.11: Signal analysis at $z = 40$ mm. Normalized frequency spectra are compared for the four approaches described, i.e. from top to bottom, results are shown for standard parallel beamforming (PBF), OFDM parallel transmit beamforming (PTBF) with three simultaneous pulses (approach A), with two simultaneous pulses (approach B), and with three pulses and additional time delays (approach C). In case OFDM is applied, different points in space are used to analyze the signals, i.e. $(x, y, z) = (0\text{ mm}, -5.5\text{ mm}, 40\text{ mm})$ for channel 1, $(x, y, z) = (0\text{ mm}, 0\text{ mm}, 40\text{ mm})$ for channel 2 and $(x, y, z) = (0\text{ mm}, 5.5\text{ mm}, 40\text{ mm})$ for channel 3 (See legend).

monic components generated have higher amplitude than for standard parallel beamforming. Second, the phenomenon of the mixing frequencies is clearly visible. When three pulses are simultaneously transmitted (approach A), significant second harmonic mixing content centered at 1.8 and 2.2 MHz is visible. These frequencies will cause difficulties in channel discrimination and make it necessary to apply narrow-bandwidth filters to select the appropriate frequencies. Here, we applied rectangular filters with a 0.2 MHz bandwidth centered around the center frequency (f_1^{2H} , f_2^{2H} , f_3^{2H}) of the second harmonic related to each channel. On the other hand, when two pulses are utilized (approach B), mixing frequencies are formed, but do not interfere with the second harmonic content related to the transmitted pulses ($2H_1$, $2H_3$). Therefore, channel discrimination capabilities are improved and broader filters can be applied. Here we applied rectangular filters with a 0.4 MHz bandwidth centered around the center frequency of the corresponding second harmonic component. When additional delays are implemented, no relevant mixing frequencies are present and hence the same broader filters may be applied. Note that the application of filters with a narrower bandwidth affects the duration of the filtered second harmonic pulse (see Fig. 6.12). Here, filtered second harmonic pulses as obtained at $z = 40$ mm, are compared for the four approaches described. As may be observed, when approach A is considered, longer second harmonic time pulses are obtained compared to approaches B and C, leading to further degradation of the axial resolution. Second harmonic pulses as obtained with two simultaneously transmitted pulses and with the application of additional delays show basically the same features, among which a shorter duration when compared to approach A.

In view of the number of channels, the duration of the filtered pulses, the avoidance of the mixing frequencies and the reduction of side-lobes, approach C seems to be preferable over the others.

6.3.2 Measurements

An experiment has been conducted to test the applicability of the OFDM technique proposed, in case approach C is considered. An in house built cylindrical transducer, with center frequency $f^{F0} = 1$ MHz and radius $r = 11$ mm, was immersed in water and excited with a driving signal identical to the one used for the numerical study of approach C (see top image in Fig. 6.13). The driving signal was generated using an arbitrary waveform generator (Agilent Technologies, 33250A) followed by an amplifier (ENI, 2100L RF power amplifier). As receiver, a calibrated needle hydrophone with a 0.2 mm diameter probe with associated

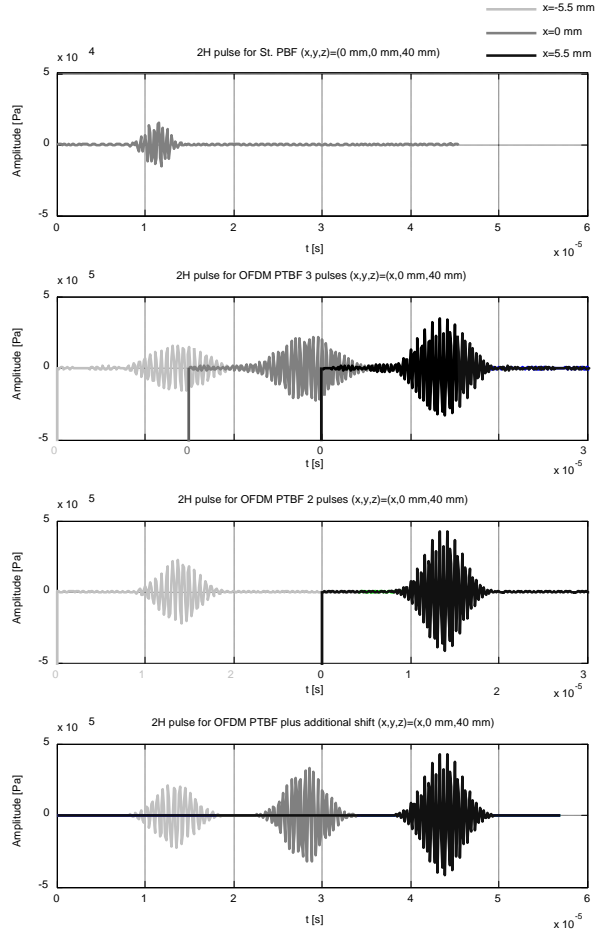


Figure 6.12: Signal analysis at $z = 40$ mm. Second harmonic pulses are compared for the four approaches described, i.e. from top to bottom, results are shown for standard parallel beamforming (PBF), OFDM parallel transmit beamforming (PTBF) with three simultaneous pulses (approach A), with two simultaneous pulses (approach B), and with three pulses and additional time delays (approach C). In case OFDM is applied, different points in space are used to analyze the signals, i.e. $(x, y, z) = (0 \text{ mm}, -5.5 \text{ mm}, 40 \text{ mm})$ for channel 1, $(x, y, z) = (0 \text{ mm}, 0 \text{ mm}, 40 \text{ mm})$ for channel 2 and $(x, y, z) = (0 \text{ mm}, 5.5 \text{ mm}, 40 \text{ mm})$ for channel 3 (See legend).

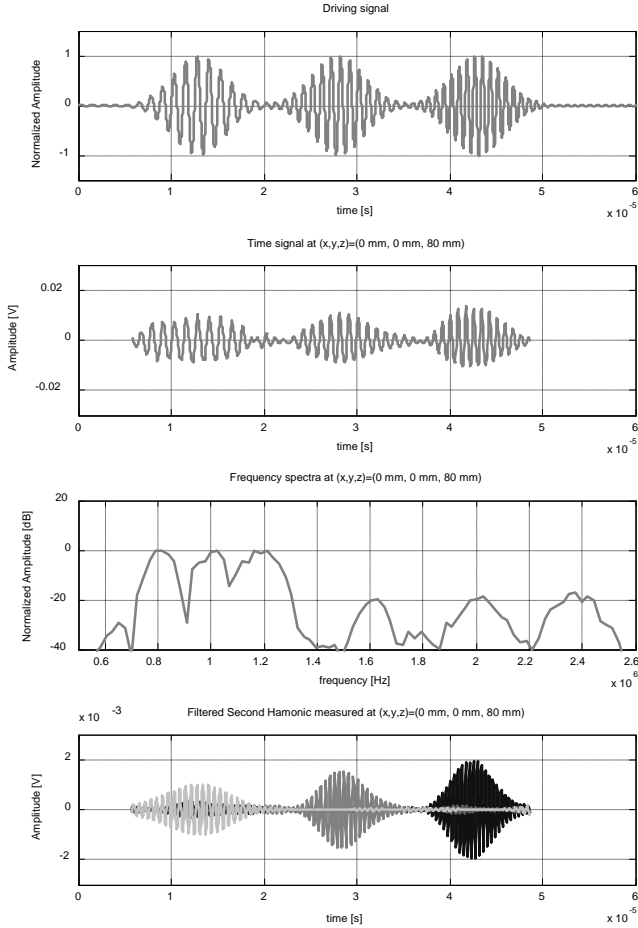


Figure 6.13: Measurements, as obtained for OFDM parallel transmit beamforming with additional time delays (approach C). From top to bottom, the graphs relative to the driving signal, the time signal measured and corresponding normalized frequency spectrum, and the three filtered second harmonic pulses, are respectively shown.

submersible pre-amplifier and DC coupler (Precision Acoustics) was positioned at 80 mm distance from the transmitter. Measurements were collected using an oscilloscope (Agilent Technologies, DSO7054A). The time signal measured and corresponding normalized frequency spectrum, obtained at the natural focus $(x, y, z) = (0 \text{ mm}, 0 \text{ mm}, 80 \text{ mm})$, are plotted in the second and third image from the top in Fig. 6.13. The three filtered second harmonic pulses are plotted at the bottom in Fig. 6.13.

6.4 Conclusions

Application of parallel transmit beamforming for harmonic imaging using orthogonal frequency division multiplexing (OFDM) has been investigated and compared with standard parallel beamforming. For standard parallel beamforming, a wide beam in transmission is generated using a five element linear array and multiple lines are simultaneously acquired in reception by means of narrower beams generated by a 32 elements linear array. For the OFDM technique proposed in this Chapter, the same array is used, but the transmitter and receiver have been interchanged. Hence, multiple narrow beams are generated in transmission using a 32 elements linear array and a wide beam, generated using a five elements linear array, is used for reception. With the method proposed, multiple distinguishable narrow beams with different center frequencies are transmitted in parallel while a wide angle beam is used for reception. Using different frequencies to generate multiple beams in transmission results in direction-dependent attenuation. However, the frequencies utilized will in general not differ largely from each other, such that they can be transmitted within the transducer bandwidth. Nevertheless, compensation for this effect might be necessary for imaging. Numerical studies, which include frequency dependent attenuation, show the ability of this method to reduce the presence of unwanted side-lobes and meanwhile increase the amplitude of the main beam by 12 dB as compared to standard parallel beamforming. These improvements are expected to influence positively the signal to noise ratio and the achievable penetration depth of a given imaging system. A drawback of the method proposed is a reduction of the axial resolution due to utilization of pulses with a narrower bandwidth.

Measurements have been performed to assess the feasibility of the method proposed for a practical transducer. The possibility to excite an ultrasound transducer with multiple Gaussian modulated pulses, each having a different center

frequency, and the capability to discriminate between the second harmonic components of each channel, are confirmed.

In this study, the advantages of using OFDM for parallel transmit beam forming are shown by simply interchanging the transmitter with the receiver. Nevertheless, these advantages might be further improved by employing the entire linear array in reception.

Finally, the presented feasibility study has been conducted on a linear array, hence for a 2D imaging system. Nevertheless, there do not appear to be any limitations for a further extension of the method presented to 3D imaging.

Conclusions and Discussion

7.1 Conclusions

From the research presented in this thesis, the following conclusions can be drawn:

- The numerical method described in this thesis is an extension of the already existing Iterative Nonlinear Contrast Source (INCS) method. The INCS method was originally developed for modeling pressure wave field propagation through homogeneous nonlinear media with frequency dependent power law attenuation. Here, the method has been extended to deal with spatially varying attenuation, coefficient of nonlinearity and speed of sound. The extensions presented in this thesis employ the full-wave character of the INCS method, which allows to model scattering. The resulting method maintains the characteristics of the INCS method. Hence, it only requires two points per smallest wavelength or period and does not favor a particular direction of propagation, which makes it suitable to model steered pressure wave fields generated from medical phased array transducers.
- The nonlinear propagation through inhomogeneous media may be described using an integral equation formulation. Originally, the INCS method provided a solution of the integral equation via application of a Neumann scheme. This intuitive and easily implementable iterative scheme allows to deal with moderate losses and nonlinearity. However, for stronger contrast, the convergence of the Neumann scheme is no more ensured. Therefore, to extend the method to deal with strong losses and/or realistic inhomo-

geneities in the speed of sound, alternative iterative schemes are necessary. The ideal iterative scheme should provide a faster convergence, be capable to cope with stronger contrast and have a reduced complexity and computational cost per iteration as compared to Neumann. In this thesis two alternatives to Neumann have been investigated, i.e. Bi-CGSTAB and Steepest Descent.

Bi-CGSTAB is capable to cope with stronger contrast than Neumann, has a faster convergence but an increased complexity and computational load per iteration. The main computational cost is in fact represented by the convolution operation, which for Neumann is occurring once per iteration, while for Bi-CGSTAB two convolution operations are necessary per iteration. In addition, it requires a linearization of the integral equation. This approximation introduces a significant error which is relevant for the harmonics of the fourth order or higher.

Steepest Descent is capable to cope with stronger contrasts than Neumann and Bi-CGSTAB and no approximation of the integral equation is necessary. When compared to Bi-CGSTAB, it results in a slower convergence and in an increased computational load, i.e. four convolution operations are necessary per iteration.

To conclude, Steepest Descent is, among the schemes investigated, the scheme that allows to deal with the broadest variety of contrasts, e.g. strong losses and realistic inhomogeneities in the speed of sound. Neumann represents the optimal scheme when simpler configurations have to be modeled, e.g. pressure wave fields through homogeneous nonlinear media, as it is the least demanding scheme from a computational point of view. Bi-CGSTAB represents the optimal scheme when simulations up to the third harmonic have to be computed as it allows to model a significantly broad variety of contrasts with a significantly reduced amount of iterations when compared to Neumann and Steepest Descent. Table 7.1 summarizes the analysis. Here, a plus sign identifies the scheme that performs best with respect to a given aspect.

- The numerical method described in this thesis has been developed to assist in the design and development of novel ultrasound modalities and imag-

Table 7.1: Performances comparison for the three schemes described.

Performances	Neumann	Bi-CGSTAB	Steepest Descent
Computational cost	+	0	–
Convergence rate	0	+	0
Harmonics up to 3H	+	+	+
Harmonics above 3H	+	0	+
Inhomogeneous β	+	+	+
Inhomogeneous attenuation	0	+	+
Inhomogeneous S.O.S.	–	0	+

ing techniques. As an example of its potentials, it has been utilized to test the feasibility of a new ultrasound imaging method, i.e. parallel transmit beamforming using orthogonal frequency division multiplexing applied to harmonic imaging. With this method multiple distinguishable narrow beams with different center frequency are transmitted in parallel and a wide angle beam is used for reception. Numerical studies show the capability of this method to reduce the presence of unwanted side-lobes and meanwhile increase the amplitude of the main beam as compared to standard parallel beamforming. This will improve the signal-to-noise ratio and the penetration depth of a given imaging system. A drawback of the method proposed is a reduction of the axial resolution due to utilization of pulses with a narrower bandwidth. Measurements confirm the feasibility of the method proposed for a practical transducer. It is shown that it is possible to measure distinct second harmonic components belonging to different channels when an ultrasound transducer is excited with multiple gaussian modulated pulses, each having a different center frequency.

7.2 Discussion

The work presented in this thesis can be used as a basis to investigate the following extensions and applications of the numerical method described:

- In Chapter 2 we derived the integral equation which represents the theoretical fundament of our method. Spatial inhomogeneities in the small signal sound velocity have been modeled via inhomogeneities in the static

compressibility, considering the static volume density of mass to be homogeneous. Inhomogeneities in the static volume density of mass may be included in the model via an additional contrast term. This additional term is obtained by introducing a spatially varying volume density of mass in the equation of motion [31].

- As shown in Chapter 4, the linearization of the integral equation introduces a systematic error which appears to be relevant for the harmonics of the fourth order or higher. A possible solution to overcome this limitation is to generalize the assumption behind the linearization. The total acoustic wave field p may in fact be considered as a combination of a primary field p^{start} and a perturbation \tilde{p} . In Chapter 4, the linear incident field $p^{(0)}$ is taken as primary field p^{start} . However, the primary field p^{start} can be chosen arbitrary. The more the primary field p^{start} is similar to the actual field p , the less is the influence of the perturbation \tilde{p} , and the smaller is the error introduced by the linearization. For example, the primary field p^{start} can be set equal to the output of the linearized method at a given iteration [56, 57].
- In this thesis we only investigated the performances of three numerical schemes, i.e. Neumann, Bi-CGSTAB and Steepest Descent. Other schemes, or combinations of the one already investigated, may result in better performances, e.g. with respect to convergence rate.
- In Chapter 6 we showed a possible application of the method developed. At that stage the idea was to compare standard parallel beam forming and the proposed OFDM technique when applied to the same array configuration, by only interchanging the transmitter and receiver array. It is important to stress that application of the OFDM technique described does allow for parallel transmission and reception together, i.e. using the entire array for transmission and reception. In this way the benefits shown by the OFDM technique would increase further, at the cost of additional processing to perform parallel beam forming in reception.
- The potentials of the method developed have not been fully investigated in this thesis as the focus of the research presented was more towards the extension of the original INCS method to model nonlinear propagation through inhomogeneous biomedical media. As an example, with the current extensions, it is now possible to test and compare different imaging algorithms.

Appendix A

Appendix: Lossy Green's function combined with contrast source approach

In this thesis, a compliance memory function is used to model attenuation. For homogeneous lossy media, the losses may either be described as a contrast with respect to a lossless background medium resulting in a real valued propagation coefficient, a lossless Green's function and an attenuation contrast source, or as a property of the background medium resulting in a complex valued propagation coefficient and a lossy Green's function. In lossy media with spatially varying attenuation, the same two approaches exist. Either, a lossless background medium is taken and all the spatially varying losses are described via an attenuation contrast source, or an attenuative background medium is taken and only those (spatially varying) losses which deviate from the losses assigned to the background medium yield an attenuation contrast source. As in this thesis the INCS method is used to model nonlinearity via a contrast source, it may sound logical to model all the losses via an attenuative contrast source. In this Appendix, it is investigated which of the two approaches works best for modeling nonlinear propagation in lossy media. Here, only the Neumann iterative solution method presented in Chapter 2 is used to solve the corresponding integral equation, and only spatially varying attenuation and coefficient of nonlinearity are considered.

A.1 Results

In this Section, two scenarios are used to demonstrate the numerical performance of the method presented. First, results as obtained for a one-dimensional plane wave propagating up to 100 mm through a linear lossy medium with inhomogeneities in the attenuation are presented and discussed. Lossy linear muscle is considered as background medium and a lossy linear blood slap is positioned from 20 mm to 40 mm depth. See Table A.1 for acoustical medium parameters. This is referred to as scenario A. Next, results as obtained for the same scenario, including nonlinear propagation, are presented and discussed. This is referred to as scenario B. In both scenarios the pressure wave field is generated by a Gaussian modulated pulse, resulting in a pressure field which, in the point $x=0$ mm, equals

$$P(t) = P_0 e^{-(2t/t_w)^2} \sin(2\pi f_0 t), \quad (\text{A.1})$$

with center frequency $f_0 = 1$ MHz, window width $t_w = 3/f_0$ and peak pressure $P_0 = 1$ MPa.

A.1.1 Convergence

To investigate the convergence of both approaches, the same normalized error utilized in Chapter 2, which equals

$$\text{Err}_1^{(n)} = \frac{\|\mathbf{p}^{(n)} - \mathbf{p}^{(n-1)}\|}{\|\mathbf{p}^{(0)}\|}, \quad (\text{A.2})$$

is used. The vector $\mathbf{p}^{(n)}$ is the obtained pressure field after n iterations, and $\mathbf{p}^{(n)} = 0$ for $n < 0$. The normalized error $\text{Err}_1^{(n)}$ is shown in Fig. A.1 in case a lossless Green's function (black) or a lossy Green's function (gray) is respectively used, both for scenario A (solid) and B (dashed). As visible, the normalized error functional decreases faster in case a lossy Green's function is used, especially when nonlinear propagation is taken into account. For the scenarios analyzed, application of a lossy Green's function results in a reduction of the number of iterations required equal to 10 for scenario A and 111 for scenario B. This is due to the fact that modeling inhomogeneous attenuation solely via a contrast source strongly affects the convergence, especially when nonlinear propagation is considered, as the higher harmonics generated by the cumulative nonlinear distortion experience a higher attenuation; resulting in an increasingly stronger contrast.

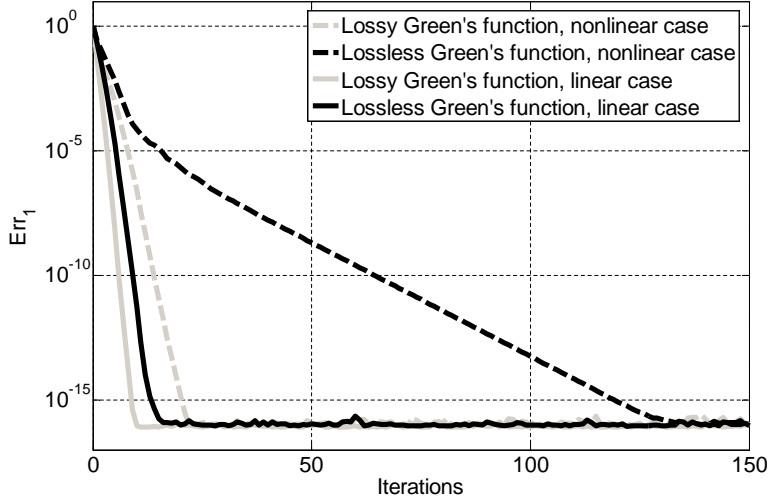


Figure A.1: Normalized error functional $\text{Err}_1^{(n)}$ for scenario A (solid) and B (dashed) obtained using a lossless (black) or a lossy (gray) Green's function.

A.1.2 In silico experiments

Fig. A.2 shows normalized frequency spectra for scenario A, at 100 mm depth, obtained using a lossy (solid line) and lossless (dashed line) Greens's function. Normalization is performed with respect to the lossless case. Results show excellent agreement between the two methods.

Fig. A.3 shows space-time domain results for scenario A obtained with both methods. As visible, when the lossless Green's function is used, an additional reflection is shown at 100 mm depth. This additional reflection is caused by the presence of an additional interface at the edge of the simulated domain.

Fig. A.4 shows normalized frequency spectra, up to the 5th harmonic component, for scenario B as obtained using a lossy (solid line) and lossless (dashed line) Greens's function. Results show excellent agreement between the two methods,

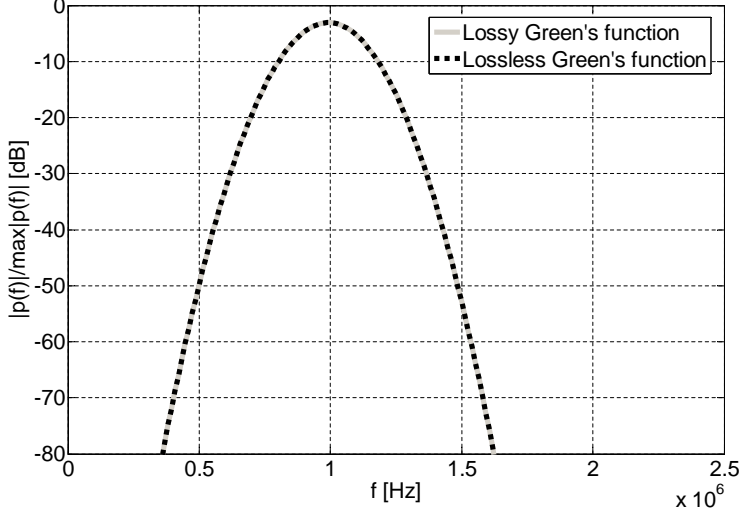


Figure A.2: Normalized frequency spectra of the propagating pulse, obtained at $x = 100$ mm. Normalization is performed with respect to the lossless case.

also in case nonlinear propagation is taken into account.

A.2 Conclusions

The results obtained using either a lossless or lossy Green's function are in excellent agreement with each other; whether nonlinear propagation is or is not taken into account. However, when a lossy Green's function is used, significantly less iterations are required to solve the integral equation, especially when nonlinear propagation is taken into account. This is caused by the fact that the losses related to the background medium are included directly in the Green's function. Hence, the iterative process has to correct only for a relatively small effect when compared to the application of an attenuation contrast source only. Further, utilization of a lossy Green's function automatically prevents for scattering artifacts caused by truncation of the numerical domain.

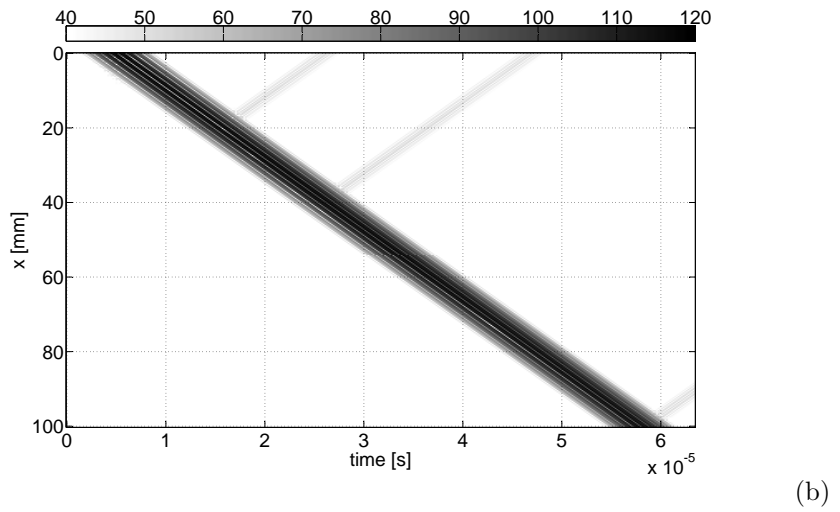
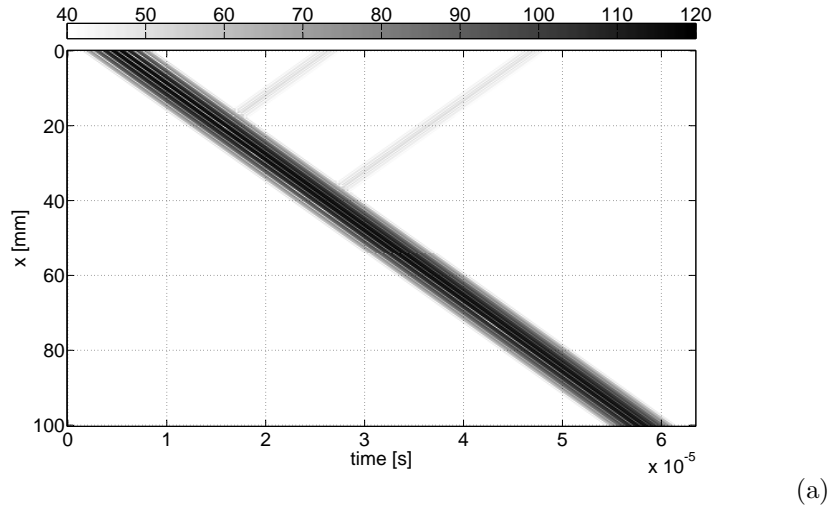


Figure A.3: Space-time domain results obtained with the (a) lossy and (b) lossless Green's function. Amplitude values are in dB relative to 1 Pa.

Table A.1: Acoustic medium parameters. The relation between a and α_1 is $\alpha_1 = a(2\pi)^{-b}$.

Medium	a	b	c_{bg}	β
	$[\text{Np cm}^{-1} \text{ MHz}^{-b}]$	$[-]$	$[\text{m s}^{-1}]$	$[-]$
blood	$1.6 \cdot 10^{-2}$	1.21	1584	4.00
muscle	$4.03 \cdot 10^{-2}$	1.0	1580	4.72

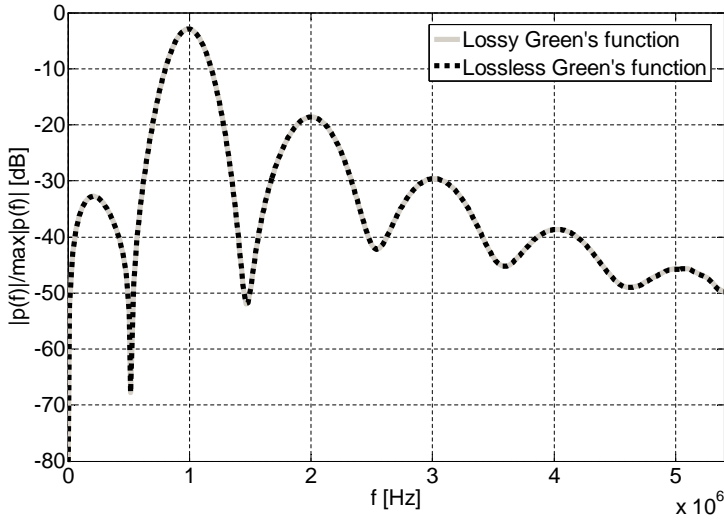


Figure A.4: Normalized frequency spectra of the nonlinear propagating pulse, obtained at $x = 100$ mm. Normalization is performed with respect to the lossless case.

Appendix **B**

Appendix: List of configurations

Figure B.1 shows a diagram which provides an overview of all the configurations utilized. For each configuration, a schematic drawing, the utilized source and contrast types, and the applied solution method, are given.



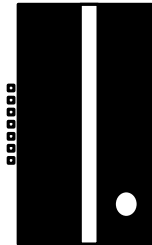
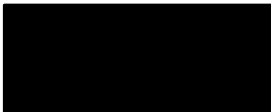

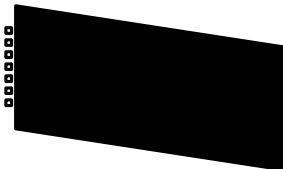
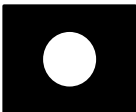
Config.	Drawing	Source and contrast	Solution method
1		<ul style="list-style-type: none">- Plane wave- Inhomogeneous β	<ul style="list-style-type: none">- Neumann
2a		<ul style="list-style-type: none">- Linear array- Homogeneous	<ul style="list-style-type: none">- Neumann
2b		<ul style="list-style-type: none">- Linear array- Inhomogeneous attenuation	<ul style="list-style-type: none">- Neumann
3		<ul style="list-style-type: none">- Plane wave- Homogeneous	<ul style="list-style-type: none">- Neumann- BiCGSTAB- Steepest Descent
4a		<ul style="list-style-type: none">- Linear array- Homogeneous plus inhomogeneous attenuation	<ul style="list-style-type: none">- Neumann- BiCGSTAB
4b		<ul style="list-style-type: none">- Linear array [skew domain]- Homogeneous	<ul style="list-style-type: none">- Neumann
5a 5b		<ul style="list-style-type: none">- Plane wave- Inhomogeneous s.o.s. plus inhomogeneous β, attenuation and s.o.s.	<ul style="list-style-type: none">- Neumann- BiCGSTAB- Steepest Descent

Figure B.1: Overview of the configurations utilized.

Bibliography

- [1] J. Huijssen, “Modeling of nonlinear medical diagnostic ultrasound”, PhD Thesis, Delft University of Technology, 35–120 and 171–186 (2008), available from <http://repository.tudelft.nl> (date last viewed 06/24/2010).
- [2] J. Huijssen and M.D. Verweij, “An iterative method for the computation of nonlinear, wide-angle, pulsed acoustic fields of medical diagnostic transducers”, *J. Acoust. Soc. Am.* **127**, 33–44 (2010).
- [3] P.L.M.J. van Neer, M.G. Danilouchkine, M.D. Verweij, L. Demi, M.M. Voormolen, A.F.W. van der Steen, and N. de Jong, “Comparison of fundamental, second harmonic, and superharmonic imaging: A simulation study”, *J. Acoust. Soc. Am.* **130**, 3148–3157 (2011).
- [4] L. Demi, M.D. Verweij and K.W.A. van Dongen, “Parallel Transmit Beamforming using Orthogonal Frequency Division Multiplexing for Harmonic Imaging”, *Proc. IEEE Int. Ultrason. Symp.*, 148–151 (2011).
- [5] W.D. O’Brien Jr., “Assessing the Risk for Modern Diagnostic Ultrasound Imaging”, *Japanese J. App. Phy.* **37**, 2781–2788 (1998).
- [6] T.L. Szabo, *Diagnostic ultrasound imaging* Elsevier, Amsterdam, 535 (2004).
- [7] J.C. Somer, “Electronic sector scanning for ultrasonic diagnosis”, *Ultrasonics* **6**, 153–159 (1968).

- [8] N. Bom, C.T. Lande, J. Honkoop and P.G. Hugenholtz “Ultrasonic viewer for cross-sectional analyses of moving cardiac structures”, *Biom. Eng.* **6**, 500–503 (1971).
- [9] J.N. Hilberath, MD, D.A. Oakes, MD, S.K. Shernan, MD, B.E. Bulwer, MD, M.N. Dambra, MD, and H.K. Eltzschig, MD, PhD, “Safety of Trans-esophageal Echocardiography”, *J. Am. Soc. Echocard.* **23**, 1115–1127 (2010).
- [10] M.A. Averkiou, D.N. Roundhill, and J.E. Powers, “A new imaging technique based on the nonlinear properties of tissues”, *Proc. IEEE Int. Ultrason. Symp.* , 1561–1566 (1997).
- [11] K. Hynynen, “Demonstration of enhanced temperature elevation due to nonlinear propagation of focussed ultrasound in dog’s thigh in vivo”, *Ultras. Med. Biol.* , **13**, 85–91 (1987).
- [12] T. Christopher, “Finite amplitude distortion-based inhomogeneous pulse echo ultrasonic imaging”, *IEEE Trans. Ultrason. Ferr. Freq. Control*, **44**, 125–130 (1997).
- [13] M.A. Averkiou, D.N. Roundhill, and J.E. Powers, “A new imaging technique based on the nonlinear properties of tissues”, in *Proc. IEEE Int. Ultrason. Symp.*, 1561–1566 (1997).
- [14] B. Ward, A.C. Baker, and V.F. Humphrey, “Nonlinear propagation applied to the improvement of resolution in diagnostic medical ultrasound equipment”, *J. Acoust. Soc. Am.* **101**, 143–154 (1999).
- [15] F. Tranquart, N. Grenier, V. Eder, and L. Pourcelot, “Clinical use of ultrasound tissue harmonic imaging”, *Ultras. Med. Biol.* **25**, 889–894 (1999).
- [16] A. Bouakaz and N. de Jong, “Native tissue imaging at superharmonic frequencies”, *IEEE Trans. Ultrason. Ferroelect. Freq. Contr.* **50**, 496–506 (2003).
- [17] A. Bouakaz, S. Frigstad, F. Ten Cate, and N. de Jong, “Super harmonic imaging: A new technique for improved contrast detection”, *Ultras. Med. Biol.* **28**, 59–68 (2002).
- [18] J.H. Ginsberg and M.F. Hamilton, “Computational methods”, in *Nonlinear acoustics*, edited by M. Hamilton and D. Blackstock, 309–341 (1998).

- [19] M.D. Verweij and J. Huijssen, “Computational methods for nonlinear acoustic wavefields in homogeneous media”, in *Computational methods in nonlinear acoustics: Current trends*, edited by C. Vanhille and C. Campos-Pozuelo, 1–19 (Research Signpost, Kerala, India) (2011).
- [20] S. Aanonsen, J. Barkve, J. Naze Tjøtta and S. Tjøtta, “Distortion and harmonic generation in the nearfield of a finite amplitude sound beam” *J. Acoust. Soc. Am.* **74**, 749–768 (1984).
- [21] Y.S. Lee and M.F. Hamilton, “Time-domain modeling of pulsed finite-amplitude sound beams” *J. Acoust. Soc. Am.* **97**, 906–917 (1995).
- [22] P.T. Christopher and K.J. Parker, “New approaches to nonlinear diffractive field propagation” *J. Acoust. Soc. Am.* **90**, 488–499 (1991).
- [23] R. Zemp, J. Tavakkoli and R. Cobbold, “Modeling of nonlinear ultrasound propagation in tissue from array transducers” *J. Acoust. Soc. Am.* **113**, 139–152 (2003).
- [24] J. Tavakkoli, D. Cathignol, R. Souchon and O.A. Sapozhnikov, “Modeling of pulsed finite amplitude focused sound beams in time domain” *J. Acoust. Soc. Am.* **104**, 2061–2072 (1998).
- [25] T. Varslot and G. Taraldsen, “Computer simulation of forward wave propagation in tissue” *IEEE Trans. Ultrason. Ferroelectr. Freq. Contr.* **52**, 1473–1482 (2005).
- [26] V.A. Khokhlova, A.E. Pomomarev, M.A. Averkiou and L.A. Crum, “Non-linear pulsed ultrasound beams radiated by rectangular focused diagnostic transducers” *Acoust. Phys.* **52**, 481–489 (2006).
- [27] V.W. Sparrow and R. Raspet, “A numerical method for general finite amplitude wave propagation in two dimensions and its application to spark pulses” *J. Acoust. Soc. Am.* **90**, 2683–2691 (1991).
- [28] S. Ginter, M. Liebler, E. Steiger, T. Dreyer and R.E. Riedlinger, “Full-wave modeling of therapeutic ultrasound: Nonlinear ultrasound propagation in ideal fluids” *J. Acoust. Soc. Am.* **111**, 2049–2059 (2002).
- [29] I.M. Hallaj and R.O. Cleveland, “FDTD simulation of finite-amplitude pressure and temperature fields for biomedical ultrasound” *J. Acoust. Soc. Am.* **105**, L7–L12 (1999).

- [30] J. Hoffelner, H. Landes, M. Kaltenbacher and R. Lerch, “Finite element simulation of nonlinear wave propagation in thermoviscous fluids including dissipation” *IEEE Trans. Ultrason. Ferroelect. Freq. Contr.* **48**, 779–786 (2001).
- [31] M.D. Verweij and J. Huijssen, “A filtered convolution method for the computation of acoustic wave fields in very large spatiotemporal domains”, *J. Acoust. Soc. Am.* **125**, 1868–1878 (2009).
- [32] J. Huijssen, M.D. Verweij, and N. de Jong, “Green’s function method for modeling nonlinear three-dimensional pulsed acoustic fields in diagnostic ultrasound including tissue-like attenuation”, *Proc. IEEE Int. Ultrason. Symp.*, 375–378, (2008).
- [33] L. Demi, M.D. Verweij and K.W.A. van Dongen, “A contrast source method for nonlinear acoustic wave fields in media with spatially inhomogeneous attenuation”, *J. Acoust. Soc. Am.* **129**, 1221–1230 (2011).
- [34] J.T. Fokkema and P.M. van den Berg, *Seismic applications of acoustic reciprocity* Elsevier, Amsterdam, 54–55 (1993).
- [35] M.D. Verweij and J. Huijssen, “Nonlinear and dissipative constitutive equations for coupled first-order acoustic field equations that are consistent with the generalized Westervelt equation”, *Proc. 17th ISNA*, 241–244 (2006).
- [36] J. Huijssen and M.D. Verweij, “Nonlinear constitutive equations derived for fluids obeying an ideal gas, a Tai-Kirkwood or a B/A type equation of state”, *Proc. 17th ISNA*, 552–555 (2006).
- [37] M.F. Hamilton and D.T. Blackstock, “On the coefficient of nonlinearity β in nonlinear acoustics”, *J. Acoust. Soc. Am.* **83**, 74–77 (1988).
- [38] S.I. Aanonsen, T. Barkve, J. Naze Tjøtta and S. Tjøtta, “Distortion and harmonic generation in the nearfield of a finite amplitude sound beam”, *J. Acoust. Soc. Am.* **75**, 749–768, (1984).
- [39] M.F. Hamilton and C.L. Morfey, “Model equations”, in *Nonlinear Acoustics*, edited by M.F. Hamilton and D.T. Blackstock, Academic Press, San Diego, 54–56 (1998).
- [40] J. Naze Tjøtta and S. Tjøtta, “Interactions of sound waves. part I: Basic equations and plane waves”, *J. Acoust. Soc. Am.* **82**, 1425–1428, (1987).

- [41] M.D. Verweij, “Modeling space-time domain acoustic wave fields in media with attenuation: The symbolic manipulation approach”, *J. Acoust. Soc. Am.* **97**, 831–43 (1995).
- [42] M.D. Verweij, “Transient acoustic wave fields in continuously layered media with depth-dependent attenuation: An analysis based on higher-order asymptotics”, *J. Acoust. Soc. Am.* **101**, 1808–1820 (1997).
- [43] D.V. Widder, *The Laplace transform* Princeton University Press, New York, 61–63 (1946).
- [44] G. Doetsch, *Handbuch der Laplace Transformation, Vol. 1 (Handbook of the Laplace Transformation)* Birkhäuser, Basel, 73 (1950).
- [45] J.P. Schouten, *Operatorenrechnung mit Anwendungen auf Technische Probleme Operational calculus with applications to technical problems* (Springer-Verlag, Berlin, 101–103 (1961).
- [46] R.E.A.C. Paley and N. Wiener, “Fourier transforms in the complex domain”, *Am. Math. Soc. Colloq. Pub.* **19**, 116–117 (1934).
- [47] A.T. de Hoop, *Handbook of radiation and scattering of waves* Academic Press, London, 71–75 and 1065–1070 (1995), available from <http://www.atdehoop.com> (date last viewed 06/24/2010).
- [48] P.N.T. Wells, “Absorption and dispersion of ultrasound in biological tissue”, *Ultras. Med. Biol.* **1**, 369–376 (1985).
- [49] F.A. Duck, *Physical properties of tissue* (Academic Press, London, 1990), 99–123.
- [50] J.C. Bamber, “Ultrasonic properties of tissues” *Ultrasound in medicine*, edited by F.A. Duck, A.C. Baker, and H.C. Starritt Institute of Physics, Bristol, 73–76 (1998).
- [51] R.S.C. Cobbold, *Foundations of biomedical ultrasound* Oxford University Press, Oxford, 72–81 (2007).
- [52] T.L. Szabo, “Causal theories and data for acoustic attenuation obeying a frequency power law”, *J. Acoust. Soc. Am.* **97**, 14–24 (1995).
- [53] A.T. de Hoop, “Convergence criterion for the time-domain iterative Born approximation to scattering by an inhomogeneous, dispersive object”, *J. Opt. Soc. Am. A* **8**, 1256–1260 (1991).

- [54] L. Demi, M.D. Verweij, J. Huijssen, N. de Jong, and K.W.A. van Dongen, "Attenuation of ultrasound pressure fields described via a contrast source formulation", Proc. IEEE Int. Ultrason. Symp., 1590–1593 (2009).
- [55] H.A. van der Vorst, "Bi-CGSTAB: a Fast and Smoothly Converging Variant of Bi-CG for the Solution of Nonsymmetric Linear Systems", J. Sci. Stat. Comput. **13**, 631–644 (1992).
- [56] M.D. Verweij, L. Demi and K.W.A. van Dongen, "Linearization strategies for the iterative nonlinear contrast source method for full-wave simulation of nonlinear ultrasound fields", Proc. 19th ISNA, 243–246 (2012).
- [57] M.D. Verweij, L. Demi and K.W.A. van Dongen "Computation of nonlinear ultrasound fields using a linearized contrast source method", J. Acoust. Soc. Am., to appear in the upcoming Special Issue on Therapeutic Applications of Ultrasound (2013).
- [58] P. M. van den Berg and A. Abubakar, "Contrast source inversion method: state of art", Progress In Electromagnetics Research, **34**, 189–218 (2001).
- [59] W. Thompson Jr., *Radiation from a spherical acoustic source near a scattering plane*, J. Acoust. Soc. Am. **60**, 781–787 (1976).
- [60] B. Delannoy, R. Torguet, C. Bruneel and E. Bridoux, "Ultrafast electronical image reconstruction device", Echocardiography, edited by C.T. Lancee (Nijhoff, The Hague), **1**, Chap. 3, 447–450 (1979).
- [61] B. Delannoy, R. Torguet, C. Bruneel, E. Bridoux, J.M. Rouvaen and H. LaSota "Acoustical image reconstruction in parallel-processing analog electronic systems", J. Appl. Phys., **50**, 3153–3159 (1979).
- [62] A. Koyano, Y. Yoshikawa, T. Konishi, Y. Kobayashi, Y. Kimita, T. Hidai, N. Osaka, C. Hayashi and K. Fujie "A high quality ultrasound imaging system using linear array transducer", Ultras. Med. Biol. , **1**, 100 (1982).
- [63] S. Hirahuka and T. Nagasaki, Japanese patent SHO-53-126135, applied 16 Oct. (1979).
- [64] S. Hirahuka and T. Nagasaki, Japanese patent SHO-55-56746, granted 17 Apr. (1980).
- [65] H. Miwa, H. Hayashi, T. Shimura, and K. Murakami, "Simultaneous multi-frequency ultrasonography - The principle and technology", Proc. IEEE Int. Ultrason. Symp., 655–659 (1981).

- [66] G. Montaldo, M. Tanter, J. Bercoff, N. Benech, and M. Fink, “Coherent Plane-Wave Compounding for Very High Frame Rate Ultrasonography and Transient Elastography”, *IEEE Trans. Ultrason. Ferroelect. Freq. Contr.* **56**, 489–506 (2009).
- [67] D.P. Shattuck, M.D. Weinschenker, S.W. Smith, O.T. von Ramm “Explososcan: A parallel processing technique for high speed ultrasound imaging with linear phased array”, *J. Acoust. Soc. Am.* **75**, 1273–1282 (1984).
- [68] S.W. Smith, H.G. Pavy and O.T. von Ramm “High-speed ultrasound volumetric imaging system. I. Transducer design and beam steering”, *IEEE Trans. Ultrason. Ferroelect. Freq. Contr.* **38**, 100–108 (1991).
- [69] O.T. von Ramm, S.W. Smith and H.G. Pavy “High-speed ultrasound volumetric imaging system. II. Parallel processing and image display”, *IEEE Trans. Ultrason. Ferroelect. Freq. Contr.* **38**, 109–115 (1991).
- [70] L. Demi, M.D. Verweij and K.W.A. van Dongen “Parallel Transmit Beamforming Using Orthogonal Frequency Division Multiplexing Applied to Harmonic Imaging A Feasibility Study”, *IEEE Trans. Ultrason. Ferroelect. Freq. Contr.* **59**, 2439–2447 (2012).
- [71] M. Alard and R. Lassalle, “Principles of modulation and channel coding for digital broadcasting for mobile receivers”, *EBU Review*, 47–69, August (1987).
- [72] M. Russel and G. Stüber, “Terrestrial digital video broadcasting for mobile reception using OFDM”, *Wireless Personal Comms, Special Issue Multi-Carrier Comms*, vol. 2, no. 1–2, 45–66 (1995).
- [73] J. Huijssen, M.D. Verweij and N. de Jong, “3D Time-Domain Modeling of Nonlinear Medical Ultrasound with an Iterative Green’s Function Method”, *Proc. IEEE Int. Ultrason. Symp.*, 2124–2127 (2006).
- [74] L. Demi, M.D. Verweij, N. de Jong, and K.W.A. van Dongen, “Modeling Nonlinear Acoustic Wave fields in Media with Inhomogeneity in the Attenuation and in the Nonlinearity”, *Proc. IEEE Int. Ultrason. Symp.*, 2056–2059 (2010).

Summary

The design and optimization of medical ultrasound modalities require a method for modeling the propagation of pressure wave fields through biomedical tissue. This method needs to be capable of modeling various phenomena in order to provide a good approximation of the pressure wave fields simulated. Among these phenomena are nonlinear propagation, attenuation, and scattering caused by arbitrary inhomogeneities in the acoustic properties of the medium. Existing methods for the numerical simulation of nonlinear acoustic wave field may be grouped into two major categories; forward wave methods and full wave methods. Forward wave methods start with the pressure distribution at the transducer plane, and propagate the field forward in a preferred direction which usually corresponds to the propagation of the main part of the field. Furthermore, many methods that belong to this category, such as the KZK method, make use of a parabolic approximation. Due to these facts, forward wave methods are inaccurate for fields that (partly) propagate in directions that largely deviate from the preferred direction of propagation, and in particular cannot deal with backscattered wave fields. On the other hand, full wave methods do not involve a preferred direction of propagation. Finite Difference and Finite Element methods are examples of full wave methods. However, as a drawback, these methods need to sample at considerably more than 2 points per smallest wavelength and per shortest period. As a consequence, the number of grid points needed to handle a realistic computational domain soon becomes too large. The Iterative Nonlinear Contrast Source (INCS) method is a full wave method which avoids this problem. Taking advantage of the filtered convolution method, it only requires

two points per wavelength or period. Originally, the method was used to model nonlinear propagation in homogeneous nonlinear media with frequency power law attenuation. In this thesis the basic steps of INCS are conserved and the method has been extended to deal with spatially varying attenuation, coefficient of nonlinearity and speed of sound. The method developed uses a generalized form of the Westervelt equation which includes a spatially dependent coefficient of nonlinearity, speed of sound and relaxation function.

The generalized Westervelt equation may be recast into an integral equation and solved using different iterative schemes. In this thesis three possible iterative schemes have been investigated: Neumann, Bi-CGSTAB and Steepest Descent. Neumann represents an intuitive and easily implementable iterative scheme that allows with the treatment of moderate losses and nonlinearity. However, for stronger contrasts, convergence is no longer ensured. Therefore, to extend the method to deal with strong losses and/or realistic inhomogeneities in the speed of sound, alternative iterative schemes are necessary. The first iterative scheme tested is Bi-CGSTAB. This scheme is capable of coping with stronger contrast than Neumann and has a faster convergence, but an increased complexity and computational load per iteration. Furthermore, it comes with the cost of an approximation that influences the results obtained. In fact, the scheme requires a linearization of the integral equation. This approximation introduces a systematic error that is relevant for the harmonics of the fourth order or higher. In addition, for very strong contrasts, the scheme may diverge. To overcome these limitations, Steepest Descent is tested as a second alternative to Neumann. This scheme is capable of coping with stronger contrasts than Neumann and Bi-CGSTAB and no linearization of the integral equation is necessary, but, when compared to Bi-CGSTAB, it results in a slower convergence and in an increased computational load. Despite its drawbacks, Steepest Descent represents, between the schemes investigated, the scheme that allows the treatment of the broadest variety of contrasts, e.g. strong losses and realistic inhomogeneities in the speed of sound.

As an example of a possible application of the method developed, a feasibility study of a new beam forming technique, i.e. parallel transmit beam forming using orthogonal frequency division multiplexing applied to harmonic imaging, has been performed. With this technique, multiple distinguishable narrow beams with different center frequencies are transmitted in parallel and a wide angle

beam is used for reception. Numerical studies show the capability of this technique to reduce the presence of unwanted side-lobes and meanwhile increase the amplitude of the main beam as compared to standard parallel beam forming. These improvements are expected to positively influence the signal to noise ratio and the achievable penetration depth of a given imaging system. A drawback of the technique proposed is a reduction of the axial resolution due to utilization of pulses with a narrower bandwidth. Measurements in water have been performed and confirmed the feasibility of the technique proposed for a practical transducer. The possibility to excite an ultrasound transducer with multiple Gaussian modulated pulses, each having a different center frequency, and the capability to discriminate between the second harmonic components of each channel, are confirmed.

Samenvatting

Om transducenten voor medisch ultrageluid te ontwerpen en te optimaliseren, is een methode nodig waarmee de voortplanting van drukgolven door biomedisch weefsel gesimuleerd kan worden. Deze methode dient verscheidene verschijnselen te kunnen simuleren om een goede benadering van de gemodelleerde drukgolven te verkrijgen. Voorbeelden van deze verschijnselen zijn onder andere niet-lineaire propagatie, demping, en verstrooiing veroorzaakt door arbitraire inhomogeniteiten in de akoestische eigenschappen van het medium. Bestaande methoden voor de numerieke simulatie van niet-lineaire acoustische golfvelden kunnen in twee groepen worden opgesplitst: voorwaartse golf methoden en integraal veld methoden. Voorwaartse golf methoden beginnen met de drukverdeling op het transducentoppervlak, en propageren het veld voorwaarts in een gewenste richting welke typisch overeen komt met de voortplantingsrichting van de sterkste component van het veld. Bovendien gebruiken veel van deze methoden, zoals bijvoorbeeld de KZK methode, een parabolische benadering. Als gevolg van deze eigenschappen zijn voorwaartse golf methoden niet nauwkeurig voor velden welke (deels) propageren in een richting die sterk afwijkt van de gesimuleerde propagatierichting, en bovendien niet in staat om terugwaartse verstrooiing te simuleren. Daarentegen hebben integraal veld methoden geen voorkeursrichting. De Finite Difference en Finite Element methoden zijn voorbeelden van dergelijke integraal veld methoden. Echter, deze methoden hebben als nadeel dat meer dan twee punten per kleinste golflengte en kortste periode nodig zijn. Hierdoor wordt het aantal rasterpunten dat benodigd is om een realistisch rekenkundig domein te simuleren snel te groot om te behappen. De Iteratieve Niet-lineaire

Contrast Bron (Iterative Nonlinear Contrast Source, INCS) methode is een integraal veld methode welke specifiek ontworpen is om deze beperking weg te nemen. Door gebruik te maken van gefilterde convolutie, zijn slechts twee punten per golflengte nodig. Oorspronkelijk werd deze methode gebruikt om niet-lineaire propagatie in homogene niet-lineaire media te simuleren, inclusief een machtswet-model voor de frequentieafhankelijke damping. In dit proefschrift blijft de gedachtengang van de originele INCS methode behouden en is de methode uitgebreid om spatiële variatie in zowel damping als niet-lineariteitscoëfficiënt en geluidssnelheid te kunnen behandelen. De ontwikkelde methode maakt gebruik van een gegeneraliseerde vorm van de Westervelt vergelijking welke een spatiaal variërende niet-lineariteitscoëfficiënt, geluidssnelheid en relaxatiefunctie bevat.

De gegeneraliseerde Westervelt vergelijking kan herschreven worden tot een integraalvergelijking, en opgelost worden met behulp van verscheidene iteratieve methoden. In dit proefschrift zijn drie mogelijke iteratieve schemas onderzocht: Neumann, Bi-CGSTAB en Steepest Descent. Neumann is een intuïtief en eenvoudig te implementeren schema waarmee gematigde damping en niet-lineariteit behandeld kunnen worden. Echter, de convergentie is voor sterke contrasten niet langer gegarandeerd. Derhalve zijn, om sterkere contrasten en/of realistische inhomogeniteiten in de geluidssnelheid te kunnen simuleren, alternatieve methoden noodzakelijk. Het eerste alternatieve schema is Bi-CGSTAB. Dit schema kan sterkere contrasten aan dan Neumann en convergeert sneller, maar heeft een grotere complexiteit en vereist meer rekentijd per iteratie. Bovendien is een benadering noodzakelijk welke het eindantwoord beïnvloedt. Het schema vereist namelijk een linearisatie van de integraalvergelijking. Deze benadering introduceert een systematische fout welke significant wordt voor harmonischen van vierde orde of hoger. Verder kan het schema voor zeer sterke contrasten divergeren. Om deze beperkingen te verhelpen, is Steepest Descent als tweede alternatief voor Neumann getest. Dit schema kan sterkere contrasten aan dan zowel Neumann als Bi-CGSTAB en de integraalvergelijking hoeft niet gelineariseerd te worden, maar in vergelijking met Bi-CGSTAB heeft het een langzamere convergentie en een hogere complexiteit en rekentijd. Ondanks deze nadelen is Steepest Descent het schema dat de grootste diversiteit aan contrasten, bijvoorbeeld sterke damping en realistische inhomogeniteiten in geluidssnelheid, aan kan.

Om een mogelijke toepassing van de ontwikkelde methode te demonstreren, is een haalbaarheidsstudie uitgevoerd naar een nieuwe beam forming techniek toegepast op niet-lineaire propagatie. De techniek maakt gebruik van meerdere orthogonale frequenties, waardoor meerdere smalle bundels in parallel uitgezon-

den worden welke met een brede bundel gelijktijdig worden ontvangen. Numerieke simulaties tonen aan dat deze techniek in staat is om ongewenste zijlobben te onderdrukken, terwijl de amplitude van de hoofdlobben in vergelijking met standaard parallel beam forming toeneemt. Deze voordelen zullen de signaal-ruis verhouding en penetratiediepte van een gegeven afbeeldingssysteem waarschijnlijk in positieve zin beïnvloeden. Een nadeel van deze techniek is een verminderde axiale resolutie aangezien pulsen met een beperktere bandbreedte gebruikt worden. Metingen in water bevestigen de haalbaarheid van de techniek voor een realistische transducent. Zowel de mogelijkheid om een ultrageluidtransducent gelijktijdig aan te sturen met meerdere Gaussische pulsen van verschillende frequenties, als de mogelijkheid om de gegenereerde tweede harmonische componenten van elk signaal te kunnen onderscheiden, zijn aangetoond.

About the author

Libertario Demi was born in Cecina (Italy) on November 19th 1983. In 2002 he started his studies in telecommunication engineering at Pisa University (Italy). From April to September 2006 he planned and established a satellite connection in Burkina Faso, (Africa) in the city of Boulsa as volunteer for Engineers Without Borders Pisa (Ingegneria Senza Frontiere Pisa). From February to March 2007 he supervised a project with the aim to install a satellite connection in Burkina Faso, (Africa) in the city of Touguri as volunteer for Engineers Without Borders Pisa (Ingegneria Senza Frontiere Pisa). From September 23rd to December 21st 2007 he carried out research activities at the University of Adelaide (South Australia), School of Electrical and Electronic Engineering, as part of his master thesis project. Supervisor: Prof. Bevan D. Bates EEE Dept. Univer-



Photo by *Chiara Nicolosi*
www.chiaranicolosi.com

sity of Adelaide. On February 18th 2008 he received, with the grade of 110/110 *cum laude*, his master degree in telecommunication engineering, specialization (laurea specialistica) in remote sensing and signal processing from Pisa University. Title of the thesis: *Automatic target recognition based on ISAR images with applications to real data acquired in an anechoic chamber*. First Supervisor: Marco Martorella, Research/Lecturer Fellow, Department of Information Engineering, University of Pisa. Second Supervisor: Prof. Fabrizio Berizzi, Lecturer, Department of Information Engineering, University of Pisa. From March 1st to June 30th 2008 he carried out research activities at Pisa University, Department of Information Engineering, with a scholarship in ICT from CNIT (Consorzio Nazionale Interuniversitario per le Telecomunicazioni). From July 1st 2008 to June 30th 2012 he carried out research activities on modeling nonlinear medical diagnostic ultrasound as a PhD at Delft University of Technology (the Netherlands). From July 15th 2012 he is carrying out research activities on prostate cancer detection using contrast agents as a PostDoc at Eindhoven University of Technology (the Netherlands).

Publications

Papers in international journals

1. M.D. Verweij, L. Demi and K.W.A. van Dongen, “Computation of nonlinear ultrasound fields using a linearized contrast source method”, J. Acoust. Soc. Am., to appear in the upcoming Special Issue on Therapeutic Applications of Ultrasound (2013).
2. L. Demi, M.D. Verweij and K.W.A. van Dongen, “Parallel Transmit Beam-forming Using Orthogonal Frequency Division Multiplexing Applied to Harmonic Imaging - A Feasibility Study”, IEEE Trans. Ultrason. Ferroelect. Freq. Contr., **59**, 2439-2448 (2012).
3. P.L.M.J. van Neer, M.G. Danilouchkine, M.D. Verweij, L. Demi, M.M. Voormolen, A.F.W. van der Steen, and N. de Jong, “Comparison of fundamental, second harmonic, and superharmonic imaging: A simulation study”, J. Acoust. Soc. Am. **130**, 3148-3157 (2011).
4. L. Demi, K.W.A. van Dongen and M.D. Verweij, “A contrast source method for nonlinear acoustic wave fields in media with spatially inhomogeneous attenuation”, J. Acoust. Soc. Am. **129**, 1221-1230 (2011).
5. M. Martorella, E. Giusti, L. Demi, Z. Zhou, A. Cacciamano, F. Berizzi and B. Bates, “Target Recognition by means of Polarimetric ISAR images”, IEEE Trans. Aerosp. Electr. Syst. **47**, 225-239 (2011).

Papers in conference proceedings

1. L. Demi, M.D. Verweij and K.W.A. van Dongen, "Modeling Three-Dimensional Nonlinear Acoustic Wave Fields in Media with Spatially Varying Coefficient of Nonlinearity, Attenuation and Speed of Sound", to appear in Proc. IEEE Int. Ultrason. Symp., (2012).
2. M.D. Verweij, L. Demi and K.W.A. van Dongen, "A linearized version of the Iterative Nonlinear Contrast Source method for full-wave simulations of nonlinear ultrasounds field", Proc. 19th ISNA AIP, 243-246 (2012).
3. L. Demi, M.D. Verweij and K.W.A. van Dongen, "Parallel Transmit Beam-forming using Orthogonal Frequency Division Multiplexing for Harmonic Imaging", Proc. IEEE Int. Ultrason. Symp., 148-151 (2011).
4. L. Demi, N. Ozmen-Eryilmaz, K.W.A. van Dongen and M.D. Verweij, "Modeling Nonlinear Pressure Fields in Inhomogeneous Media Using a Lossy Green's Function and a Contrast Source", Proc. IEEE Int. Ultrason. Symp., 2154-2157 (2011).
5. N. Ozmen-Eryilmaz, L. Demi, E.J. Alles, K.W.A. van Dongen and M.D. Verweij, "Modeling Acoustic Wave Field Propagation in 3D Breast Models", Proc. IEEE Int. Ultrason. Symp., 1700-1703 (2011).
6. L. Demi, M.D. Verweij and K.W.A. van Dongen, "Modeling nonlinear acoustic waves in media with inhomogeneities in the coefficient of non-linearity", Proc. POMA for 160th Meeting of the Acoustical Society of America **11** (2010).
7. L. Demi, M.D. Verweij, N. de Jong and K.W.A. van Dongen, "Modeling nonlinear acoustic waves in media with inhomogeneities in the attenuation and in the nonlinearity", Proc. IEEE Int. Ultrason. Symp., 2056-2059 (2010).
8. L. Demi, M.D. Verweij, N. de Jong and K.W.A. van Dongen, "Modeling nonlinear medical ultrasound via a linearized contrast source method", Proc. IEEE Int. Ultrason. Symp., 2175-2179 (2010).
9. S.S. Catusian, F. Longobardi, F. Panicucci, R.P. Bartalesi, L. Demi, A.D. Cuomo and S. Orlandi, "BoulSat Project: Low-cost Wireless Metropolitan Network Implementation in Burkina Faso", Proc. AFRICOM, 78-85 (2009).

10. L. Demi, M.D. Verweij, J. Huijssen, N. de Jong and K.W.A. van Dongen, "Attenuation of Ultrasound Pressure Fields Described via Contrast Source Formulation", Proc. IEEE Int. Ultrason. Symp., 1590-1593 (2009).
11. K.W.A. Dongen, E.J. Alles and L. Demi, "Medical acoustical array expertise at Delft University of Technology", Proc. NAG-DAGA, International Conference on Acoustics, 30-33 (2009).
12. M. Martorella, E. Giusti, L. Demi, Z. Zhou, A. Cacciamano, F. Berizzi and B. Bates, "Automatic Target Recognition by means of Polarimetric ISAR images: a Model Matching Based Algorithm", Proc. IEEE Radar, 27-31 (2008).

Abstracts

1. K.W.A. van Dongen, L. Demi and M.D. Verweij, "Numerical schemes for the Iterative Nonlinear Contrast Source method", 164th Meeting of the Acoustical Society of America (2012).
2. M.D. Verweij, L. Demi and K.W.A. van Dongen, "Rationale behind the Iterative Nonlinear Contrast Source method", 164th Meeting of the Acoustical Society of America (2012).
3. L. Demi, M.D. Verweij and K.W.A. van Dongen, "A linearized contrast source method for full-wave modeling of nonlinear acoustic wave fields in media with strong and inhomogeneous attenuation", 162th Meeting of the Acoustical Society of America (2011).
4. K.W.A. van Dongen, L. Demi and M.D. Verweij, "A full wave method for modeling nonlinear acoustic wave fields in media with inhomogeneous wave speed, attenuation, and parameter of nonlinearity", 162th Meeting of the Acoustical Society of America (2011).
5. M.D. Verweij, L. Demi and K.W.A. van Dongen, "A linearized contrast source method for full-wave modeling of nonlinear acoustic wave fields in homogeneous media", 162th Meeting of the Acoustical Society of America (2011).
6. M.D. Verweij, L. Demi, P.L.M.J. van Neer, M.G. Danilouchkine, N. de Jong, and K.W.A. van Dongen, "A dual pulse technique for improving the

- point spread function of superharmonic imaging systems”, 161th Meeting of the Acoustical Society of America (2011).
7. K.W.A. van Dongen, M.G. Danilouchkine, L. Demi, P.L.M.J. van Neer, N. de Jong, and M.D. Verweij, “A frequency compounding technique for improving the point spread function of superharmonic imaging systems”, 161th Meeting of the Acoustical Society of America (2011).
 8. L. Demi, M.D. Verweij and K.W.A. van Dongen, “Modeling nonlinear acoustic wave fields in inhomogeneous biomedical tissue”, 3rd Dutch Biomedical Engineering Conference (2011).
 9. M.D. Verweij, J. Huijssen, L. Demi, and K.W.A. van Dongen, “Generalization of the Iterative Nonlinear Contrast Source Method to realistic nonlinear biomedical tissue”, 160th Meeting of the Acoustical Society of America (2010).